Washington University in St. Louis

Washington University Open Scholarship

Spring 5-15-2020

Ultrasound guided Diffuse Optical Tomography for Breast Cancer Diagnosis: Algorithm Development

K M Shihab Uddin
Washington University in St. Louis

Follow this and additional works at: https://openscholarship.wustl.edu/eng_etds

Part of the Biomedical Engineering and Bioengineering Commons

WASHINGTON UNIVERSITY IN ST. LOUIS

Department of Biomedical Engineering

Dissertation Examination Committee:
Quing Zhu, Chair
Mark Anastasio
Adam Bauer
Abhinav Jha
Ulugbek Kamilov

Ultrasound guided Diffuse Optical Tomography for Breast Cancer Diagnosis: Algorithm
Development
by
K M Shihab Uddin

A dissertation presented to
The Graduate School
of Washington University in
partial fulfillment of the
requirements for the degree
of Doctor of Philosophy

May 2020
St. Louis, Missouri

Table of Contents

List of Figures

v

List of Tables

<u>Acknowledgments</u>

First, I like to thank Dr Quing Zhu, my PhD supervisor, for her guidance and support throughout my entire PhD. While she taught me how to think like a researcher and how to write a scientific article, which I never did prior to my PhD. I think I am lucky to have a professor who is very accessible and approachable, and I could just walk into her office any time with any problem or concern. I also like to thank Dr Mark Anastasio for his collaboration with our group. He helped me a lot with research ideas, problem formulation and manuscript writing. I acknowledge the value of the critical feedback I received from my thesis committee members, Dr Jha, Dr Kamilov and Dr Bauer, which guided my thesis in right direction. I would like to thank all clinicians, doctors and radiologists who helped to get patients and ex vivo tissue samples.

I am grateful to all my lab mates for their help and support. Specially, Atahar, Shuying, Menghao, Eghbal, Xiandong, Yifeng, Shiqi and Guang, with whom I have directly work in different projects and they also helped me in my projects.

I offer special thanks to the Washington University School of Engineering for allowing us to use their dissertation template as a starting point for the development of this document.

K M Shihab Uddin

Washington University in St. Louis

May 2020

x

Dedicated to my family.

ABSTRACT OF THE DISSERTATION

Ultrasound guided Diffuse Optical Tomography for breast cancer diagnosis: Algorithm

Development

by

K M Shihab Uddin

Doctor of Philosophy in Biomedical Engineering

Washington University in St. Louis, 2020

Professor Quing Zhu, Chair

According to National Breast Cancer Society, one in every eight women in United States is diagnosed with breast cancer in her lifetime. American Cancer Society recommends a semi-annual breast-cancer screening for every woman which can be heavily facilitated by the availability of low-cost, non-invasive diagnostic method with good sensitivity and penetration depth. Ultrasound (US) guided Diffuse Optical Tomography (US-guided DOT) has been explored as a breast-cancer diagnostic and screening tool over the past two decades. It has demonstrated a great potential for breast-cancer diagnosis, treatment monitoring and chemotherapy-response prediction. In this imaging method, optical measurements of four different wavelengths are used to reconstruct unknown optical absorption maps which are then used to calculate the hemoglobin concentration of the US-visible lesion. This dissertation focuses on algorithm development for robust data processing, imaging reconstruction and optimal breast cancer diagnostic strategy development in DOT. The inverse problem in DOT is ill-posed, ill-conditioned, and underdetermined. This makes the task of image reconstruction challenging, and thus regularization-based method need to be employed. In this dissertation, a simple two-step reconstruction method that can produce accurate

image estimates in DOT is proposed and investigated. In the first step, a truncated Moore-Penrose Pseudoinverse solution is computed to obtain a preliminary estimate of the image. This estimate can be reliably determined from the measured data; subsequently, this preliminary estimate is incorporated into the design of a penalized least squares estimator that is employed to compute the final image estimate. Using physical phantoms, the proposed method was demonstrated to yield more accurate reconstruction compared to other conventional reconstruction methods. The method was also evaluated with clinical data that included 10 benign and 10 malignant cases. The capability of reconstructing high contrast malignant lesions improved by the use of the proposed method.

Reconstructed absorption maps are prone to image artifacts from outliers in measurement data from tissue heterogeneity, bad coupling between tissue and light guides, and motion by patient or operator. In this dissertation, a new automated iterative perturbation correction algorithm is proposed to reduce image artifacts based on the structural similarity index (SSIM)) of absorption maps of four optical wavelengths. The SSIM was calculated for each wavelength to assess its similarity with other wavelengths. Absorption map was iteratively reconstructed and projected back into measurement space to quantify projection error. Outlier measurements with highest projection errors were iteratively removed until all wavelength images were structurally similar with SSIM values greater than a threshold. Clinical data demonstrated statistically significant improvement in image artifact reduction.

US guidance with DOT helps to reduce false positive rate and hence reduce number of unnecessary biopsies. However, DOT data processing and image reconstruction speed remains slow compared to real-time US. Real-time or near real time diagnosis with DOT is an important step toward the clinical translation of the US-guided DOT. In this dissertation, to address this important need, we

present a two-stage diagnostic strategy that is computationally efficient and accurate. In the first stage, benign lesions are identified in near real-time by use of a random forest classifier acting on the DOT measurements and radiologists' US diagnostic scores. The lesions that cannot be reliably classified by the random forest classifier will be passed on to the image reconstruction stage. Functional information from the reconstructed hemoglobin concentrations is used by a Support Vector Machine (SVM) classifier for diagnosis in the second stage. This two-step classification approach that combines both perturbation data and functional features results in improved classification, as quantified using the receiver operating characteristic (ROC) curve. Using this two-step approach, area under the ROC curve (AUC) is 0.937 ± 0.009 with sensitivity of 91.4% and specificity of 85.7%. While using functional features and US score, AUC is 0.892 ± 0.027 with sensitivity of 90.2% and specificity of 74.5%. The specificity increased by more than 10% due to the implementation of the random forest classifier.

Chapter 1: Introduction

Breast cancer is the second leading cause of cancer death among women in the United States [1]. About 276,480 new invasive breast cancer cases will be diagnosed in 2020, and 41,170 women will die of it [2]. Near infrared (NIR) diffuse optical tomography (DOT) or diffuse optical spectroscopy (DOS), non-invasive imaging and spectroscopic techniques, have demonstrated their clinical potential for probing tumor angiogenesis, which can be quantitatively assessed by total hemoglobin (tHb) concentration. Tumor angiogenesis, i.e., the creation of new blood vessels, is a hallmark of cancer that reflects the aggressive growth of the cancer cells. Thus, functional information provided by DOT can be useful in breast cancer diagnosis.

In DOT, multiple wavelengths are used to reconstruct the optical absorption and scattering of the tissue, and these data are used to measure oxy and deoxy Hb concentrations. But due to intense light scattering, the diffused NIR light yields low resolution and makes tumor location uncertain. On the contrary, ultrasound can detect very small lesions at depths as deeps as a few millimeters, but it cannot be used in diagnosis since it returns overlapping characteristics for benign and malignant tumor. Hence, ultrasound is used for detecting the location of tumors and diffused light is used for separating benign and malignant tumors based on optical properties. But due to the chest wall effect and data saturation, the actual number of measurements is much less than the number of properties to be reconstructed. Moreover, perturbations produced by heterogeneities is much smaller than the background signals. DOT reconstruction is thus sensitive to measurement errors and noise.

Our lab uses US guided DOT by deploying NIR source-detector fibers and ultrasound array on the same probe. This co-registration permits joint evaluation of acoustic and optical properties. With a priori knowledge of a tumor's shape and location, DOT reconstruction can be localized to a specific 3-dimensional location known as a Born Sphere. While US guidance helps to reduce the number of voxels that need to be examined, our reconstruction problem is still ill-posed and under-determined. This dissertation focuses on (1) robust DOT reconstruction for accurate quantification of blood chromophores, i.e., oxy-hemoglobin and deoxy-hemoglobin, (2) reducing imaging artifact by perturbation correction, and (3) developing the optimal diagnostic strategy to provide near real time assessment of benign tumors and reduce unnecessary biopsies. The dissertation is organized as follows.

In chapter one, we review facts about breast cancer, then discuss its causes and conventional treatment methods. We also discuss the principles of DOT and its application in breast cancer diagnosis and chemotherapy treatment monitoring. Finally, the US guided DOT system developed in our lab is introduced, and its data acquisition and system calibration methods are explained.

In chapter two, we introduce a novel two-step imaging reconstruction method for DOT. Both the DOT forward and inverse problems are presented in detail, and optimization strategies to solve the inverse problem are discussed. Both phantom and clinical study results are presented to prove the effectiveness of the proposed method. Optimal regularization parameter selection strategies are discussed as well.

In chapter three, an iterative perturbation correction scheme is proposed and evaluated with clinical data. The structural similarity of multiple wavelength reconstructed images is used as a criterion to find images with artifacts for the evaluation.

In chapter four, we propose an optimal diagnostic strategy for breast cancer, using both ultrasound and optical data. Random forest classifiers are used to filter out most of benign cases in near real time, based on ultrasound BI-RADS scores and DOT perturbation data. Suspicious lesions are then classified using a support vector machine.

In chapter five, we summarize the dissertation and present some future work directions in robust US image processing, DOT reconstruction, and the evaluation of reconstructed images.

1.1   Breast Cancer

The human breast is mostly made of fat cells known as adipose tissue [1]. Lobules in the breast are the basic structural units of the mammary gland that produces milk [3]. A side view and a top view of the breast are shown in figure 1.1, which is adopted from ref [4]. The breast size increases in the second half of the menstrual cycle, following ovulation [5]. During this natural cyclic growth of the breast, angiogenesis is highly restricted [6]. Angiogenesis is the process of creating new blood vessels from existing vasculature. When tissue starts to grow rapidly, more blood vessels are created to supply nutrition to the fast-growing area, creating a lump of tissue or tumor. If the tumor does not invade the surrounding tissue and spread into other organs, then it is considered benign tumor. But the tumor contains cancer cells that grow aggressively and can attack nearby tissues or move into blood or lymph nodes, then the tumor is labeled as malignant [7].
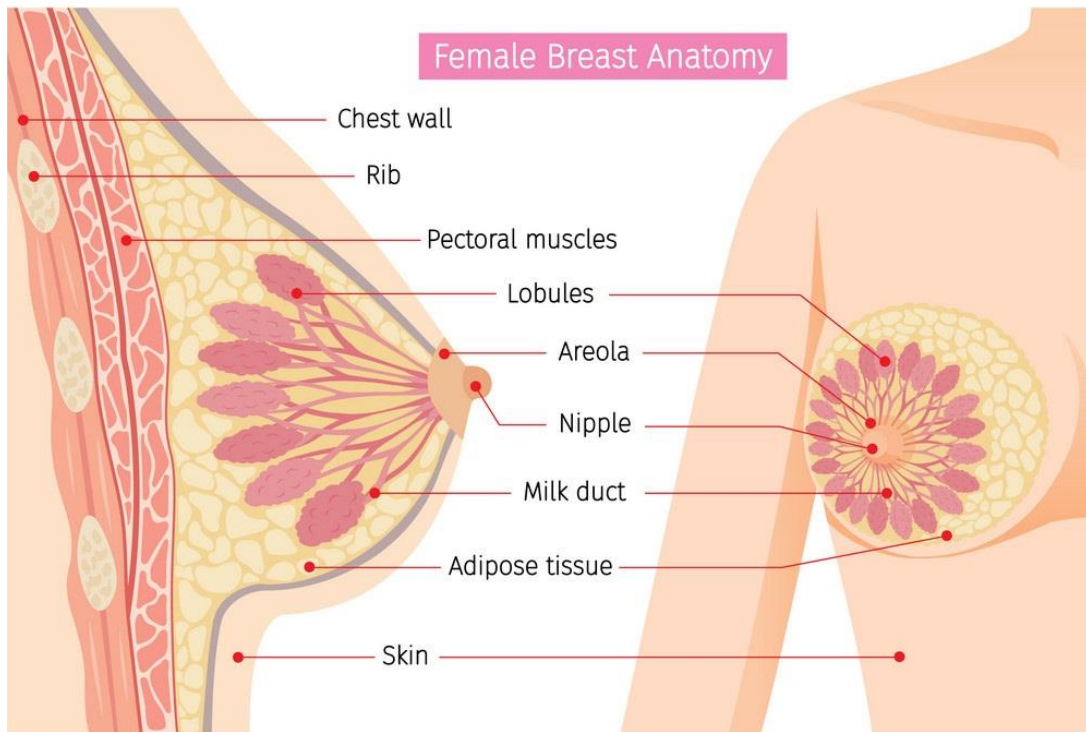
Figure 1.1: Female breast anatomy, with a side cross-sectional view on the left and a frontal cross-sectional view on right [4]

Breast cancers or malignant tumors are classified in different grades according to their growth rates and metabolic activity levels, which result in widely varying functional characteristics [8]. Breast cancer can be ductal carcinoma, starting in a milk duct; lobular carcinoma, starting in a breast lobule; or inflammatory, where the breast appears swollen. Additionally, benign breast disease encompasses a heterogeneous group of lesions that vary in vascular content, proliferative index, and metabolic activity, all of which may or may not be associated with future risk of breast cancer [9]. Benign breast tumors can variously be a fibroadenoma, a solid tumor, and intraductal papilloma, a fluid filled cyst, or an area of fat necrosis. Breast cancer symptoms, on the other hand, may not be noticeable or visible without professional screening. A lump in the breast, a distorted

shape of the breast, a red and swollen nipple area, and discharge from the nipple might be symptoms of breast cancer [5].

Breast cancer incidence has steadily increased over the past decade with a rate of 0.3% annually [2]. But the breast cancer death rate decreased by 1.3% per year from 2013 to 2017. Figure 1.2 shows the breast cancer incidence rate for 15 years, from 2001 to 2016, and the survival rate for 31 years, from 1976 to 2017. Increased awareness, better diagnostic methods, and improvement treatment have all helped to reduce the death rate. Despite the advances in diagnostic methods, hundreds of thousands of biopsies are performed each year, but most of them prove unnecessary, yielding benign results [10]. So, Better diagnostic tools are needed to reduce false positives in the clinical management of breast cancer.

(a) Breast Cancer Incidence Rate   (b) Breast Cancer Survival Rate
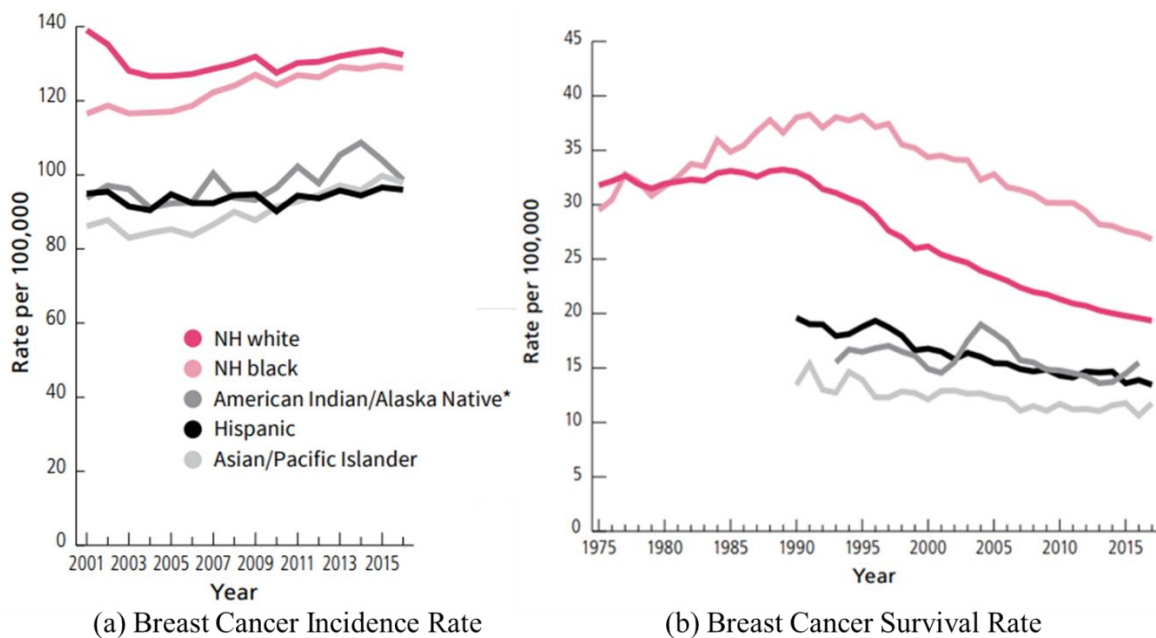
Figure 1.2: Breast cancer statistics (a) breast cancer incidence rate over 15 years and (b) survival rate over 31 years, (NH for Non-Hispanic) [2].

1.1.1 Breast Cancer Risk Factors

Risk factors are not definite indicators of breast cancer; rather they are associated with the probability of having breast cancer. Risk factors can be related to one's genetics, family history, age, weight, physical activities, diet, menopausal state, and many other conditions [11]. Our age and genetics are beyond our control, but breast cancer risk increases with age and a history of breast cancer in immediate family members. Alcohol consumption is associated with a moderate increase of breast cancer. Daily consumption of 10 g alcohol (one serving) can increase cancer risk by 10%; while 30g per day can increase the risk by as much as 30% [12]. Menopausal age is also associated with breast cancer risk. A postmenopausal woman will have a higher risk of breast cancer than a premenopausal woman of the same age. Some factors lower the risk of the breast cancer. Though childbearing can increase cancer risk immediately after birth, it later protects against breast cancer [13-14]. Women who have had at least one full term pregnancy, have a 25% lower risk of breast cancer than women who never were pregnant [14]. Moderate exercise and a healthy diet containing fruits, vegetables, meat, and fiber can reduce the risk of cancer. Breastfeeding helps to reduce risk of pregnancy, too. Women who had breastfed a total of 25 months had a 33% lower risk of cancer than women who never breastfed [13].

1.1.2 Breast Cancer Staging

Based on the growth and size of the tumor, breast cancer can be classified into different stages using the Manchester classification or the International TNM classification [4]. According to Manchester classification, breast cancer is diagnosed as Stage I, II, III, or IV cancer based on the cancer's progress and growth. Stage I cancer is confined in an organ, with no palpable axillary lymph node. Stage II cancer is also regional, or growth is limited to a region only, but with a palpable axillary lymph node. Stage III cancer is locally advanced cancer which has penetrated to

6

other tissues, such as the skin, chest wall muscles, or ribs. Stage IV is the final metastatic stage of cancer. Metastasis is the process of tumor progression into distant areas of the body, e.g., bones, the liver, and the kidneys [15]. TNM classification is based on tumor size (T for tumor), presence of palpable axillary nodes (N for node), and metastasis (M for metastasis). A tumor, with a diameter less than 2 cm, is classified as T1; with a diameter of 2 to 5 cm, it is T2; with a diameter of 5 to 10 cm, it is T3; and with a diameter greater than 10 cm, it is T4. Axillary nodes can be N0 with no palpable axillary nodes, N1 with regional mobile axillary nodes, N2 with regional fixed nodes and N3 with cancer in internal mammary lymph nodes. Metastatic state M0 refers to no metastasis, and M1 signifies a distance metastasis. As an example, T1-N0-M0 would mean that patient has a tumor with diameter less than 2 cm, no palpable axillary node, and locally confined with no distant metastasis.

1.1.3 Breast Cancer Diagnostic Methods

Different diagnostic methods have been used for breast cancer diagnosis over the past three decades including but not limited to x-ray mammography, ultrasound (US), magnetic resonance imaging (MRI), position emission tomography (PET), computed tomography (CT), and biopsy. Biopsy is considered the gold standard for cancer diagnosis [16-19], but it is very costly and not applicable for rapidly repeated screening. X-ray mammography is routinely used in breast cancer screening. While X-rays have excellent spatial resolution and imaging depth, their ionizing radiation might increase the breast cancer risk [20]. PET presents a radiation problem too [19]. MRI has good resolution and imaging depth and does not pose an ionizing radiation problem, but its data acquisition is slow, and the imaging is expensive [18]. Ultrasound offers a good tradeoff between imaging depth, resolution, and cost, and can provide real time imaging, but the functional contrast between solid benign and malignant tumors is poor for ultrasound [17]. Diffuse optical

imaging has also been investigated as a potential diagnostic tool over past few decades [21-51]. It has good imaging depth with excellent tissue contrast, fast data acquisition, a low cost, and non-ionizing radiation. The only problem with optical imaging is poor resolution, which can be improved by guiding the imaging using a high-resolution imaging modality [26-34]. Our lab investigated ultrasound guided diffuse optical tomography as a potential diagnostic tool for breast cancer [52-56].

1.2   Diffuse Optical Tomography

1.2.1   DOT Principles and Imaging

DOT is a noninvasive imaging modality that provides the optical properties of the object being imaged by using optical illumination in the diffusive regime [21]. The spatial resolution of DOT imaging is limited [22], but its good contrast mechanism, higher penetration depth, low cost, and high speed have established diffuse optical imaging as an alternative to conventional radiological imaging techniques. Near infrared light can penetrate several centimeters through the scalp, breast fat, and brain making a useful range of investigation. DOT image reconstruction involves both a forward and an inverse problem. The forward problem uses the diffusion equation to predict the distribution of reemitted light on the basis of presumed parameters for both the light and object. The inverse problem uses the forward problem to reconstruct the distribution of the optical properties of the object from a measured data set. The DOT forward and inverse problems will both be discussed in chapter two.

The operation of the imaging probe is based on the use of diffuse photon density waves. Diffused photon waves are scalar, overdamped traveling waves of photon density. They propagate through

turbid media such as breast tissue, wherein the transport of light energy density is governed by a diffusion equation. A light source with an intensity modulated at frequency ω generates a diffused photon density wave in an optically turbid medium. For a sinusoidally modulated source, the resultant diffusive wave obeys the Helmholtz equation. Detailed methods for solving the equation for an infinite medium are discussed in ref 2. we solve the equation for a semi-infinite boundary condition since we use a reflection geometry imaging probe. The probe is painted black with a nominal reflection coefficient of zero, which ensures light propagates only in one direction, towards the breast. The DOT forward problem is solved by using the Born approximation and the Green function to approximate a point source response [23].

DOT can operate in one of the three modes: time domain (TD), frequency domain (FD), and continuous wave (CW) or direct current. The time domain mode uses a short-pulsed laser beam and thus contains a broad frequency spectrum [24]. The frequency domain mode uses a source light of a single wavelength, modulated by a higher frequency signal. Time domain systems perform better than frequency domain systems in terms of optical crosstalk reduction but are more expensive than frequency domain systems [25]. CW systems use a constant current of zero frequency, which provides less information than FD systems but is much cheaper. A frequency domain system offers a good trade-off between data acquisition speed and accuracy of target quantification.

 In our lab, we use a frequency domain DOT imaging system. DOT suffers from poor lesion localization due to intense light scattering. To improve the target quantification and lesion localization, DOT is often guided by other high-resolution imaging modalities, referred as dual modality imaging method [26-34]. DOT can be guided by MRI [26-28], X-ray [29-30] or US [31-34]. Using high resolution imaging modalities, a lesion's location and dimensions can be

9

approximated, thus DOT can be confined to a smaller region of interest. US-guided DOT, as used in our lab, will be discussed in section 1.3.

1.2.2 Breast Cancer Diagnosis using DOT

Functional information, e.g., the hemoglobin concentration, oxygen concentration, and water and lipid concentrations of breast tissue are important in diagnosis of breast cancer. Thus, NIR DOT imaging, which provides this information, has been successfully used in breast cancer diagnosis over past two decades. Using NIR imaging, Colak et al. studied 10 patients with 5 benign and 5 malignant [35]. All 5 malignant cases were successfully diagnosed, while one fibroadenoma case was missed, resulting in an accuracy of 90%. Tromberg et al., introduced a frequency domain imaging system in 1997 which successfully diagnosed two patients, one having fibroadenoma and another having fluid filled cyst [36]. Thus, in this limited study, NIR imaging was capable of detecting both solid and fluid filled tumors. Using a CW system, Cheng et al. studied 50 human subjects for breast cancer diagnosis [37] and obtained a sensitivity of 92% and specificity of 67%. Van veen et al., reported a 74% accuracy among 24 breast cancer patients studied [38]. Too deep tumors and very small tumors (less than 10 mm in size) were excluded from the study. Taroni et al. studied 101 breast cancer patients using four wavelengths ranging from 683 to 975 nm [39]. They found 81% of the malignant tumors and 70% of the cysts were diagnosed correctly, while only 37% of the fibroadenoma and 33% of the other types of abnormalities were diagnosed correctly. Nioka et al. used a CW system to do spectroscopic measurements of 116 human subjects [40]. They reported a sensitivity of 96%, specificity of 93%, positive predictive value (PPV) of 89% and negative predictive value of 97%. Choe et al. used a parallel plate diffuse optical tomography system to image 51 lesions in 47 patients, out of which 41 were malignant and 10

were benign [41]. They showed a higher contrast for total hemoglobin, oxy hemoglobin and reduced scattering coefficient between the malignant and benign groups. A sensitivity of 98% and specificity of 90% were achieved. Mastanduno et al. studied 16 benign and 28 malignant breast tumors using MRI-guided DOT [28]. Two tailed t-test between the benign and malignant groups' total hemoglobin concentrations provide a p value of 0.0037, which was found to be significant. Fang et al. studied 189 breasts from 139 subjects [29]. Total hemoglobin in malignant tumor group was significantly greater than fibrograndular tissue with p-value of 0.0062, solid benign lesions with p-value of 0.025 and cystic lesions with p-value of 0.0033. Using an ultrasound guided DOT system, our lab, led by Dr Quing Zhu, studied 288 patients with 55 malignant lesions and 233 benign lesions [34]. We reported a sensitivity of 96.6%-100% and specificity of 77.3-83.3%.

1.2.3 Breast Cancer Treatment Monitoring using DOT

Beyond diagnosis, DOT has been widely used in chemotherapy response prediction. Change of functional parameters provided by DOT can be a good indicator of responder or non-responder patients. If the patient does not respond to chemotherapy, doctors need to change the chemo or adopt alternative treatment options. So, it's important to predict chemotherapy response as early as possible in the treatment cycle. Using diffuse optical spectroscopic measurements, Jakubowski et al. studied a 54-year-old postmenopausal Caucasian female with malignant tumor [42]. The total hemoglobin concentration in tumor area of the patient breast decreased by 56% in 10 weeks of treatment. Half of the decrease happened in the 1st week. DOT was successful to identify the patient as a responer in about a week. Using the same system in 2005, Tromberg et al. studied 12 premenopausal patients age ranging from 30 to 39 [43]. All patients were responders. Within one

week of treatment, tissue optical index decreased more than 50%. Tissue optical index was calculated using hemoglobin, water and lipid concentrations. Choe et al. studied a 35-year-old premenopausal patient with ductal carcinoma [44]. Her total hemoglobin concentration decreased from 21.4 μM to 9.1 μM in 12 weeks of treatment period. Her oxygen saturation, sO2, decreased sharply from 89% to 59% up to 5th chemotherapy cycle, and then did not vary much further. Zhou et al. studied a 45-year-old premenopausal Caucasian woman [45]. The patient was a responder and total hemoglobin concentration decreased after only 4 days of treatment; after 7 days, it was significantly lower. Cerussi et al. studied 11 patients, 6 responders and 5 non-responders [46]. For the 6 responders, total hemoglobin and oxy hemoglobin concentration decreased by 27% to 33% within 1 week of treatment, but these parameters did not vary much for the 5 non-responder cases. The total hemoglobin concentration was found to be the single best predictor, with a sensitivity of 85% and a specificity of 100%. By combining all predictors, a sensitivity of 100% and specificity of 100% were achieved. Jiang et al. studied 7 patients with 4 responders and 3 non-responders [47]. After 4 weeks of treatment, total hemoglobin decreased by 64.2% on average for responder group, but it increased by 16.1% on average for non-responder group. sO2 was found to be insignificant in chemotherapy response prediction. Soliman et al. studied 10 patients, with 5 responders and 4 non-responders, and 1 patient who responded after chemo change [48]. After 4 weeks of treatment, oxy and deoxy hemoglobin concentration decreased by 67.6% and 58.9% respectively for responder group, and 17.7% and 18% for non-responder group. Roblyer et al. studied 24 tumors from 23 patients with 11 partial responder, 8 complete responder and 5 non-responders [49]. After just day one of treatment, significant difference in oxy hemoglobin was observed between non-responder group and complete or partial responder group. Ueda studied 42 tumors, with 12 responders and 30 non-responders [50]. With a threshold of 76% for sO2, a

sensitivity of 75% and specificity of 73.3% were obtained from responder vs non-responder comparison. Combining estrogen receptor with sO2 further improved sensitivity to 100% and specificity to 85.7%. Jiang et al. studied 19 patients in 2014, with 9 responders and 10 non-responders [51]. Mean total hemoglobin reduction for responder group was 74%, and reduction for non-responder group was 43%.

1.3 Ultrasound guided Diffuse Optical Tomography

The Optical and Ultrasound Imaging Group in Department of Biomedical Engineering at Washington University in St Louis, is a pioneer in ultrasound guided optical imaging technologies, led Dr. Quing Zhu. We have developed frequency domain ultrasound guided DOT imaging systems and applied them in breast cancer diagnosis and neoadjuvant chemotherapy treatment monitoring over last two decades. In this section, I will briefly introduce the introduce the evolution of our DOT system and properties of our current DOT system used at the Washington University Medical School. DOT data acquisition and system calibration techniques are also discussed.

1.3.1 Evolution of US guided DOT

The first NIR DOT System was developed in 2001 by Dr. Quing Zhu [52]. The DOT system was frequency domain imaging system whose probe had 12 sources and 8 detectors. A dual wavelength laser diode was used as light source. Data was acquired at 780 and 830 nm. The Laser source output was modulated at 140 MHz . System design of the first-generation DOT system and its probe design are shown in Figure 1.3. The Noisy ultrasound image made it harder to localize tumors with this system, which inspired the development of next generation systems. Second generation system solved the ultrasound noise problem by using a commercial ultrasound system

with the home-made DOT system [53]. Three laser diodes, at 690 nm, 780 nm and 830 nm, were the light sources. There were 9 sources and 12 detectors was A National instruments data acquisition card (NI-DAQ) was used to acquire data, which greatly enhanced the signal to noise ratio. But NI-DAQ card was bulky, data acquisition was very slow, and the system has also had source-detector coupling noises.
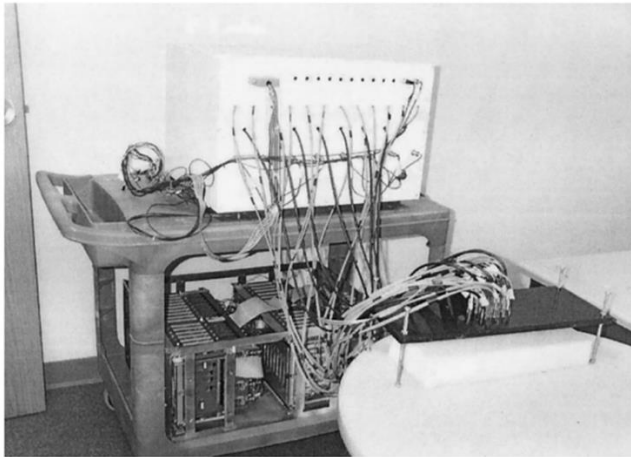
(a) 1st generation DOT System
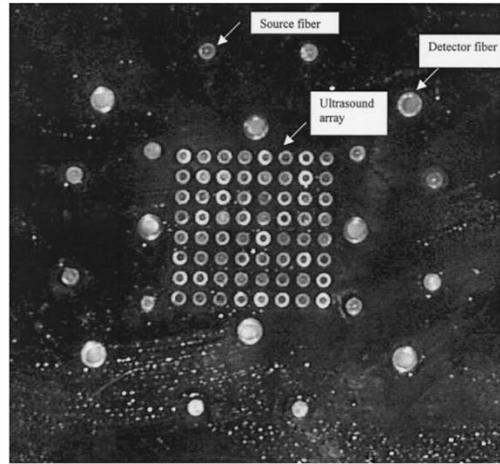
(b) 1st generation DOT Probe

Figure 1.3: First generation (a) DOT system (b) imaging probe [52]

Design of the third-generation DOT system accelerated the DOT data acquisition speed by replacing by NI-DAQ board with an FPGA-based data acquisition card [54]. The number of laser diodes was increased to four, with wavelengths of 740,780, 808 and 830 nm. The number of detector channels was increased to 14, compared to the 10 in second-generation system. Optical isolators were used for noise reduction. Custom made software was developed for data acquisition.

The fourth-generation DOT system [55], which is currently used in our research, is similar to the third-generation system in principle and features. Figure 1.4 shows the current US guided DOT imaging system and setup with the probe design. Four laser diodes with wavelengths of 740, 780,

808, and 830 nm are sequentially switched by a 4×1 and a 1×9 optical switch to deliver light modulated at 140 MHz to each of the nine source positions on the probe. Fourteen parallel photomultiplier tubes (PMTs) detect reflected light via light guides from the tissue. A custom A/D board samples detected signals from all channels and stores data in a PC.

One important difference is that the laser control and detector gain control are all automated and integrated in the software now. The system is portable, and the probe design is optimized to avoid photomultiplier saturation.
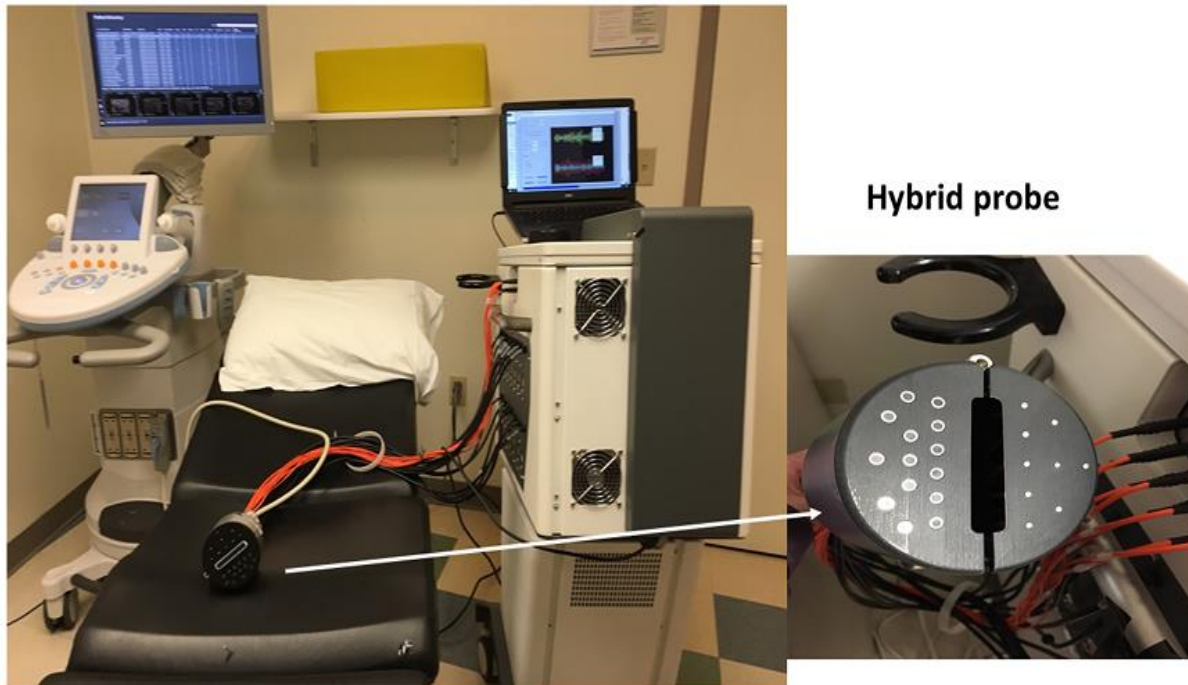
Figure 1.4: Portable NIR DOT System with handheld imager. Smaller circles on the probe are sources, and larger circles are detectors; the hole in the middle is used to insert a US transducer [4].

1.3.2 DOT Data Acquisition and System Calibration

One of the challenges encountered in the design of a NIR imaging system is the huge dynamic range of signals received at various source–detector distances. For example, for a semi-infinite phantom made of 0.5% intralipid solution, the amplitude measured at 1 cm away from a source is approximately 5000 times larger than that at 8 cm separation. In addition, perturbation due to embedded heterogeneities with optical properties similar to a tumor is normally a few percent of the background signal. So, for each detector channel, we vary the photomultiplier (PMT) gain to reduce the dynamic range of the signal. After the data acquisition, we have to calibrate the gain and phase shift of the data, which is referred as system calibration. In our imaging system, we collect three types of data: intralipid, reference, and target data. Intralipid data is collected from a homogeneous intralipid solution that is used in system calibration. Reference data is collected from the normal patient's breast, and target data is collected from the breast with a lesion. Reference breast is assumed to be homogeneous. For heterogeneous dense breasts, reference smoothing is done [56]. The calibration process is discussed in detail in ref [52]. In short, the detected amplitude, A_{sd} and phase, ϕ_{sd} of the signal are related to the source detector distance, ρ_{sd}, between source, s, and detector, d:

$$\log[\rho_{sd}^2 A_{sd}] = \log[I_s] + \log[I_d] - k_i\rho_{sd} \text{ , and}$$

$$\phi_{sd} = \phi_s + \phi_d + k_r\rho_{sd} \quad \text{, s=1,2 ...m, and d=1,2, ... n,} \qquad \text{Eq (1.1)}$$

where m and n are the number of sources and detectors, I_s and I_d are gains for the source and detector, ϕ_s and ϕ_d are the source and detector phase shifts. k_i and k_r are the imaginary and real part of wavenumber k. For both gain and phase shift calculation, we will have m×n number of equations for m source and n detectors, but only m+n+1 number of unknowns to reconstruct.

16

Usually m+n+1<m×n, so this problem is overdetermined. The least square solution gives the estimated system gains and phase shifts. Compensating for the system gain, we have

$$\log[\rho_{sd}^2 A_{sd}] = -k_i \rho_{sd} \text{ , and}$$

$$\phi_{sd} = k_r \rho_{sd} \quad \text{, s=1,2 …m, and d=1,2, … n.} \qquad \text{Eq (1.2)}$$

Examples of calibrated and uncalibrated signal for a homogeneous reference are shown in figure 1.5.

(a) Uncalibrated Amplitude (b) Calibrated Amplitude

(c) Uncalibrated Phase (b) Calibrated Phase
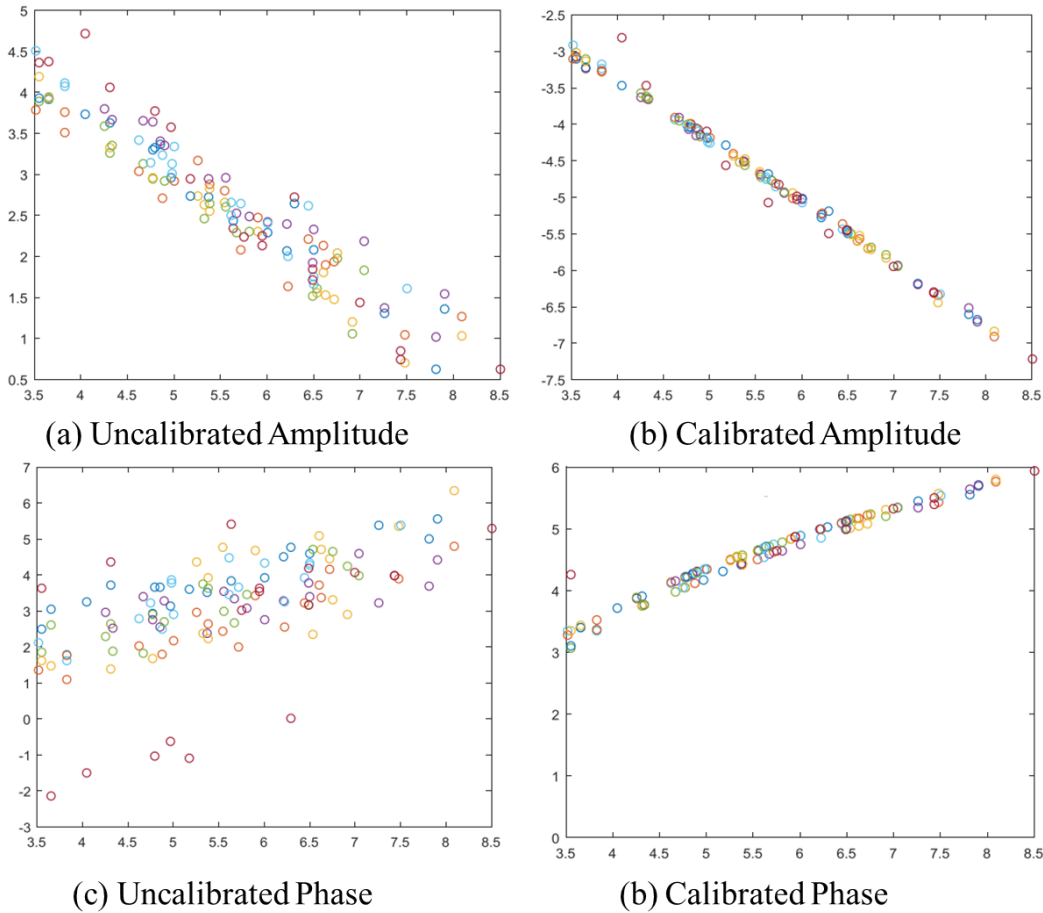
Figure 1.5: Measurement amplitude and phase before and after system calibration (a) Amplitude before calibration (b) Amplitude after calibration (c) Phase before calibration (d) Phase after calibration

17

Equation 1.3 establishes a linear relationship between the source-detector separation and the measured signal, as seen in figure 1.5 as well. The Slope of the fitted straight line from the amplitude and phase plot gives the wavenumber, k. We will discuss in Chapter 2 how we solve our forward problem using this fitted wavenumber from a reference breast.

References

1. National breast cancer foundation Inc, https://www.nationalbreastcancer.org/, 2020

2. American cancer society, https://www.cancer.org/cancer/breast-cancer/, 2020

3. Williams, Norman S., Christopher JK Bulstrode, and P. Ronan O'connell. Bailey & Love's short practice of surgery. Crc Press, 2008.

4. Female Breast Anatomy, VectorStock, 2020. https://www.vectorstock.com/royalty-free-vector/cross-section-of-female-breast-anatomy-vector-15819316

5. Black, John, Kevin G. Burnand, and William EG Thomas. Browse's Introduction to the Symptoms & Signs of Surgical Disease 4th Edition. CRC Press, 2005.

6. Fox, Stephen B., Daniele G. Generali, and Adrian L. Harris. "Breast tumour angiogenesis." Breast cancer research 9, no. 6 (2007): 216.

7. Essays, UK. (November 2018). History And Treatment Of Breast Cancer Biology Essay. Retrieved from https://www.ukessays.com/essays/biology/history-and-treatment-of-breast-cancer-biology-essay.php?vref=1

8. Polyak, Kornelia. "Heterogeneity in breast cancer." The Journal of clinical investigation 121, no. 10 (2011): 3786-3788.

9. Guray, Merih, and Aysegul A. Sahin. "Benign breast diseases: classification, diagnosis, and management." The oncologist 11, no. 5 (2006): 435-449.

10. The ASPE Technical Expert Panel on Improving Cancer Policy Research through Information Technology. The Importance of Radiology and Pathology Communication in the Diagnosis and Staging of Cancer: Mammography as a Case Study. November 2010.

11. Key, Timothy J., Pia K. Verkasalo, and Emily Banks. "Epidemiology of breast cancer." The lancet oncology 2, no. 3 (2001): 133-140.

12. Smith-Warner, Stephanie A., Donna Spiegelman, Shiaw-Shyuan Yaun, Piet A. Van Den Brandt, Aaron R. Folsom, R. Alexandra Goldbohm, Saxon Graham et al. "Alcohol and breast cancer in women: a pooled analysis of cohort studies." Jama 279, no. 7 (1998): 535-540.

13. Beral, Valerie, and Gillian Reeves. "Childbearing, oral contraceptive use, and breast cancer." Lancet (London, England) 341, no. 8852 (1993).

14. Layde, Peter M., Linda A. Webster, Andrew L. Baughman, Phyllis A. Wingo, George L. Rubin, Howard W. Ory, and Cancer and Steroid Hormone Study Group. "The independent associations of parity, age at first full term pregnancy, and duration of breastfeeding with the risk of breast cancer." Journal of clinical epidemiology 42, no. 10 (1989): 963-973.

15. Geiger, Thomas R., and Daniel S. Peeper. "Metastasis mechanisms." Biochimica et Biophysica Acta (BBA)-Reviews on Cancer 1796, no. 2 (2009): 293-308.

16. Wang, Lulu. "Early diagnosis of breast cancer." Sensors 17, no. 7 (2017): 1572.

17. Stavros, A. Thomas, David Thickman, Cynthia L. Rapp, Mark A. Dennis, Steve H. Parker, and Gale A. Sisney. "Solid breast nodules: use of sonography to distinguish between benign and malignant lesions." Radiology 196, no. 1 (1995): 123-134.

18. Kriege, Mieke, Cecile TM Brekelmans, Carla Boetes, Peter E. Besnard, Harmine M. Zonderland, Inge Marie Obdeijn, Radu A. Manoliu et al. "Efficacy of MRI and mammography for breast-cancer screening in women with a familial or genetic predisposition." New England Journal of Medicine 351, no. 5 (2004): 427-437.

19. Zangheri, Barbara, Cristina Messa, Maria Picchio, Luigi Gianolli, Claudio Landoni, and Ferruccio Fazio. "PET/CT and breast cancer." European journal of nuclear medicine and molecular imaging 31, no. 1 (2004): S135-S142.

20. Evans, John S., John E. Wennberg, and Barbara J. McNeil. "The influence of diagnostic radiography on the incidence of breast cancer and leukemia." New England Journal of Medicine 315, no. 13 (1986): 810-815.

21. Jiang, Huabei. Diffuse optical tomography: principles and applications. CRC press, 2018.

22. Wang, Lihong V., and Hsin-I. Wu. Biomedical optics: principles and imaging. John Wiley & Sons, 2012.

23. Huang, Minming, and Quing Zhu. "Dual-mesh optical tomography reconstruction method with a depth correction that uses a prioriultrasound information." Applied optics 43, no. 8 (2004): 1654-1662.

24. Keren, Shay, Olivier Gheysens, Craig S. Levin, and Sanjiv S. Gambhir. "A comparison between a time domain and continuous wave small animal optical imaging system." IEEE transactions on medical imaging 27, no. 1 (2007): 58-63.

25. Nissilä, Ilkka T., Jeremy C. Hebden, David Jennions, Jenni Heino, Martin Schweiger, Kalle M. Kotilahti, Tommi EJ Noponen et al. "Comparison between a time-domain and a frequency-domain system for optical tomography." Journal of biomedical optics 11, no. 6 (2006): 064015.

26. Brooksby, Ben, Brian W. Pogue, Shudong Jiang, Hamid Dehghani, Subhadra Srinivasan, Christine Kogel, Tor D. Tosteson, John Weaver, Steven P. Poplack, and Keith D. Paulsen. "Imaging breast adipose and fibroglandular tissue molecular signatures by using hybrid MRI-guided near-infrared spectral tomography." Proceedings of the National Academy of Sciences 103, no. 23 (2006): 8828-8833.

27. Ntziachristos, Vasilis, A. G. Yodh, Mitchell D. Schnall, and Britton Chance. "MRI-guided diffuse optical spectroscopy of malignant and benign breast lesions." Neoplasia (New York, NY) 4, no. 4 (2002): 347.

28. Mastanduno, Michael A., Junqing Xu, Fadi El-Ghussein, Shudong Jiang, Hong Yin, Yan Zhao, Kelly E. Michaelsen et al. "Sensitivity of MRI-guided near-infrared spectroscopy clinical breast exam data and its impact on diagnostic performance." Biomedical optics express 5, no. 9 (2014): 3103-3115.

29. Fang, Qianqian, Juliette Selb, Stefan A. Carp, Gregory Boverman, Eric L. Miller, Dana H. Brooks, Richard H. Moore, Daniel B. Kopans, and David A. Boas. "Combined optical and X-ray tomosynthesis breast imaging." Radiology 258, no. 1 (2011): 89-97.

30. Krishnaswamy, Venkataramanan, Kelly E. Michaelsen, Brian W. Pogue, Steven P. Poplack, Ian Shaw, Ken Defrietas, Ken Brooks, and Keith D. Paulsen. "A digital x-ray tomosynthesis coupled near infrared spectral tomography system for dual-modality breast imaging." Optics express 20, no. 17 (2012): 19125-19136.

31. Zhu, Quing, Edward B. Cronin, Allen A. Currier, Hugh S. Vine, Minming Huang, NanGuang Chen, and Chen Xu. "Benign versus malignant breast masses: optical differentiation with US-guided optical imaging reconstruction." Radiology 237, no. 1 (2005): 57-66.

32. Zhu, Quing, Poornima U. Hegde, Andrew Ricci Jr, Mark Kane, Edward B. Cronin, Yasaman Ardeshirpour, Chen Xu et al. "Early-stage invasive breast cancers: potential role of optical tomography with US localization in assisting diagnosis." Radiology 256, no. 2 (2010): 367-378.

33. Zhu, Quing, Patricia A. DeFusco, Andrew Ricci Jr, Edward B. Cronin, Poornima U. Hegde, Mark Kane, Behnoosh Tavakoli, Yan Xu, Jesse Hart, and Susan H. Tannenbaum. "Breast cancer: assessing response to neoadjuvant chemotherapy by using US-guided near-infrared tomography." Radiology 266, no. 2 (2013): 433-442.

34. Zhu, Quing, Andrew Ricci Jr, Poornima Hegde, Mark Kane, Edward Cronin, Alex Merkulov, Yan Xu, Behnoosh Tavakoli, and Susan Tannenbaum. "Assessment of functional differences in malignant and benign breast lesions and improvement of diagnostic accuracy by using US-guided diffuse optical tomography in conjunction with conventional US." Radiology 280, no. 2 (2016): 387-397.

35. Colak, S. B., M. B. Van der Mark, G. W. t Hooft, J. H. Hoogenraad, E. S. Van der Linden, and F. A. Kuijpers. "Clinical optical tomography and NIR spectroscopy for breast cancer detection." IEEE Journal of selected topics in quantum electronics 5, no. 4 (1999): 1143-1158.

36. Tromberg, Bruce J., Olivier Coquoz, Joshua B. Fishkin, Tuan Pham, Eric R. Anderson, John Butler, Mitchell Cahn, Jeffrey D. Gross, Vasan Venugopalan, and David Pham. "Non–invasive measurements of breast tissue optical properties using frequency–domain photon migration." Philosophical Transactions of the Royal Society of London B: Biological Sciences 352, no. 1354 (1997): 661-668.

37. Cheng, Xuefeng, Jian-min Mao, Robin Bush, Daniel B. Kopans, Richard H. Moore, and Maryann Chorlton. "Breast cancer detection by mapping hemoglobin concentration and oxygen saturation." Applied optics 42, no. 31 (2003): 6412-6421.

38. Van Veen, R. L. P., Henricus JCM Sterenborg, A. W. K. S. Marinelli, and M. Menke-Pluymers. "Intraoperatively assessed optical properties of malignant and healthy breast tissue used to determine the optimum wavelength of contrast for optical mammography." Journal of biomedical optics 9, no. 6 (2004): 1129-1136.

39. Taroni, Paola, Gianmaria Danesini, Alessandro Torricelli, Antonio Pifferi, Lorenzo Spinelli, and Rinaldo Cubeddu. "Clinical trial of time-resolved scanning optical mammography at 4 wavelengths between 683 and 975 nm." Journal of biomedical optics 9, no. 3 (2004): 464-473.

40. Nioka, S., and B. Chance. "NIR spectroscopic detection of breast cancer." Technology in cancer research & treatment 4, no. 5 (2005): 497-512.

41. Choe, Regine, Soren D. Konecky, Alper Corlu, Kijoon Lee, Turgut Durduran, David R. Busch, Saurav Pathak et al. "Differentiation of benign and malignant breast tumors by in-vivo three-dimensional parallel-plate diffuse optical tomography." Journal of biomedical optics 14, no. 2 (2009): 024020-024020.

42. Jakubowski, Dorota B., Albert E. Cerussi, Natasha Shah, David Hsiang, John Butler, and Bruce J. Tromberg. "Monitoring neoadjuvant chemotherapy in breast cancer using quantitative diffuse optical spectroscopy: a case study." Journal of biomedical optics 9, no. 1 (2004): 230-238.

43. Tromberg, Bruce J., Albert Cerussi, Natasha Shah, Montana Compton, Amanda Durkin, David Hsiang, John Butler, and Rita Mehta. "Diffuse optics in breast cancer: detecting tumors

in pre-menopausal women and monitoring neoadjuvant chemotherapy." Breast Cancer Research 7, no. 6 (2005)

44. Choe, Regine, Alper Corlu, Kijoon Lee, Turgut Durduran, Soren D. Konecky, Monika Grosicka-Koptyra, Simon R. Arridge et al. "Diffuse optical tomography of breast cancer during neoadjuvant chemotherapy: a case study with comparison to MRI." Medical physics 32, no. 4 (2005): 1128-1139.

45. Zhou, Chao, Regine Choe, Natasha Shah, Turgut Durduran, Guoqiang Yu, Amanda Durkin, David Hsiang et al. "Diffuse optical monitoring of blood flow and oxygenation in human breast cancer during early stages of neoadjuvant chemotherapy." Journal of biomedical optics 12, no. 5 (2007): 051903.

46. Cerussi, Albert, David Hsiang, Natasha Shah, Rita Mehta, Amanda Durkin, John Butler, and Bruce J. Tromberg. "Predicting response to breast cancer neoadjuvant chemotherapy using diffuse optical spectroscopy." Proceedings of the National Academy of Sciences 104, no. 10 (2007): 4014-4019.

47. Jiang, Shudong, Brian W. Pogue, Colin M. Carpenter, Steven P. Poplack, Wendy A. Wells, Christine A. Kogel, Jorge A. Forero et al. "Evaluation of breast tumor response to neoadjuvant chemotherapy with tomographic diffuse optical spectroscopy: case studies of tumor region-of-interest changes." Radiology 252, no. 2 (2009): 551-560.

48. Soliman, Hany, Anoma Gunasekara, Mary Rycroft, Judit Zubovits, Rebecca Dent, Jacqueline Spayne, Martin J. Yaffe, and Gregory J. Czarnota. "Functional imaging using diffuse optical spectroscopy of neoadjuvant chemotherapy response in women with locally advanced breast cancer." Clinical Cancer Research 16, no. 9 (2010): 2605-2614.

49. Roblyer, Darren, Shigeto Ueda, Albert Cerussi, Wendy Tanamai, Amanda Durkin, Rita Mehta, David Hsiang et al. "Optical imaging of breast cancer oxyhemoglobin flare correlates with neoadjuvant chemotherapy response one day after starting treatment." Proceedings of the National Academy of Sciences 108, no. 35 (2011): 14626-14631.

50. Ueda, Shigeto, Darren Roblyer, Albert Cerussi, Amanda Durkin, Anais Leproux, Ylenia Santoro, Shanshan Xu et al. "Baseline tumor oxygen saturation correlates with a pathologic complete response in breast cancer patients undergoing neoadjuvant chemotherapy." Cancer research 72, no. 17 (2012): 4318-4328.

51. Jiang, Shudong, Brian W. Pogue, Peter A. Kaufman, Jiang Gui, Michael Jermyn, Tracy E. Frazee, Steven P. Poplack, Roberta DiFlorio-Alexander, Wendy A. Wells, and Keith D. Paulsen. "Predicting breast tumor response to neoadjuvant chemotherapy with diffuse optical spectroscopic tomography prior to treatment." Clinical Cancer Research 20, no. 23 (2014): 6006-6015.

52. Chen, Nan Guang, Puyun Guo, Shikui Yan, Daqing Piao, and Quing Zhu. "Simultaneous near-infrared diffusive light and ultrasound imaging." Applied optics 40, no. 34 (2001): 6367-6380.

53. Zhu, Quing, Chen Xu, Puyun Guo, Andres Aguirre, Baohong Yuan, Fei Huang, Diego Castilo et al. "Optimal probing of optical contrast of breast lesions of different size located at different depths by US localization." Technology in cancer research & treatment 5, no. 4 (2006): 365-380.

54. Xu, Chen, Hamed Vavadi, Alex Merkulov, Hai Li, Mohsen Erfanzadeh, Atahar Mostafa, Yanping Gong, Hassan Salehi, Susan Tannenbaum, and Quing Zhu. "Ultrasound-guided diffuse optical tomography for predicting and monitoring neoadjuvant chemotherapy of breast cancers: recent progress." Ultrasonic imaging 38, no. 1 (2016): 5-18.

55. Vavadi, Hamed, Atahar Mostafa, Feifei Zhou, KM Shihab Uddin, Murad Althobaiti, Chen Xu, Rajeev Bansal, Foluso Ademuyiwa, Steven Poplack, and Quing Zhu. "Compact ultrasound-guided diffuse optical tomography system for breast cancer imaging." Journal of biomedical optics 24, no. 2 (2018): 021203.

56. Vavadi, Hamed, and Quing Zhu. "Automated data selection method to improve robustness of diffuse optical tomography for breast cancer imaging." Biomedical optics express 7, no. 10 (2016): 4007-4020.

Chapter 2: Two Step Imaging Reconstruction for US guided DOT

2.1 Introduction

DOT reconstruction problem is ill-posed and often underdetermined due to smaller number of measurements compared to number of unknown properties to be reconstructed and intense scattering of light in diffusive regime. A variety of image reconstruction methods have been employed to improve target reconstruction accuracy in DOT. This includes the algebraic reconstruction technique (ART) [1], nonlinear iterative gradient based optimization methods [2-4], and Newton-like methods that requires the direct calculation and inversion of the Jacobian or weight matrix [5-6]. Reconstruction methods using a prior information determined from co-registered high-resolution MRI [7-9], x-ray imaging [10-11], and ultrasound imaging (US) [12-13] have been investigated extensively. These methods segment the lesion and background regions, or different tissue types seen by a high-resolution modality, and therefore reduce voxels with unknown optical properties and improve the ill-posed and underdetermined DOT reconstruction problem. Another means of incorporating a prior information into an iterative image reconstruction method is through the initial image estimate. Behnoosh and Zhu proposed a two-step reconstruction using Genetic Algorithm (GA) to find a suitable initial image estimate that was subsequently refined by use of a conjugate gradient (CG) method, which showed improved target quantification as compared to CG with zero initial estimate [14]. However, GAs are time-consuming and an optimal CG stopping criterion for use with experimental data is difficult to specify.

In this chapter, a simple two-step reconstruction method that can produce useful image estimates in DOT is proposed and investigated. In the first step, a truncated Moore-Penrose Pseudoinverse (MPP) solution is computed to obtain a preliminary estimate of the target image that can be reliably determined from the measured data; subsequently, this preliminary estimate is incorporated into the design of a penalized least squares estimator that is employed to compute the final image estimate. The MPP was employed to compute the initial estimate of the target image for several reasons. Firstly, the MPP pseudoinverse, by definition, produces the least-squares estimate of the image that possess the minimum norm. This yields a solution that can be interpreted as an orthogonal projection of the true target image onto a subspace that is the orthogonal complement to the null space of the imaging operator. Therefore, the MPP solution describes the estimate of the target that is closest to the true target but contains no component in the null space. This is a reliable strategy for image reconstruction when no reliable a priori information about the target is available. Secondly, the MPP pseudoinverse solution can be easily regularized by excluding contributions that correspond to small values. Therefore, there is little ambiguity in how to choose the regularization parameter. Thirdly, the MPP pseudoinverse operator for our system can be explicitly stored in memory, which leads to near real-time image reconstruction. By use of phantom data, the proposed method was demonstrated to yield more accurate images than those produced by conventional reconstruction methods. The method was also evaluated with clinical data that included 10 benign and 10 malignant cases. The capability of reconstructing high contrast malignant lesions was demonstrated to be improved by use of the proposed method. Methods and results of this chapter are adopted from my published article in biomedical optics express [13].

2.2 Materials and methods

2.2.1 DOT Forward Problem

The propagation of light through tissue is described by radiative transfer equation (RTE) [15-17]. For computational efficiency an approximation of RTE is used for diffused photon, which is known as diffusion equation [18]. The propagation of diffused light through tissue can be described by photon diffusion approximation as :

$$\left[\nabla^2 + k^2\right]U(r) = -\frac{1}{D}S(r), k^2 = \frac{-\upsilon\mu_a + jw}{D}, \quad D = \frac{1}{3\mu_s'}, \qquad \text{Eq. (2.1)}$$

where $S(r)$ is the equivalent isotropic source and, $U(r)$ is the photon density wave, D is the diffusion coefficient, μ_a and μ_s' are the absorption and reduced scattering coefficients, respectively. k is the wavenumber that we estimated from reference data as discussed in section 1.3. The inverse problem is typically linearized by Born approximation [18]. By digitizing the imaging space into N voxels, the resulted integral equations are formulated as following:

$$[U_{sc}]_{M\times 1} = [W]_{M\times N}[\delta\mu_a]_{N\times 1} = WX , \qquad \text{Eq. (2.2)}$$

where U_{sc} is the measured scattered photon density wave, M is the number of measurements, denotes the unknown changes of absorption coefficient at each voxel. The weight matrix, W, describes the distribution of diffused wave in the homogenous medium and characterizes the measurement sensitivity to the absorption and scattering changes.

2.2.2 DOT Inverse Problem

At the end, the inverse problem can be formulated as an unregularized optimization problem as:

29

$$f(x) = \arg\min_{X} \|U_{sc} - WX\|^2 \qquad\qquad \text{Eq. (2.3)}$$

In our ultrasound-guided DOT image reconstruction, a dual-zone mesh scheme is used to segment the imaging volume into a lesion region identified by co-registered US and a background region with fine and coarse voxel sizes, respectively [19]. This scheme effectively reduces the total number of voxels with unknown optical properties. The conjugate gradient (CG) method is utilized to iteratively solve the inverse problem. As a result, the target quantification accuracy can be significantly improved. However, when the lesions are larger, the total number of finer voxels and coarse voxels, N, can be much larger than the total measurements, M, which is the number of sources × the number of detectors × 2=14×9×2=252 counting for both amplitude and phase data. Due to the correlated nature of diffused light measured at closely spaced source and detector positions and also measurement noise, increasing the number of sources and detectors does not effectively mitigate the ill-conditioned nature of the DOT inversion problem.

In this manuscript, we formulate the inverse problem as:

$$f(x) = \arg\min_{X} (\ \|U_{sc} - WX\|^2 + \frac{\lambda}{2}\|(X - X^0)\|^2\ ), \qquad\qquad \text{Eq. (2.4)}$$

where X^0 is a preliminary estimate of the optical properties that can be reliably determined from the measured data and λ is a regularization parameter. A Newton-like or conjugate gradient optimization method will be employed to approximately solve Eq. (2.4). No spatial or temporal filters were used on solution $f(x)$.

2.2.3 Truncated pseudoinverse as an initial estimate

We propose to employ a truncated pseudoinverse (PINV) operator W_{PINV}^{-1} of W to form the preliminary estimate of X^0 as $X^0 = W_{PINV}^{-1} U_{sc}$, which appears in the second term in Eq. (2.4). According to singular value decomposition (SVD) theory, W can be decomposed as:

$$W = \sum_{n=1}^{R} \sqrt{\sigma_n} u_n v_n^\dagger ,$$ Eq. (2.5)

$\{u_n\}$ and $\{v_n\}$ are left and right singular vector of W or orthonormal eigenvector of $WW^\dagger$, $\{\sigma_n\}$ are nonzero eigenvalues of $W^\dagger W$ or $WW^\dagger$ and R is the number of nonzero singular values. MPP of W is,

$$W_{PINV}^{-1} = \sum_{n=1}^{R} \frac{1}{\sqrt{\sigma_n}} v_n u_n^\dagger$$ Eq. (2.6)

From system of linear equations, Eq.(2),

$$\tilde{X} = W_{PINV}^{-1} U_{sc} = \sum_{n=1}^{R} \frac{1}{\sqrt{\sigma_n}} v_n u_n^\dagger U_{sc}$$ Eq. (2.7)

Since our measurement contains noise, we assume additive noise n, $U_{sc} = U_{noiseless} + n$. Then the reconstructed absorption $\tilde{X}$ is given as:

$$\tilde{X} = W_{PINV}^{-1}(U_{noiseless} + n)$$

$$= X + X_{noise} , \quad X_{noise} = \sum_{n=1}^{R} \frac{1}{\sqrt{\sigma_n}} v_n u_n^\dagger n$$ Eq. (2.8)

For very small singular values $\sqrt{\sigma_n} \to 0$, X_{noise} may contain image artifacts.

In the truncated MPP approach, a threshold $\sqrt{\sigma_{th}}$ is set for singular values and the initial solution using MPP is:

$$X^0 = W_{PINV}^{-1} U_{sc} = \sum_{n=1}^{R'} \frac{1}{\sqrt{\sigma_n}} v_n u_n^\dagger U_{sc} , \quad \sqrt{\sigma_1}, \sqrt{\sigma_2}, \dots\dots\dots\dots \sqrt{\sigma_{R'}} \geq \sqrt{\sigma_{th}}$$ Eq. (2.9)

In the phantom and clinical data, we have chosen $\sqrt{\sigma_{th}}$ as 10% of $\sqrt{\sigma_1}$ as a cut off value. From the truncated pseudoinverse, a preliminary estimate of unknown optical properties can be obtained.

31

Pseudoinverse of forward imaging operator is also used for image reconstruction in fluorescence molecular tomography (FMT) [20], nuclear imaging [21] and photoacoustic imaging [22]. A simple projection operation is used to suppress pixels outside the region of interest identified by a sphere **B** obtained from measurements of co-registered ultrasound image. This projected absorption map is used as an initial solution for Newton or conjugate gradient search method.

2.2.4 Newton Method

The Newton method uses 2nd derivative of objective function (known as Hessian) to calculate a 2nd order search direction resulting in quadratic convergence rate. We reformulate our penalized least square problem as a quadratic optimization problem,

$$f(x) = \frac{1}{2}X^T Q X - b^T X - c$$

$$Q = 2W^T W + \lambda I \, , \quad b = 2W^T U_{sc} + \lambda X^0 \qquad \text{Eq. (2.10)}$$

Clearly, the hessian is positive definite when $\lambda > 0$. Our solution is iteratively updated using following equations,

$$X^{k+1} = X^k - \left(\nabla^2 f(X)\right)^{-1}\left(\nabla f(x)\right), \quad \nabla f(x) = QX - b, \quad \nabla^2 f(X) = Q \qquad \text{Eq. (2.11)}$$

The iteration process is terminated when change of objective function between successive iterations become smaller than a preset tolerance. Choice of the regularization parameter is a critical part of solution design. Based on tumor size measured from ultrasound image and largest singular value of weight matrix, σ_1 we empirically chose our regularization parameter as $\lambda = p\sqrt{\sigma_1}$, where p is proportional to tumor size.

2.2.5 Conjugate Gradient Method

The Conjugate gradient (CG) method is a well-known iterative technique for solving symmetric positive definite linear systems of equations. We investigated this method both with regularization and without regularization. For the unregularized optimization formulation as given in Eq. (3), W is only positive semi-definite because it possesses singular values that take on zero values. From phantom experiments using absorbers with known optical properties, we determined 3 iterations as a stopping criterion because the reconstructed absorption coefficients are close to known values. For the regularized least square formulation $Q = 2W^T W + \frac{1}{2}\lambda I$, and Q is, by construction, symmetric and positive semi-definite. For any choice of $\lambda > 0$, Q will be a positive definite matrix since the lower bound for the singular values of Q is $\frac{\lambda}{2}$. Again, $\lambda = p\sqrt{\sigma_1}$, is chosen with p proportional to the target size measured from US. The algorithm for implementing the CG method is adapted from Ref. 23.

2.2.6 Comparison of five reconstruction methods

Five reconstruction methods have been compared using phantom and clinical data. Using zero as an initial estimate of target optical properties and regularized Newton optimization (Newton Zero initial) and regularized CG optimization (CG Zero initial); using PINV as an initial estimate of target optical properties and regularized Newton optimization (Newton PINV initial), regularized CG optimization (CG PINV initial), and using zero initial estimate and unregularized CG. Additionally, target centroid error i.e. the absolute difference between the center of a phantom target measured by co-registered US and the centroid of corresponding reconstructed target absorption map, is calculated as a measure of reconstruction quality.

2.2.7 Choice of regularization

Proper choice of regularization parameter, λ, is an important part of reconstruction. If λ is too small, then penalty may not have any effect on reconstruction, however, a larger λ heavily penalizes data fidelity term and solution may not converge near true minimum of unconstrained objective function. In our approach, λ is chosen as $\lambda = p\sqrt{\sigma_1}$. Table 2.1 shows the λ/σ_n, n=1,2,3,4, as function of μ_{s0}' with μ_{a0} as parameters. The target size is 3 cm and the first four eigenvalues are about the threshold σ_{th}. λ/σ_n decreases with μ_{s0}' of background μ_{a0} and μ_{s0}' (see table 4) and typical target size of p from 1 to 5 cm, λ is a few percent of first two largest eigenvalues of Q matrix (Eq. 2.11) for different combination. Thus our regularization is such a way that our solution is regularized more when background absorption increases, since it will be difficult to a reliable estimate from iterative update.

Table 2.1: Ratio of Regularization parameter, λ to first four eigenvalues of Q

μ_{a0}	μ_{s0}'	λ/σ_1	λ/σ_2	λ/σ_3	λ/σ_4
0.01	4-9	0.65-1.39%	6.4-15.8%	17.1-31.7%	19.6-40.3%
0.02	4-9	0.69-1.44%	6.5-15.9%	17.3-31.1%	19.5-41.2%
0.03	4-9	0.74-1.50%	6.7-15.9%	17.2-32.3%	19.2-41.4%
0.04	4-9	0.78-1.55%	6.8-15.9%	16.9-32.3%	18.7-41.2%
0.05	4-9	0.82-1.52%	6.9-15.8%	16.7-32.3%	18.3-40.8%
0.06	4-9	0.86-1.64%	7.0-15.7%	16.4-32.2%	17.8-40.4%
0.07	4-9	0.90-1.69%	7.0-15.8%	15.7-31.8%	17.0-39.3%
0.08	4-9	0.94-1.73%	7.1-15.7%	15.7-31.8%	17.4-39.8%

2.3 Results

2.3.1 Phantom experiment results

Phantom experiments were performed with solid ball phantoms of different sizes and different optical contrasts emulating tumors. These targets were submerged in 0.08% intralipid solution of μ_a in the range of 0.02-0.03 cm^{-1} and μ'_s in the range of 7 to 8 cm^{-1} emulating homogeneous background tissue. We use 3 different size solid balls with diameters of 1, 2 and 3 cm submerged in depths of 1.5 cm to 3 cm in 0.5 cm step in depth. The calibrated high and low contrast phantoms were $\mu_a = 0.23\ cm^{-1}$ and $\mu_a = 0.11\ cm^{-1}$ mimicking malignant and benign lesions, respectively. An absorption map for each target location, size and contrast was reconstructed and maximum μ_a is obtained for quantitative comparison. An average reconstructed maximum μ_a from all target conditions using Newton Zero initial, Newton PINV initial, CG Zero initial, CG PINV initial and unconstrained CG are given in Table 2.2 and shown in figure 2.1. Errors of both high and low contrast targets reconstructed using different methods are given in Table 2.3. As seen from the Table, Newton and CG with PINV as an initial accurately estimate absorption coefficient while Newton and CG with a zero initial produce larger errors. Unconstrained CG gives a better estimate for high contrast phantoms but results in under reconstruction for low contrast ones.

Table 2.2: Maximum reconstructed absorption (cm⁻¹) (mean ± standard deviation) for phantom

	Newton with zero Ini	Newton with PINV ini	CG with zero ini	CG with PINV ini	CG unconstrained
Error (high contrast)	0.097 ± 0.018	0.099 ± 0.016	0.093 ± 0.012	0.100 ± 0.017	0.107 ± 0.069
Error (low contrast)	0.191 ± 0.042	0.229 ± 0.021	0.191 ± 0.041	0.228 ± 0.021	0.222 ± 0.027

Table 2.3: Errors in reconstructed absorption coefficient using different method

	Newton with zero Ini	Newton with PINV ini	CG with zero ini	CG with PINV ini	CG unconstrained
Error (high contrast)	11.6±13.8%	0.04±9.1%	11.8±13.2%	0.1±9.0%	3.5±9.9%
Error (low contrast)	12.0±16.1%	9.6±14.6%	15.6±10.9%	8.8±15.8%	26.5±8.5%
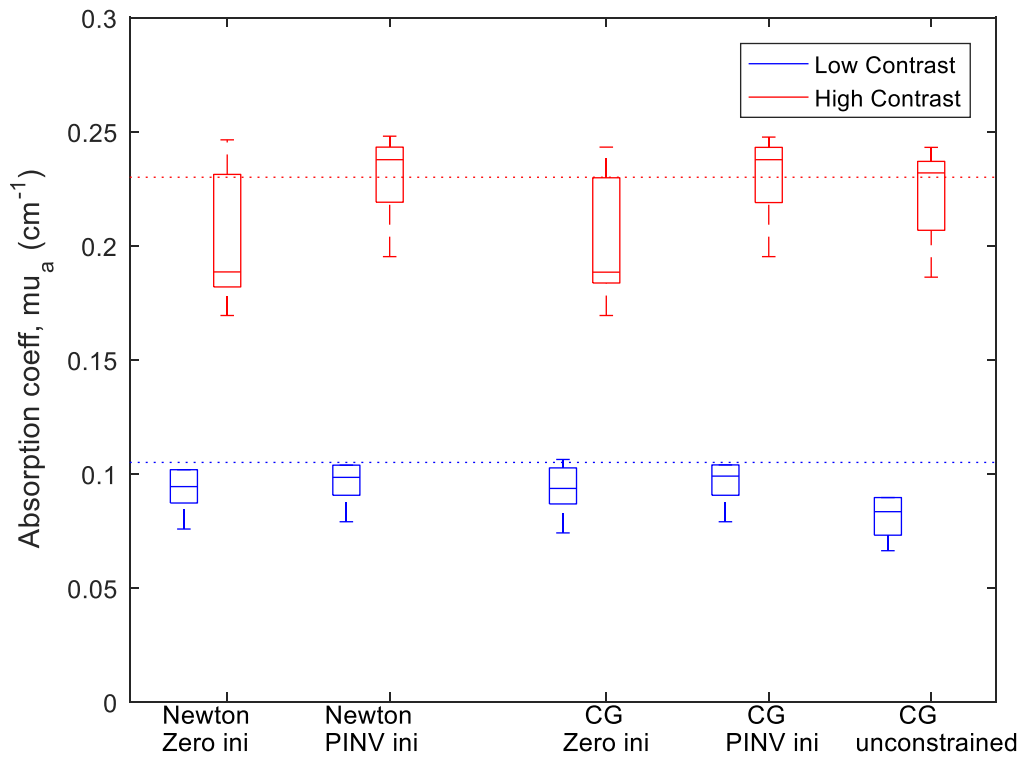
Figure 2.1:   Box plot of phantom data obtained from 1 to 3 cm size absorbers of high contrast (red) and low contrast (blue) located at different depths (1.5-3.5cm center depth) using zero and PINV as an initial guess and Newton as optimization, respectively (first and second columns), zero and PINV as initial guess and CG, respectively (third and fourth columns), and unconstrained CG (last column)

2.3.2 Clinical study

Performance of proposed method is demonstrated using clinical data obtained from 20 patients [12]. Based on biopsy results, 10 patients had benign lesions and 10 patients had cancers. The study was approved by the local Institution Review Boards (IRB) and was compliant with the Health Insurance Portability and Accountability Act (HIPPA). Informed consent was given by each patient. Data used in this study have been de-identified.

An example of a cancer case is shown in Figure 2.2. Figure 2.2 (a) is the co-registered US image with the suspicious lesion marked by a circle. Absorption maps of PINV initial image from truncated PINV (b) and reconstructed images using Newton with zero initial (c), PINV initial (d), CG with zero initial (e), CG with PINV initial (f) and unregularized CG (g) have shown similar lesion position and shape, however, the Newton's method with PINV initial yields highest reconstructed μ_a=0.268 cm^{-1}. Each map shows 7 sub-images marked as slice 1 to 7 and each sub-image shows spatial x and y distribution of absorption coefficients reconstructed from 0.5 cm to 3.5 cm depth range from the skin surface. The spacing between the sub-images in depth is 0.5 cm. The color bar is absorption coefficients in cm^{-1}. We chose the μa display range from 0 to 0.2 cm^{-1} because most of the reconstructed absorption values fall within this range. Each subfigure dimension is 8cm x 8cm with scales from -4 cm to 4 cm in both X and Y axis.

(a)

(b)

(c)

(d)

(e)

(f)

(g)

38
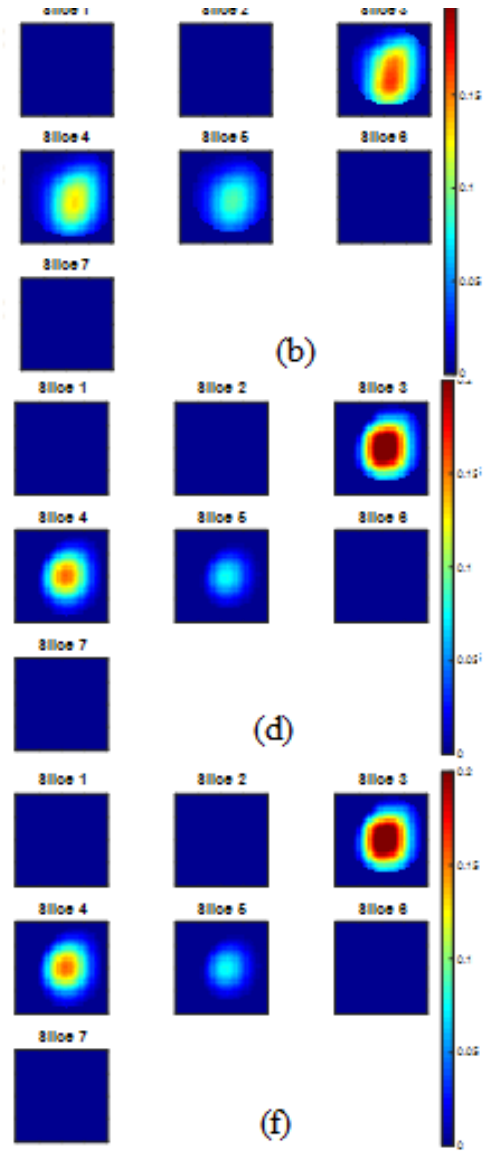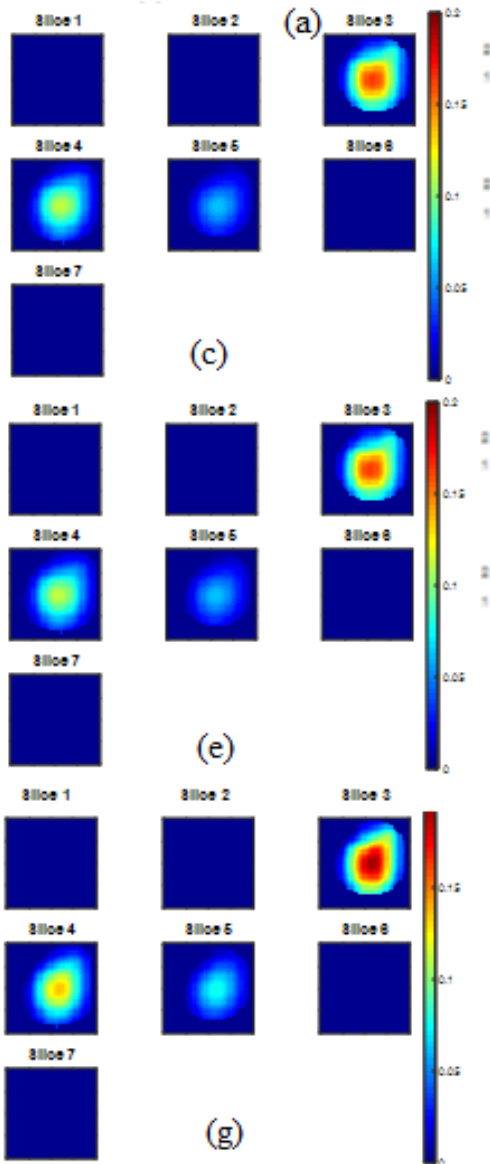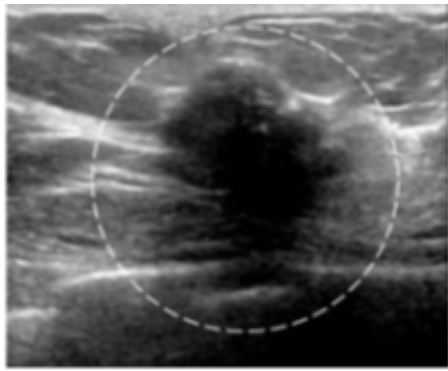
Figure 2.2: Reconstructed absorption map at 780 nm of a malignant case. (a) co-registered US image, (b) PINV initial image, Max μ_a=0.194 cm^{-1} (c) Newton with zero initial, Max μ_a=0.179 cm^{-1} (d) Newton with PINV initial, Max μ_a=0.268 cm^{-1} (e) regularized CG with zero initial, Max μ_a=0.179 cm^{-1} (f) regularized CG with PINV initial, Max μ_a=0.267 cm^{-1} and (g) unregularized CG, Max μ_a=0.216 cm$^{-1.}$

An example of a benign lesion is shown in Figure 2.3. Figure 2.3 (a) is the co-registered US image with the suspicious lesion marked by a circle. Absorption map of MPP estimated image is shown in Figure 2.3 (b), reconstructed images using five corresponding reconstruction methods are given in Figure 2.3 (c)-(g) and reconstructed maximum μ_a are quite similar. Box plot of maximum total hemoglobin (tHb) of all clinical cases is shown in Figure 2.4. The two-sample t test was performed between malignant and benign groups of each method. Newton's method and CG with PINV as an initial provide highest statistical significance.

(a)

(b)

(c)

(d)

(e)

(f)

(g)
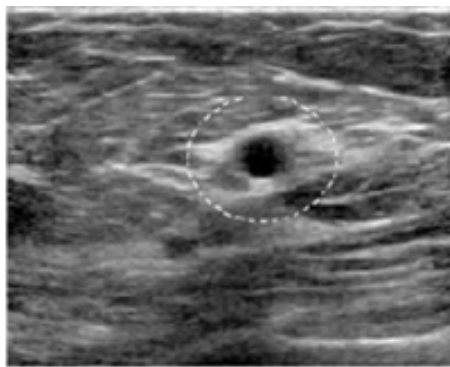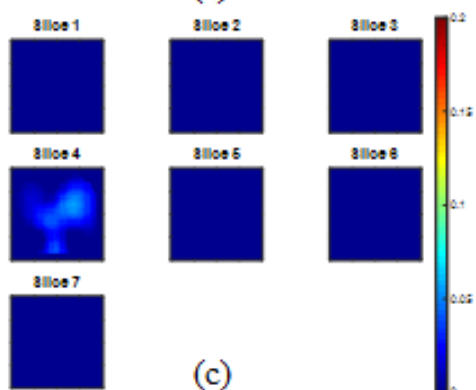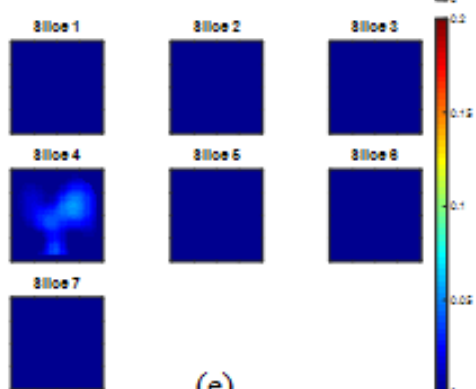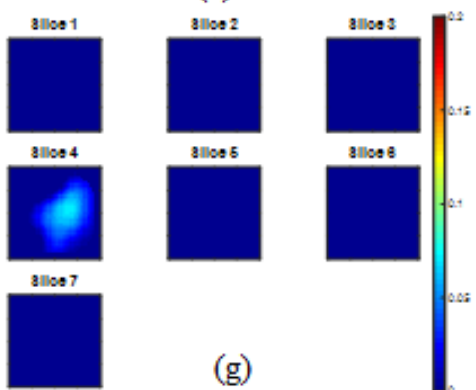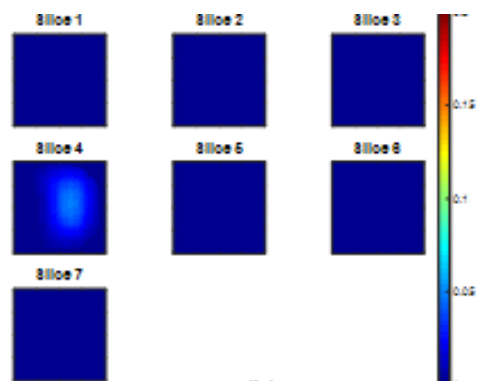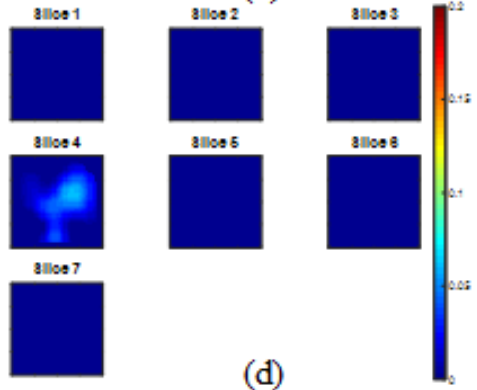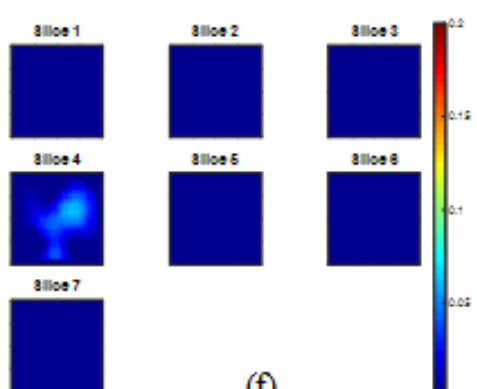
Fig. 2.3: Reconstructed absorption map at 780 nm of a benign case. (a) co-registered US image, (b) PINV reference image, Max μ_a=0.076 cm^{-1} (c) Newton with zero initial, Max μ_a=0.078 cm^{-1} (d) Newton with PINV initial, Max μ_a=0.087 cm^{-1} (e) regularized CG with zero initial, Max μ_a=0.077 cm^{-1} (f) regularized CG with PINV initial, Max μ_a=0.088 cm^{-1} and (g) unregularized CG, Max μ_a=0.092 cm^{-1}. The absorption maps have the same scale as Fig.2.

Additionally, the malignant to benign contrast ratios are 1.61, 2.11, 1.61, 2.07, 1.93, for Newton's with zero initial, PINV initial, CG zero initial, PINV initial and unregularized CG respectively. The average and standard deviation of maximum tHb concentration obtained from each method is given in Table 2.4. For benign cases, reconstructed tHb are comparable using five methods, however, for malignant cases the total Hb contrast is much higher when Newton's and CG are used with PINV initial estimate.

Table 2.4: Total Hb concentration (μM) for clinical cases using different methods

	Newton with zero Ini	Newton with PINV ini	CG with zero ini	CG with PINV ini	CG unregularized
Total Hb conc. (Benign)	47.5±14.2	49.4±10.6	47.5±14.3	50.4±9.8	48.5±16.3
Total Hb conc. (Malignant)	76.4±23.9	104.2±23.6	76.5±23.8	104.2±23.6	93.5±26.9
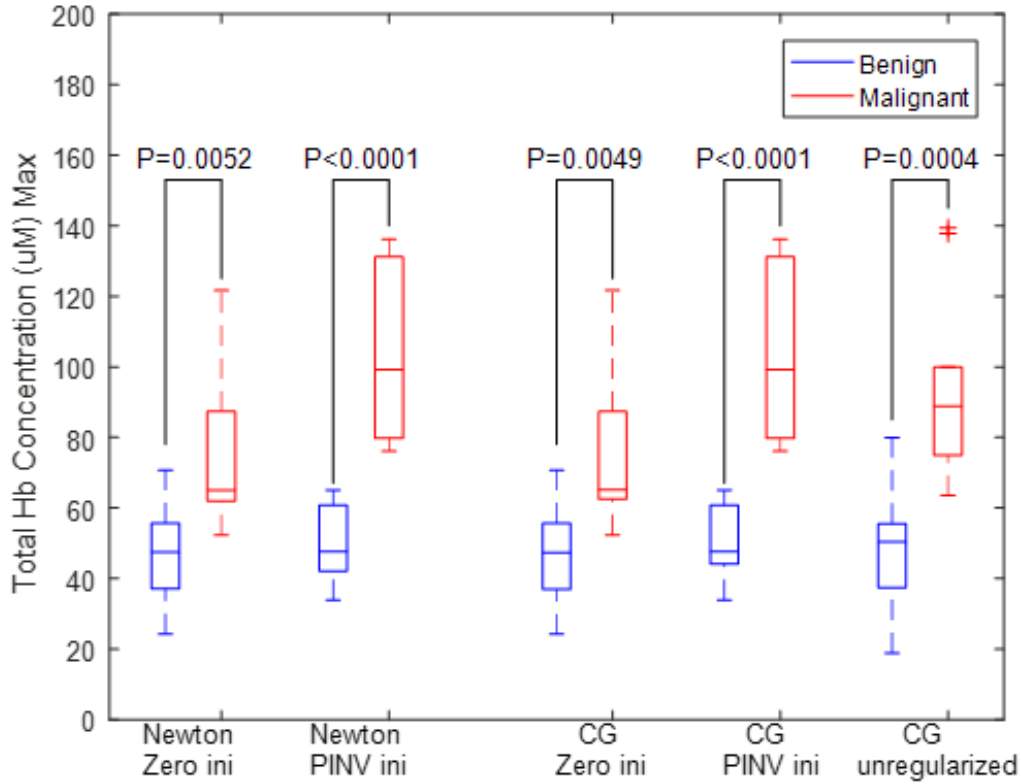
Figure 2.4: Box plot of total hemoglobin concentration of 20 patients (malignant (red), n=10, benign (blue) n=10) using five methods. PINV as an initial guess and Newton as optimization (first and second columns), zero and PINV as initial guess and CG (third the fourth columns), and unregularized CG (last column).

We also calculated the detectabilty, SNR_t for comparing all the five methods using the following formula, [24],

$$SNR_t = \frac{\langle t \rangle_1 - \langle t \rangle_2}{\sqrt{\frac{1}{2}\sigma_1^2 + \frac{1}{2}\sigma_2^2}}$$

Eq. (2.12)

Where, $\langle t \rangle_1$ and $\langle t \rangle_2$ are mean tHb for malignant and bening group respectively, and σ_1^2 and σ_2^2 are variance of malignant and benign group respectively.

From the detectability, AUC was calculated using equation (6) in ref 25. The result is shown in table 2.5. For 20 samples studied in this project, we obatained an AUC of 0.8498 for newton with zero initial, 0.9829 for newton with PINV initial, 0.8591 for CG with zero initial, 0.9824 for CG with PINV initial and 0.9238 for unregularized CG. The detectability values are 1.4646 for newton with zero initial, 2.9939 for newton with PINV initial, 1.4773 for CG with zero initial, 2.9790 for CG with PINV initial and 2.0234 for unregularized CG. Both the AUCs and detectabilty values show similar trend as p-values calculated earlier: PINV initial is better than zero initial, and unregularized CG performs better than zero initial but worse than PINV initial.

Table 2.5: Detectability and AUC values for clinical cases using different methods

	Newton with zero Ini	Newton with PINV ini	CG with zero ini	CG with PINV ini	CG unregularized
Detectability	1.4646	2.9939	1.4773	2.9790	2.0234
AUC	0.8498	0.9829	0.8591	0.9824	0.9238

2.3.3 Convergence Analysis

Utilizing PINV as an initial estimate of lesion optical properties, Newton and CG have demonstrated better classification of benign and malignant tumors because of improved convergence rate and solution stability. To compare the convergence of different reconstruction methods, we normalize the objective function for each method to the power of scattered field, $\|U_{sc}\|^2$, which is the initial objective function for unconstrained CG method. Shown in Fig. 2.5 is the mean and standard deviation of normalized object functions of five methods using phantom data. Truncated pseudoinverse provides a good initial guess which reduces the initial objective function to 4%. Newton and CG with PINV as an initial estimate converge in 1 and 2 iterations, respectively. Newton and CG with zero initial converges in 1 and 3 iterations, respectively, and

the residual normalized objective function of CG is slightly higher than that with PINV as an initial. Unconstrained CG converges in 3 ietrations. Note that for our early studies using unconstrained CG, the iteration was stopped at 3 ietrations because it provided optimal performance for phantom data.

Figure 2.6 shows normalized object functions of a typical malignant and a typical benign case. Interestingly, the convergenece tread follows phantom data well. After 3 or 4 iterations unconstrained CG method has a larger residual than other four methods . With PINV as an initial estimate, Newton converges in one iteration and CG two iterations. If zero initial is used, Newton converge quickly about two iterations, while CG converges in 4 to 5 iterations. Table 2.6 and 2.7 show mean and standard deviations of normalized objective functions for five methods up to 5 iterations. Newton with PINV as an initial is the best and convergeres in one iteration with the lowest residual normalized objective function and standard deviation. The unconstrained CG has the largest residual and standard deviation and may not converge after 4 iterations.

For unconstrained CG method, reduction of object function doesn't always guarantee better reconstructed image quality. Because of the ill-conditioned and underdetermined DOT reconstruction problem, there are many local minima of object function for unconstrained formulation. Regularization parameter balances data fidelity and penalty term. Pseudoinverse is dominated by first few singular values which are significantly larger than other singular values. These large singular value components are less affected by noise. Initial estimate from only first few singular values are hence reliable and can help Newton and CG search algorithms converge quickly. Additionally, applying a regularization factor obtained from the first singular value and target size is more individualized to the weight matrix and help stabilize the reconstruction.

44
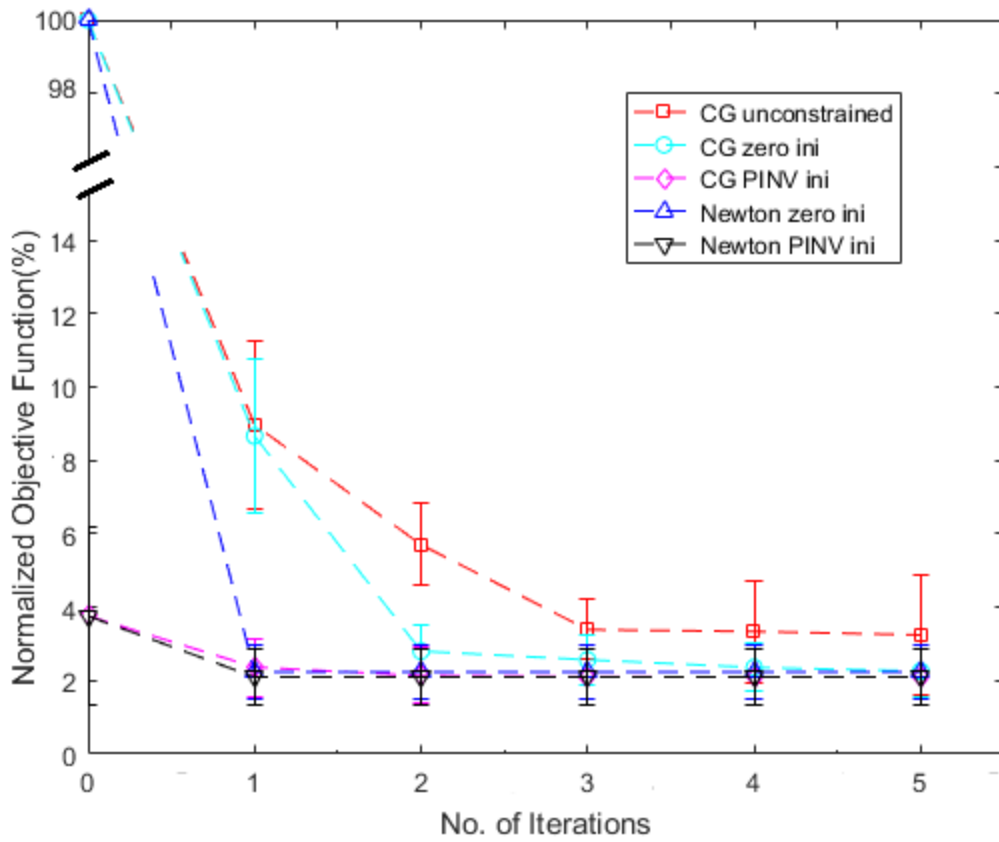
Figure 2.5: Normalized object functions of five different methods using phantoms data.
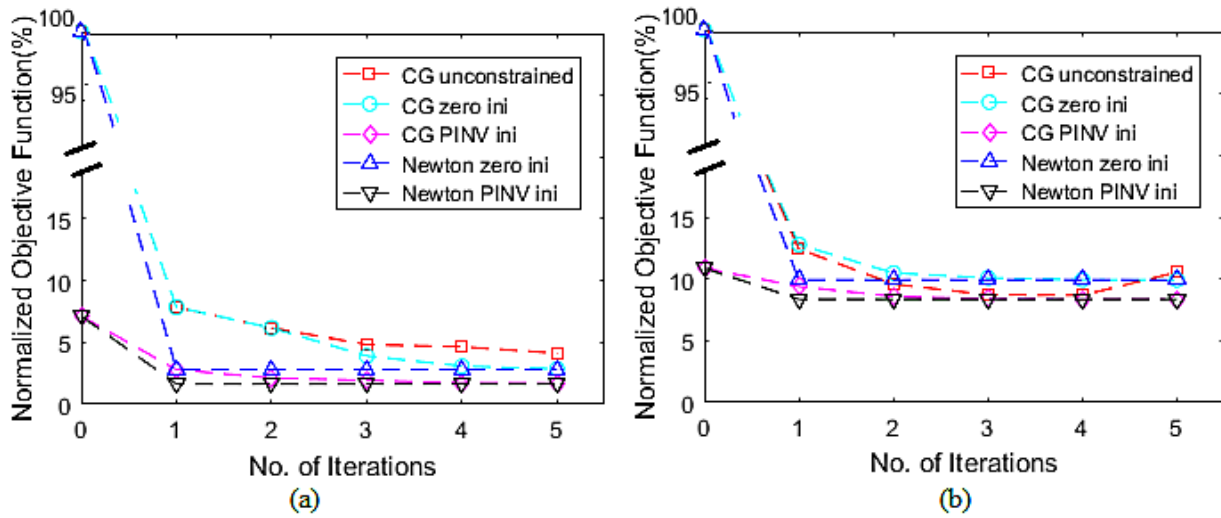
Figure 2.6:   Normalized object functions of five different methods of (a) a malignant lesion and

(b) a benign lesion.

Table 2.6: Normalized objective function (mean ± standard deviation) for malignant cases

	Iteration 1	Iteration 2	Iteration 3	Iteration 4	Iteration 5
Newton with zero Ini	10.0%± 5.6	10.0%± 5.6	10.0% ± 5.6	10.0% ± 5.6	10.0%± 5.6
CG with zero ini	22.5%± 8.7	16.4% ± 6.8	12.6 %± 5.6	11.0%± 5.5	10.2% ± 5.5
Newton with PINV ini	7.8% ± 4.9	7.8% ± 4.9	7.8% ± 4.9	7.8%± 4.9	7.8%± 4.9
CG with PINV ini	10.2 %± 5.5	9.2%± 5.3	8.6 %± 4.9	8.1%± 4.9	7.9%± 4.9
unconstrained CG	22.5% ± 8.7	17.1%± 7.0	15.6% ± 7.1	18.1% ± 10.2	29.2% ± 29.6

Table 2.7: Normalized objective function (mean ± standard deviation) for benign cases

	Iteration 1	Iteration 2	Iteration 3	Iteration 4	Iteration 5
Newton with zero Ini	22.8 ± 18.2	22.8 ± 18.2	22.8 ± 18.2	22.8 ± 18.2	22.8 ± 18.2
CG with zero ini	35.1 ± 24.3	25.9 ± 20.3	23.6 ± 18.4	22.9 ± 18.3	22.8 ± 18.2
Newton with PINV ini	18.7 ± 15.6	18.7 ± 15.6	18.7 ± 15.6	18.7 ± 15.6	18.7 ± 15.6
CG with PINV ini	21.2 ± 16.6	19.7 ± 16.3	18.9 ± 15.7	18.7 ± 15.6	18.7 ± 15.6
CG unconstrained	38.6 ± 32.5	32.3 ± 34.1	30.7 ± 34.6	31.1 ± 34.7	33.2 ± 34.8

2.3.4 Target Centroid Error Analysis

To compare different reconstruction methods, the target centroid error i.e. the absolute difference

between the center of a phantom target measured by co-registered US and the centroid of

46

corresponding reconstructed target absorption map, is calculated as a measure of reconstruction quality. Phantom data of both low and high contrast targets of 1 cm diameter located at different depths and measured at 780 nm were used to estimate the centroid error and results are shown in Table 2.8. MATLAB function 'regionprop' is used to estimate the centroid of target absorption map and the difference between the estimated centroid and the measured target center from corresponding co-registered US is calculated. As seen from Table 2.8, the target centroid error which is less than one voxel size of 0.25 cm does not depend on reconstruction method. Thus, all reconstruction methods provide the same target centroid.

Table 2.8: Object centroid error $(\Delta x, \Delta y)$ (mean $\pm$ standard deviation) for phantom data

	Newton with zero ini	Newton with PINV ini	CG with zero ini	CG with PINV ini	CG unregularized
Object centroid Error (Δx)	0.157±0.093	0.157±0.093	0.157±0.093	0.157±0.093	0.163±0.091
Object centroid Error (Δy)	0.225±0.101	0.225±0.101	0.225±0.101	0.225±0.101	0.190±0.069

2.4 Summary and Discussion

Choice of regularization parameter, λ, is an important part of reconstruction. If λ is too small, then the penalty may not have any effect on reconstruction, however, a larger λ heavily penalizes data fidelity term and solution may not converge near true minimum of unregularized objective function. In our approach, λ is chosen as $\boldsymbol{\lambda} = \boldsymbol{p}\sqrt{\boldsymbol{\sigma_1}}$ which decreases with $\boldsymbol{\mu_{s0}}'$ and increases with background $\boldsymbol{\mu_{a0}}$. Thus, for higher background $\boldsymbol{\mu_{a0}}$, the λ regulates more to improve the conditioning of the Q matrix. Additionally, because the huge difference between the first and the rest of the eigenvalues, the $\boldsymbol{\lambda}/\boldsymbol{\sigma_n}$ increases with n and therefore λ regulates more for smaller eigenvalues and further improves the conditioning of Q matrix. Choice of regularization parameter is always a difficult problem and mathematical techniques like L-curve and U-curve are not often useful [26-27]. We have determined regularization parameter by trial and error using phantom data to ensure convergence, reconstruction accuracy and lower image artifacts. In further study, we will apply machine learning techniques to automatically select regularization parameter to minimize the reconstruction error. The ultimate clinical use of ultrasound-guided diffused light imaging is to maximize the separation of benign and malignant lesions.

In the past two decades, researchers in DOT community have tried to simultaneously reconstruct target absorption coefficient, μ_a, and diffusion coefficient, D ($D = 1/3\mu_s'$, see Eq. (2.1)). However, since the lesion diffusion coefficient is much smaller than the absorption coefficient, correctly reconstructing the scattering coefficient is a challenge. Also, simultaneously reconstructing the absorption and diffusion coefficients doubles the number of unknown optical parameters to estimate. Therefore, the reconstruction becomes more ill-posed and under-determined. However, with a better initial estimate and an appropriate choice of regularization parameter λ, it is possible to explore simultaneous reconstruction of both parameters. This has

been demonstrated in reference 14 using GA as an initial estimate and unregulated CG to iteratively reconstruct target absorption and scattering maps. In this manuscript, our objectives were to 1) evaluate the performance of the proposed simple, robust, two-step reconstruction algorithm; and 2) compare this algorithm with a group of four algorithms including the unregulated CG algorithm that we have used in the past. Therefore, we did not attempt to simultaneously reconstruct both parameters but focused on absorption coefficient, μ_a, which is the most important parameter to reveal tumor angiogenesis. Thus, our phantoms have similar reduced scattering coefficient as the background medium. In future study, we will evaluate the performance of the proposed novel algorithm in simultaneously recovering both target absorption and scattering maps.

In summary, a simple, robust, two-step reconstruction algorithm has proposed, and its performance has demonstrated using phantom and clinical data. Using a truncated pseudoinverse as a preliminary estimate of target optical properties and regularized Newton and CG optimization search methods to iteratively reconstruct target optical properties within region of interest identified by co-registered US gave best results. The truncated pseudoinverse as a preliminary estimate and regularized Newton optimization converges in one iteration. This two-step reconstruction technique is generally applicable to x-ray-guided and MRI guided DOT imaging reconstruction.

References

1. Intes, X., Ntziachristos, V., Culver, J. P., Yodh, A., and Chance, B. "Projection access order in algebraic reconstruction technique for diffuse optical tomography," Physics in medicine and biology, 47(1), N1 (2001).

2. Arridge, S. R., and Schweiger, M. "A gradient-based optimisation scheme for optical tomography," Optics Express, 2(6), 213-226 (1998).

3. Hielscher, A. H., and Bartel, S. "Use of penalty terms in gradient-based iterative reconstruction schemes for optical tomography," Journal of Biomedical Optics, 6(2), 183-192 (2001).

4. Hielscher, A. H., Klose, A. D., and Hanson, K. M. "Gradient-based iterative image reconstruction scheme for time-resolved optical tomography," IEEE Transactions on medical imaging, 18(3), 262-271 (1999).

5. Dehghani, H., Srinivasan, S., Pogue, B. W., and Gibson, A. "Numerical modelling and image reconstruction in diffuse optical tomography," Philosophical Transactions of the Royal Society of London A: Mathematical, Physical and Engineering Sciences, 367(1900), 3073-3093 (2009).

6. Schweiger, M., Arridge, S. R., and Nissilä, I. "Gauss–Newton method for image reconstruction in diffuse optical tomography," Physics in medicine and biology, 50(10), 2365 (2005).

7. Brooksby, B., Jiang, S., Dehghani, H., Pogue, B. W., Paulsen, K. D., Weaver, J., and Poplack, S. P. "Combining near-infrared tomography and magnetic resonance imaging to study in vivo breast tissue: implementation of a Laplacian-type regularization to incorporate magnetic resonance structure," Journal of biomedical optics, 10(5), 051504-051504 (2005).

8. Azar, F. S., Lee, K., Khamene, A., Choe, R., Corlu, A., Konecky, S. D., and Yodh, A. G. "Standardized platform for coregistration of nonconcurrent diffuse optical and magnetic

resonance breast images obtained in different geometries," Journal of biomedical optics, 12(5), 051902-051902 (2007).

9. Zhang, L., Zhao, Y., Jiang, S., Pogue, B. W., and Paulsen, K. D. "Direct regularization from co-registered anatomical images for MRI-guided near-infrared spectral tomographic image reconstruction," Biomedical optics express, 6(9), 3618-3630 (2015).

10. Fang, Q., Selb, J., Carp, S. A., Boverman, G., Miller, E. L., Brooks, D. H., and Boas, D. A. "Combined optical and X-ray tomosynthesis breast imaging," Radiology, 258(1), 89-97 (2011).

11. Krishnaswamy, V., Michaelsen, K. E., Pogue, B. W., Poplack, S. P., Shaw, I., Defrietas, K., and Paulsen, K. D. "A digital x-ray tomosynthesis coupled near infrared spectral tomography system for dual-modality breast imaging," Optics express, 20(17), 19125-19136 (2012).

12. Zhu, Q., Ricci Jr, A., Hegde, P., Kane, M., Cronin, E., Merkulov, A., and Tannenbaum, S. "Assessment of functional differences in malignant and benign breast lesions and improvement of diagnostic accuracy by using US-guided diffuse optical tomography in conjunction with conventional US," Radiology, 280(2), 387-397 (2016).

13. Uddin, KM Shihab, Atahar Mostafa, Mark Anastasio, and Quing Zhu. "Two step imaging reconstruction using truncated pseudoinverse as a preliminary estimate in ultrasound guided diffuse optical tomography." Biomedical optics express 8, no. 12 (2017): 5437-5449.

14. Tavakoli, B., and Zhu, Q. "Two-step reconstruction method using global optimization and conjugate gradient for ultrasound-guided diffuse optical tomography," Journal of biomedical optics, 18(1), 016006-016006 (2013).

15. Klose, Alexander D., and Edward W. Larsen. "Light transport in biological tissue based on the simplified spherical harmonics equations." Journal of Computational Physics 220, no. 1 (2006): 441-470.

16. Jha, Abhinav K., Matthew A. Kupinski, Takahiro Masumura, Eric Clarkson, Alexey V. Maslov, and Harrison H. Barrett. "Simulating photon-transport in uniform media using the radiative transport equation: a study using the Neumann-series approach." JOSA A 29, no. 8 (2012): 1741-1757.

17. Jha, Abhinav K. "Retrieving information from scattered photons in medical imaging." (2013).

18. J. B. Fishkin and E. Gratton, "Propagation of photon-density waves in strongly scattering media containing an absorbing semi-infinite plane bounded by a straight edge," J. Opt. Soc. Am. A 10(1), 127–140 (1993).

19. Zhu, Q., Chen, N., and Kurtzman, S. H. "Imaging tumor angiogenesis by use of combined near-infrared diffusive light and ultrasound," Optics letters, 28(5), 337-339 (2003).

20. Zhu, Yansong, Abhinav K. Jha, Dean F. Wong, and Arman Rahmim. "Image reconstruction in fluorescence molecular tomography with sparsity-initialized maximum-likelihood expectation maximization." Biomedical optics express 9, no. 7 (2018): 3106-3121.

21. Jha, Abhinav K., Harrison H. Barrett, Eric C. Frey, Eric Clarkson, Luca Caucci, and Matthew A. Kupinski. "Singular value decomposition for photon-processing nuclear imaging systems and applications for reconstruction and computing null functions." Physics in Medicine & Biology 60, no. 18 (2015): 7359.

22. Modgil, Dimple, Patrick J. La Rivière, and Bradley E. Treeby. "Photoacoustic image reconstruction in an attenuating medium using singular-value decomposition." Journal of biomedical optics 17, no. 6 (2012): 061204.

23. Press, W. H. Numerical recipes 3rd edition: The art of scientific computing (Cambridge university press, 2007).

24. Barrett, Harrison H., and Kyle J. Myers. Foundations of image science. John Wiley & Sons, Chapter 13, 2013.

25. Jha, Abhinav K., Eric Clarkson, and Matthew A. Kupinski. "An ideal-observer framework to investigate signal detectability in diffuse optical imaging." Biomedical optics express 4, no. 10 (2013): 2107-2123.

26. Hanke, Martin. "Limitations of the L-curve method in ill-posed problems." BIT Numerical Mathematics 36, no. 2 (1996): 287-301.

27. Hansen, Per Christian. "The L-curve and its use in the numerical treatment of inverse problems." (1999): 119-142.

Chapter 3: Imaging artifact reduction by perturbation outlier removal

3.1 Introduction

DOT reconstructed images can be distorted by image artifacts due to outlier measurements. due to wavelength-dependent tissue heterogeneity, bad coupling between tissue and sources and detectors, and patient motion or operator hand motion. Several experimental and modeling approaches have been developed for system calibration of optical source strengths, detection channel gains and phase shifts [1-3], source and detector (optodes) position errors, and coupling errors between skin and optodes [4-8]. For correcting motion artifacts, different algorithms have been proposed, including cubic spline interpolation [9], adaptive Kalman filtering [10], and wavelet-based motion artifact removal [11]. To improve the imaging quality, projection error based adaptive regularization techniques have been employed which outperform standard Tikhonov regularization [12]. However, these approaches do not compensate for wavelength-dependent problems. For example, the 740 nm wavelength is prone to measurement errors from tissue heterogeneity caused by dark skin and skin pigment. As another example, the 830 nm wavelength has lower SNR at longer source and detector distances due to the reduced sensitivity of photomultiplier tube detector beyond 800 nm.

In our US-guided DOT approach to assessing breast cancer, perturbation, which is the normalized difference between the lesion breast and the contralateral normal breast (reference) measurements, is used for mapping lesion absorption at each wavelength. The total hemoglobin map is computed

from the absorption maps of four optical wavelengths. The tissue heterogeneity of the reference measurements contributes to outliers in the perturbation measurements. In a recent investigation by our group, Vavadi et al. [13] introduced a statistical method based on the semi-infinite tissue model to automatically remove outliers from contralateral normal breast measurements. However, this method cannot be used for perturbation measurements because lesion measurements are expected to be more heterogeneous than the reference measurements. To separate the measurement errors from lesion heterogeneity, more information from multiple wavelength measurements can be incorporated in the preprocessing before image reconstruction. Recently, Murad et al. introduced an approach for data filtering based on multiple wavelength measurements collected at the lesion site [14]. The method combines data collected from multiple sets of lesion measurements to detect and correct outliers caused by wavelength- dependent measurement errors in the perturbation. However, this approach requires that 2-3 wavelength perturbation datasets must be correlated, and then the rest of the wavelength-dependent distortion can be compensated for.

In this chapter, we propose a new iterative perturbation correction algorithm by using structural similarity index (SSIM) as an image quality assessment criterion. The initial estimate of the absorption map is obtained from the truncated pseudoinverse solution. In subsequent iterations, the average SSIM for each wavelength and errors between the measurement and the projected data are computed and outliers are removed from the measurements based on the errors. This procedure is iterated until the SSIM reaches a preset threshold. We demonstrate the effectiveness of this approach in phantoms and clinical data. The methods and results of this chapter is partially adopted from my published article in Journal of biomedical optics [15].

3.2 Materials and methods

3.2.1 DOT Data preprocessing

DOT data acquisition is performed on both a lesion breast and a contralateral normal breast, referred as the reference breast. Amplitude and phase measurements are extracted from the detected RF signal using the Hilbert transform. For the ith source-detector pair, reference measurement is given as $U_r(i) = A_r(i)e^{j\varphi_r(i)}$, and the lesion measurement is $U_l(i) = A_l(i)e^{j\varphi_l(i)}$, where $i = 1,2, \dots m$, and m is the total number of source-detector pairs or the total number of measurements. Perturbation, $U_{sc}(i)$, is defined as the normalized difference between the reference and target measurements.

$$U_{sc}(i) = \frac{A_l(i)e^{j\varphi_l(i)} - A_r(i)e^{j\varphi_r(i)}}{A_r(i)e^{j\varphi_r(i)}}$$

$$= \left(\frac{A_l(i)}{A_r(i)}\cos(\varphi_l(i) - \varphi_r(i)) - 1\right) + j\left(\frac{A_l(i)}{A_r(i)}\sin(\varphi_l(i) - \varphi_r(i))\right). \qquad \text{Eq (3.1)}$$

The first term is the real part of the perturbation, and the second term is the imaginary part of the perturbation. A typical 2D representation of perturbation data for a phantom is shown in Figure 3.1, with real perturbation on the x-axis and imaginary perturbation along the y-axis. The unit circle represents the expected boundary that perturbation data should lie within. From simulations of different target contrasts and locations in depths, it was shown that maximum phase difference for any source detector pair should not exceed 90 degrees, even in extreme cases [13]. Since $0 \leq \cos(\varphi_l(i) - \varphi_r(i)) \leq 1$ for $-\frac{\pi}{2} \leq \varphi_l(i) - \varphi_r(i) \leq \frac{\pi}{2}$ for all i, real perturbation should be greater than -1. For a high contrast target, $A_l \ll A_r$, so perturbation is more skewed towards the negative real axis. For a low contrast target, perturbation is very small and clustered more towards the

positive real axis, while imaginary perturbation is evenly distributed around the origin, since $-1 \le$

$\sin(\varphi_l(i) - \varphi_r(i)) \le 1$ for $-\frac{\pi}{2} \le \varphi_l(i) - \varphi_r(i) \le \frac{\pi}{2}$.
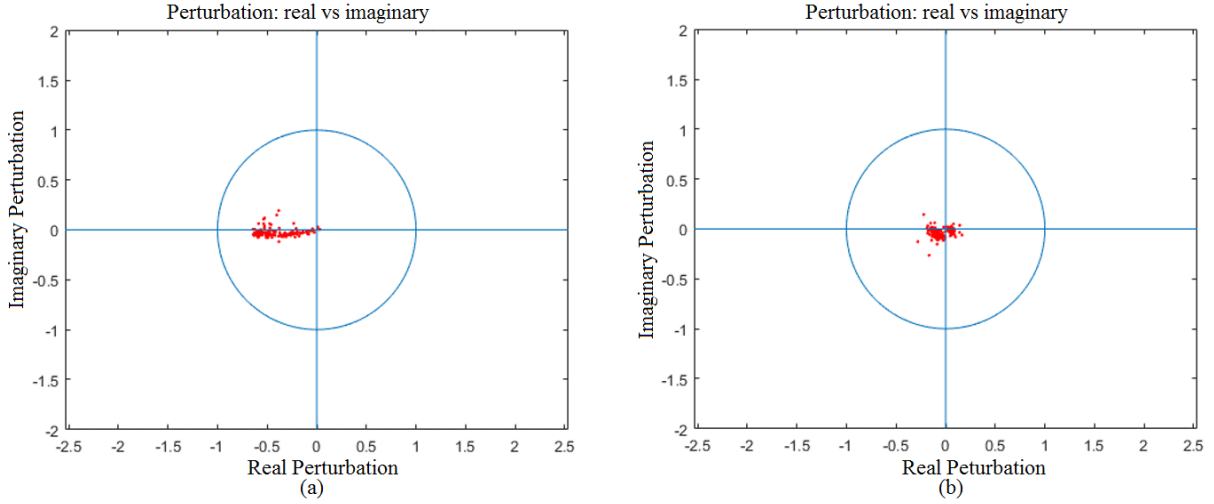
Figure 3.1: Phantom perturbation data. (a) Data measured from a high contrast phantom target imbedded in intralipid solution. (b) Data measured from a low contrast phantom target imbedded in intralipid solution.

Figure 3.2 shows one set of perturbation data of a highly absorbing malignant breast lesion and a low absorbing benign breast lesion . As evident from the figure, clinical data is more scattered because of tissue heterogeneity, mis-coupling of the tissue and source and detector fibers, and patient movement or operator hand motions.
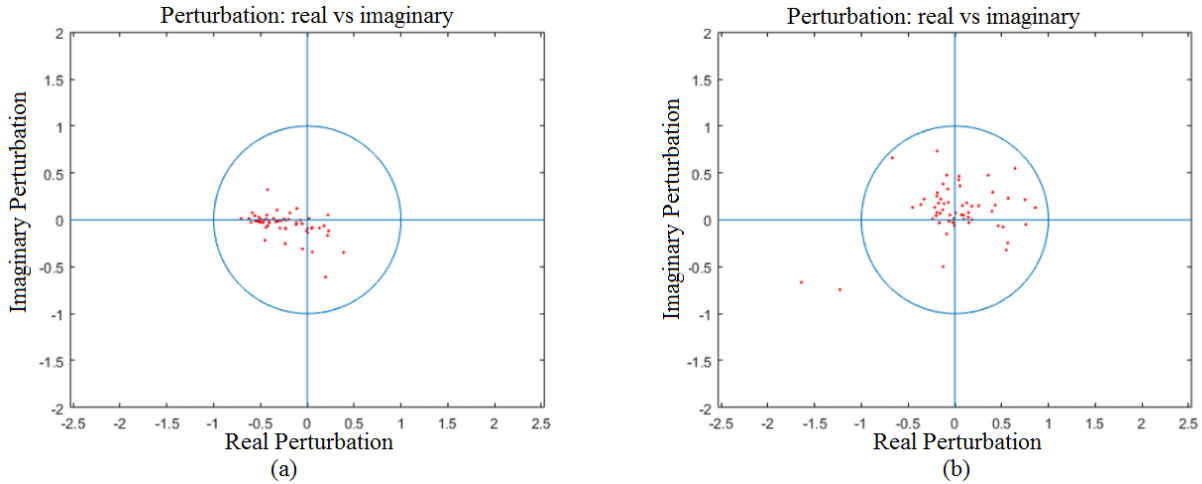
Figure 3.2: Clinical perturbation data. (a) A malignant breast lesion. (b) A benign breast lesion.

Multiple perturbation datasets are compiled together, and a multivariate Gaussian is fitted, and data points are removed if there are any with a Mahalanobis distance greater than the threshold computed from the inverse chi-square distribution with a cumulative probability of 99%. Based on chest wall matching of the reference and lesion breast, a single measurement dataset is selected from multiple measurements. The structural similarity-based perturbation correction algorithm depicted in Figure 3.3 is applied to perturbation data to obtain corrected perturbation and artifact-free images.

3.2.2 Image Quality Assessment

In DOT reconstruction, quantitative assessment of imaging quality poses a challenge. Previously, image distortion and inconsistent images for different wavelengths were visually inspected, and perturbation was manually corrected by an experienced operator. Such manual data processing is operator-dependent and time consuming. In this manuscript, we propose to use the structural

similarity index (SSIM) to quantitatively evaluate imaging quality by taking all four wavelength images into account. The SSIM measure is a function of the image's luminance, contrast, and structure [16-17]. The SSIM between two images X and Y is defined as in Ref. 16,

$$SSIM(X,Y) = [l(X,Y)]^\alpha \cdot [c(X,Y)]^\beta \cdot [s(X,Y)]^\gamma \qquad \text{Eq. (3.2)}$$

where $l(X,Y)$, $c(X,Y)$ and $s(X,Y)$ are the luminance, contrast and structure similarity respectively, and $\alpha > 0, \beta > 0, \gamma > 0$ are three parameters used to adjust relative importance of the three components of similarity measure. The luminance, contrast, and structure of an image are computed from mean, standard deviation and normalized images [17] as

$$l(X,Y) = (2\mu_X\mu_Y + C_1)/(\mu_X^2 + \mu_Y^2 + C_1)$$

$$c(X,Y) = (2\sigma_X\sigma_Y + C_2)/(\sigma_X^2 + \sigma_Y^2 + C_2)$$

$$s(X,Y) = (\sigma_{XY} + C_3)/(\sigma_X\sigma_Y + C_3) \qquad \text{Eq. (3.3)}$$

Here, $\mu_X, \mu_Y, \sigma_X, \sigma_Y$, and σ_{XY} are the means of pixel values of image X and image Y, the standard deviation of image X and image Y, and the covariance of image X and Y, respectively. C_1, C_2, C_3 are constants.

For each wavelength, $\lambda_i \in \{740,780,808,830 \ nm\}$, the other three wavelength images are used as references to compute SSIMs for three image pairs. An average of the three SSIMs is the quantitative image quality index, $SSIM(\lambda_i)$, used to evaluate the reconstructed image quality of wavelength λ_i as given below:

$$SSIM(\lambda_i) = \frac{1}{n_{wavelength}-1} \sum_{j=1,j\neq i}^{n_{wavelength}} SSIM(image_i, image_j). \qquad \text{Eq. (3.4)}$$

3.2.3 Iterative Perturbation Correction

Iterative perturbation correction is performed based on $SSIM(\lambda_i)$ for each wavelength. The wavelength with the minimum $SSIM(\lambda_i)$ is corrected first. The initial estimate is from the truncated pseudoinverse (PINV). If $SSIM(\lambda_i)$ is lower than a preset threshold (0.9), perturbation from λ_i wavelength is corrected based on the original perturbation and projected perturbation. The reconstructed image, $\delta\mu_a'$, for λ_i is projected into measurement space by multiplying the weight matrix, $\boldsymbol{W}$, to obtain projected data:

$$[U_{projected}] = [W][\delta\mu_a'] \qquad\qquad \text{Eq. (3.5)}$$

Based on the Euclidean distance of original perturbation data, U_{sc}, and projected data, $U_{projected}$, projection error, $E_{proj,}$ is calculated as

$$E_{proj} = \left\| U_{projected} - U_{sc} \right\|^2. \qquad\qquad \text{Eq. (3.6)}$$

The data point with maximum projection error is removed from U_{sc}. Modified perturbation is again used to reconstruct the absorption map for wavelength λ_i using regularized CG. $SSIM(\lambda_i)$ is recomputed and compared with the threshold. This process is repeated until the lowest $SSIM(\lambda_i)$ is greater or equal to the threshold. This iterative correction procedure is performed for each wavelength until the $SSIM(\lambda_i)$ values for all four wavelengths are above the threshold.
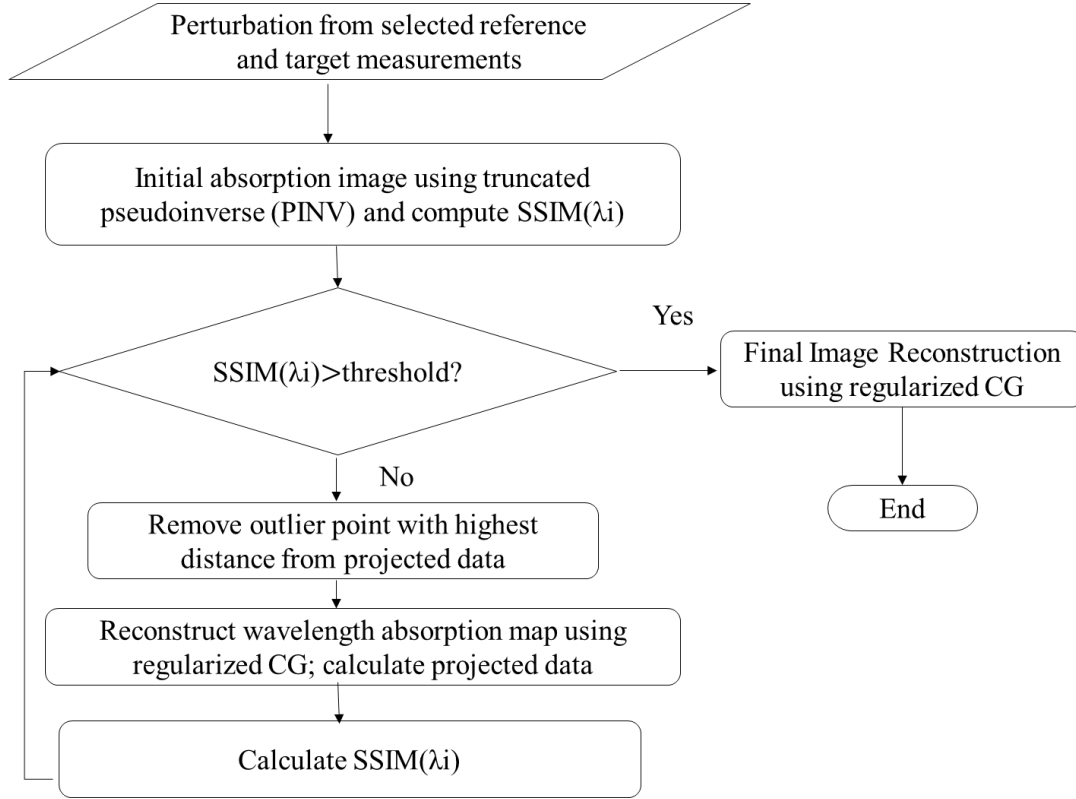
Figure 3.3: Data preprocessing and iterative perturbation correction algorithm

3.3 Results

3.3.1 Phantom experiment

In phantom experiments, intralipid solution was used to simulate a homogeneous background medium. The experiment was repeated for solid spherical balls with different contrasts and sizes simulating different types of tumors in intralipid solution in different depths. The average image similarity index was computed for all phantom absorption map images. The reconstructed absorption map for a ball of 2 cm diameter at 2 cm depth is shown in Figure 4. The average

structural similarity indices for four wavelengths —740 nm, 780 nm, 808 nm, and 830 nm—are 0.98, 0.97,0.99, and 0.96, respectively.
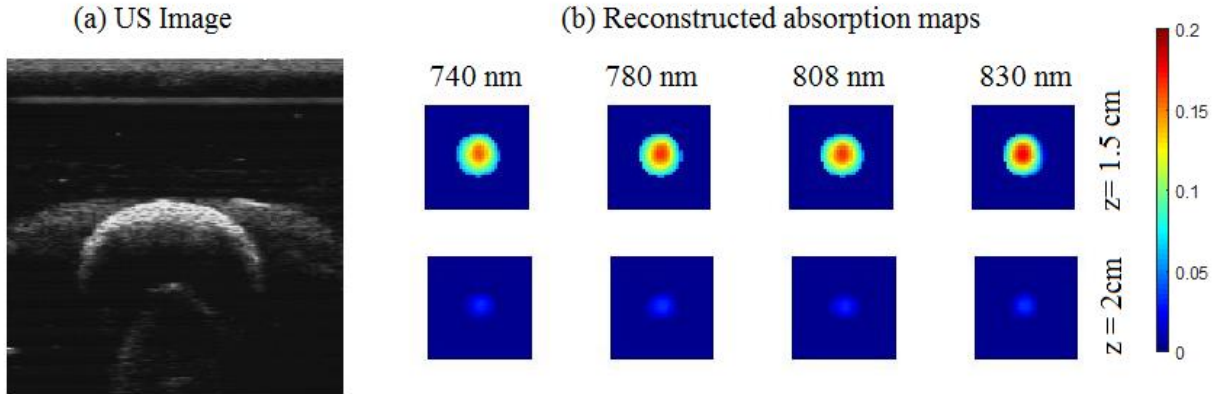
Figure 3.4: Reconstructed image similarity for phantom data (a) US image (b) reconstructed absorption maps (2 layers at $z = 1.5\ cm$ and $z = 2\ cm$) for all four wavelengths. Each 2D layer is $8\ cm\ \times 8\ cm$. Average SSIMs are 0.98, 0.97, 0.99, 0.96 for 740 nm,780 nm, 808 nm and 830 nm respectively.

Pairwise SSIMs (mean ± standard deviation) are presented in Table 1. Large similarity indices indicate strong structural similarity among different wavelengths, which is visually apparent in figure 3.4.

Table 3.1: Structural similarity index (mean ± standard deviation) for phantom data

	740 nm	780 nm	808 nm	830 nm
740 nm	—	0.976 ± 0.004	0.988 ± 0.003	0.942 ± 0.015
780 nm	0.976 ± 0.004	—	0.985 ± 0.006	0.943 ± 0.023

808 nm	0.988 ± 0.003	0.985 ± 0.006	—	0.947 ± 0.020
830 nm	0.942 ± 0.015	0.943 ± 0.023	0.947 ± 0.020	—
Average	0.954 ± 0.019	0.969 ± 0.008	0.957 ± 0.018	0.974 ± 0.009

3.3.2 Clinical study

A clinical study was approved by the local Institutional Review Board (IRB) and was compliant with the Health Insurance Portability and Accountability Act (HIPPA). Informed consent was given by each patient. Data used in this study have been de-identified. A total 40 patients were studied including 13 malignant and 27 benign lesions, based on biopsy results. All patients were categorized into two categories, patients with image artifact present in one or more wavelength absorption maps (17 patients) and patients with no image artifact (23 patients). This categorization was based on a present cutoff value of 0.9 for structural similarity among the four wavelengths reconstructed absorption map images. An example of benign fibroadenoma is shown in Figure 3.5. Figure 3.5(a) shows the ultrasound image with the lesion marked by a white ellipse. Figure 3.5(b) shows reconstructed absorption maps for four wavelengths. Each wavelength absorption map has one 2D layer at depth, $z = 1\ cm$. The mean SSIMs for the four wavelengths 740, 780, 808, and 830 nm are 0.87, 0.91, 0.87, and 0.82. The reconstructed absorption coefficients are 0.2463 cm^{-1}, 0.2069 cm^{-1}, 0.1326 cm^{-1} and 0.3316 cm^{-1}, respectively. Image SSIM indicates that there is image artifact at wavelength 830 nm and visual inspection confirms this. Figure 3.5(c) shows reconstructed absorption maps after perturbation correction. The mean SSIMs for the four wavelengths changes to 0.95, 0.97, 0.97, and 0.96 while absorption coefficients change to 0.1582 cm^{-1}, 0.1470 cm^{-1}, 0.1345 cm^{-1}, and 0.1484 cm^{-1} respectively.

Figure 3.5: Image artifact reduction for a benign case (a) US image, 1 cm lesion depth (b) absorption maps for original data before perturbation correction (c) absorption maps after perturbation correction

Iterative changes in the perturbation and absorption map for this case at 830 nm are shown in Figure 3.6. For iteration 0, we see the original dataset and the absorption map: the map is similar to that in Figure 3.5(b). In successive iterations we removed perturbation points denoted by red dots. We continue to remove perturbations until absorption map is structurally similar to the maps of other wavelengths.
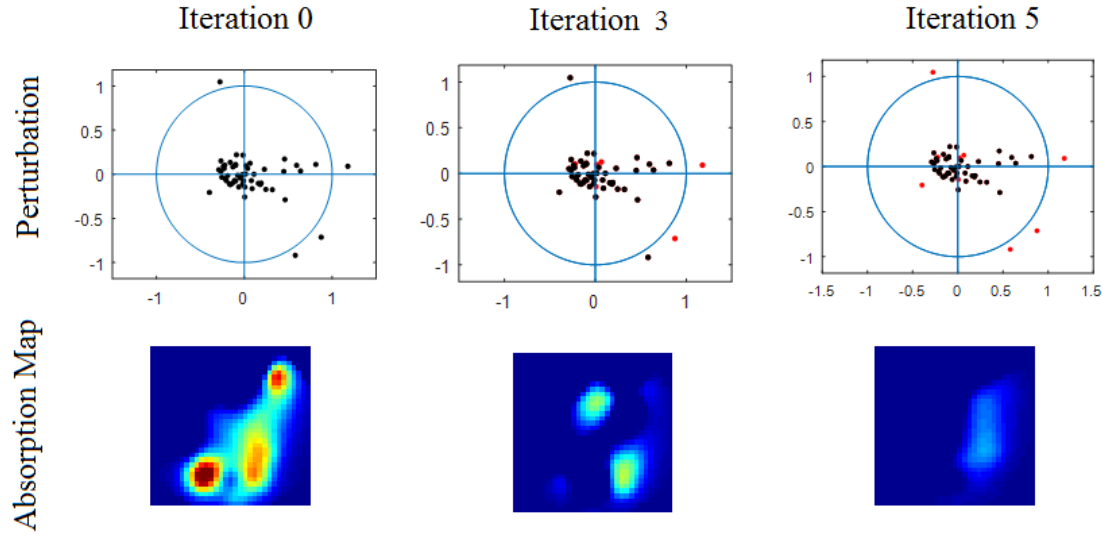
Figure 3.6: Iterative changes in absorption map and perturbation filtering for 830 nm for the benign case. Red dots denote removed data points.

An example of malignant breast cancer with mixed ductal and lobular features is shown in Figure 3.7. Figure 3.7(a) shows an ultrasound image with a lesion marked by a white ellipse. Figure 3.7(b) shows reconstructed absorption maps for the four wavelengths. Each wavelength absorption map shows two layers at depths, $z = 1.5 \ and \ 2 \ cm$. Mean image similarity indices for the four wavelengths 740, 780, 808, and 830 nm are 0.83, 0.82, 0.77, and 0.79, and reconstructed absorption coefficients are 0.254 cm^{-1}, 0.237 cm^{-1}, 0.070 cm^{-1}, and 0.054 cm^{-1}, respectively. Image artifact is present in 808 and 830 nm absorption maps. Figure 3.7(c) shows reconstructed absorption maps after perturbation correction. Mean SSIMs for four wavelengths improves to 0.94, 0.94, 0.93, and 0.91 while reconstructed absorption coefficients changed to 0.2542 cm^{-1}, 0.2371 cm^{-1}, 0.2281 cm^{-1}, and 0.1754 cm^{-1}, respectively.
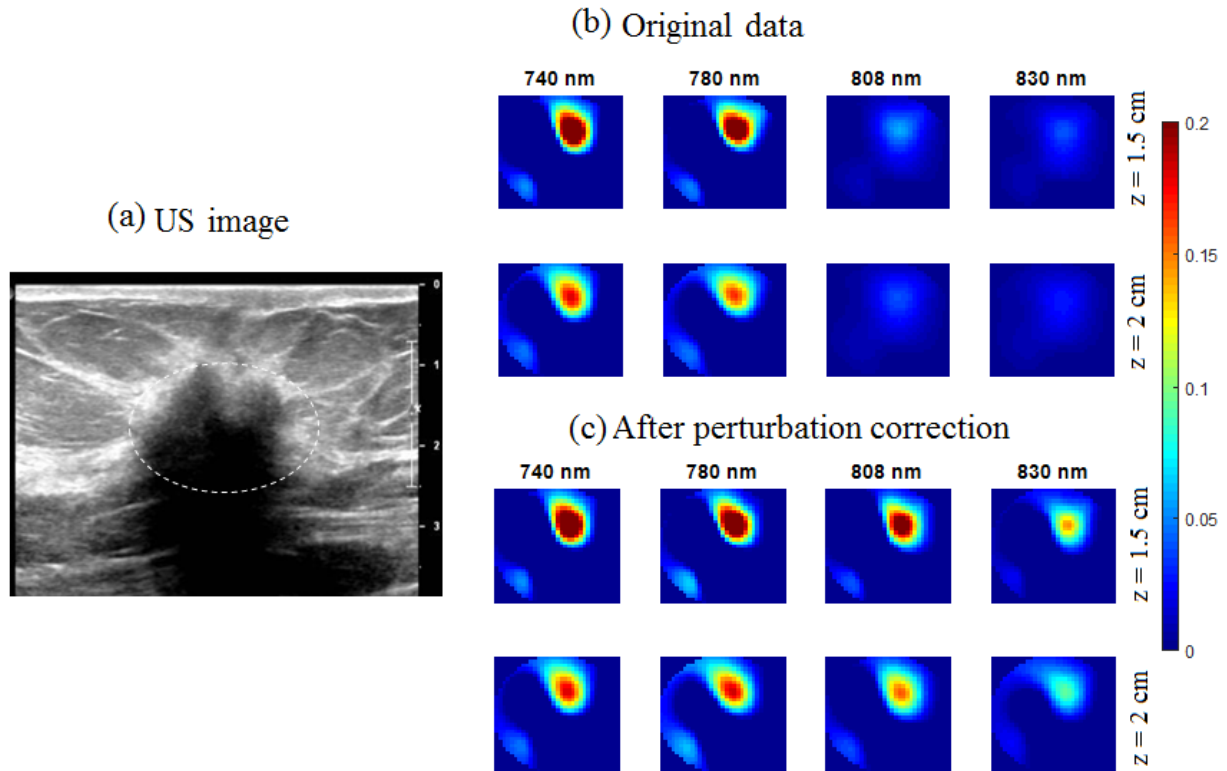
Figure 3.7: Image artifact reduction for a malignant case (a) US image, 1.5 and 2 cm lesion depths (b) absorption maps for original data before perturbation correction (c) absorption maps after perturbation correction

Figure 3.8 shows iterative changes of perturbation and absorption maps for the malignant case at 808 nm. In iteration 0, we have original dataset and absorption map similar to that in Figure 3.7(b). In successive iterations we removed perturbation points denoted by red dots. We continue to remove perturbations until absorption map is structurally similar to maps of other wavelengths.
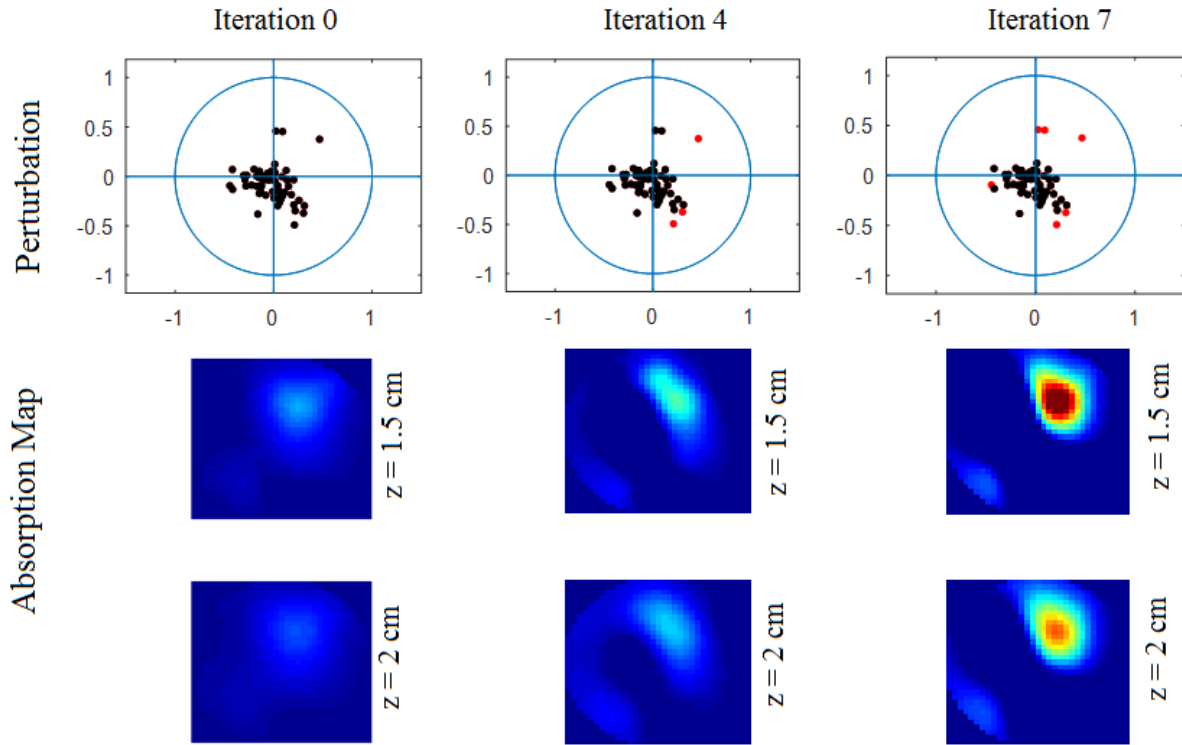
Figure 3.8: Iterative changes of absorption map and perturbation filtered at 808 nm, for the malignant case. Red dots denote removed data points.

Another malignant example with small tumor is shown in Figure 3.9. Figure 3.9(a) shows the ultrasound image with lesion marked by white ellipse. Figure 3.9(b) shows reconstructed absorption maps for four wavelengths. Each wavelength absorption map shows only 1 layer at depth, $z = 1.5\ cm$. Mean image similarity indices for four wavelengths 740, 780, 808, 830 nm are 0.86, 0.84, 0.85, 0.81 and reconstructed absorption coefficients are 0.2509 cm^{-1}, 0.2289 cm^{-1}, 0.2440 cm^{-1} and 0.3182 cm^{-1} respectively. Image artifact is present in 808 and 830 nm absorption maps. Figure 3.9(c) shows reconstructed absorption maps after perturbation correction. Mean SSIMs for four wavelengths changes to 0.93, 0.94, 0.93, 0.92 while reconstructed absorption coefficients changed to 0.2509 cm^{-1}, 0.2289 cm^{-1}, 0.2658 cm^{-1} and 0.2623 cm^{-1}, respectively.
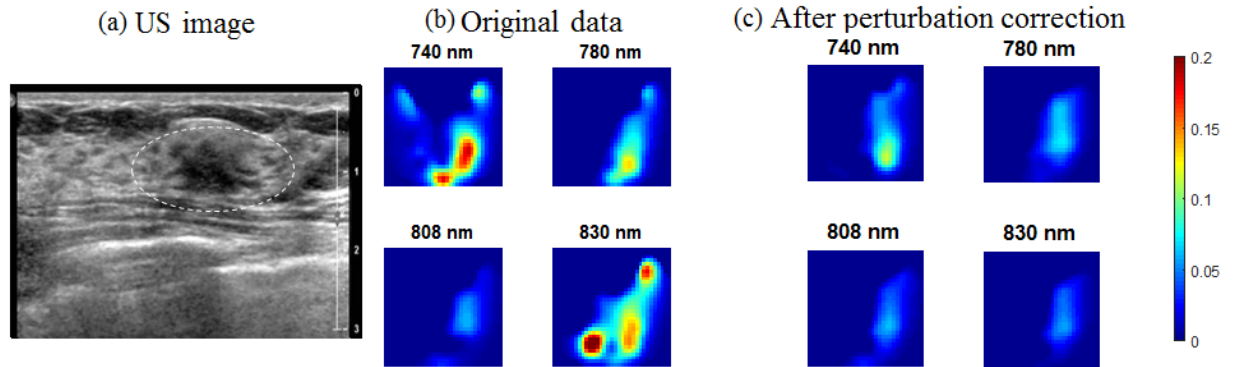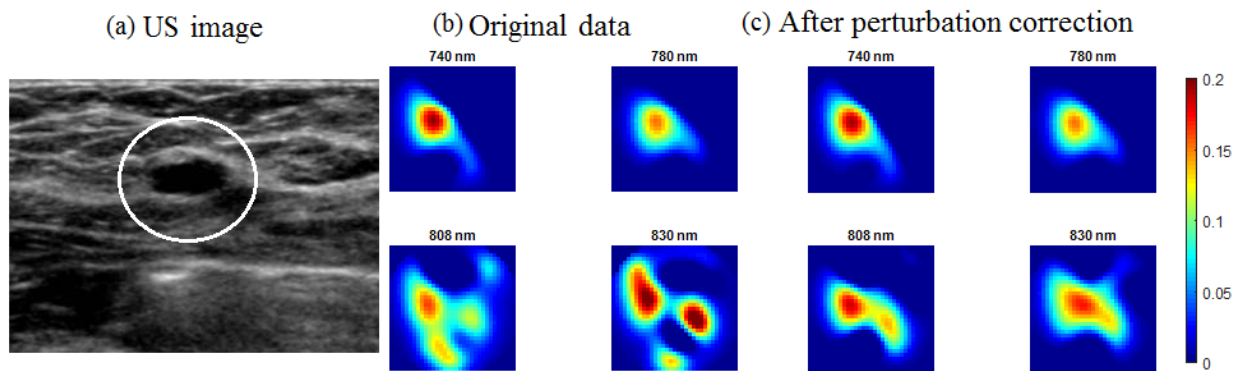
Figure 3.9: Image Artifact reduction for a malignant case (a) US image (b) absorption maps for original data before perturbation correction (c)absorption maps after perturbation correction

Iterative change of perturbation and absorption map for the malignant case for 830 nm wavelength is shown in figure 3.10. In iteration 0, we have original dataset and absorption map similar to that in figure 3.9(b). In successive iterations we removed perturbation points denoted by red dots. We continue to remove perturbations until absorption map is structurally similar to maps of other wavelengths.
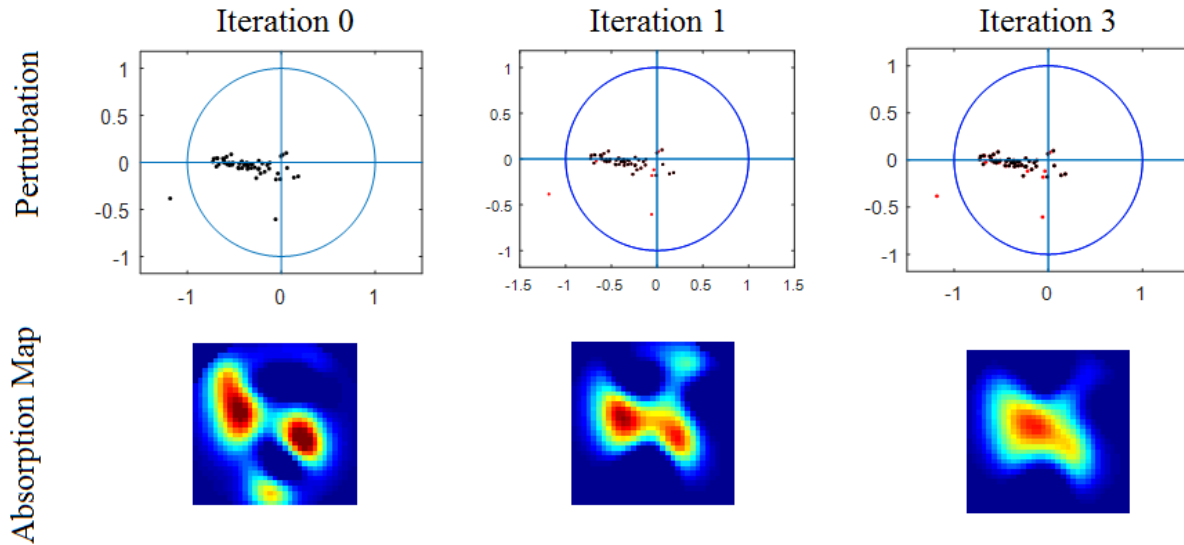
Figure 3.10: Iterative change of absorption map and perturbation filtering for wavelength 830 nm for a malignant case. Red dots denote removed data points.

Perturbation correction statistically improves the SSIM among different wavelengths, as depicted in Figure 3.11. A two-tailed paired t-test was done for images with artifacts both before and after perturbation correction, and the SSIM is statistically higher after perturbation correction, with a p-value less than 0.001. Student t-test on images with no artifacts shows no significant change in terms of structural similarity (p-value 0.52), which is expected.
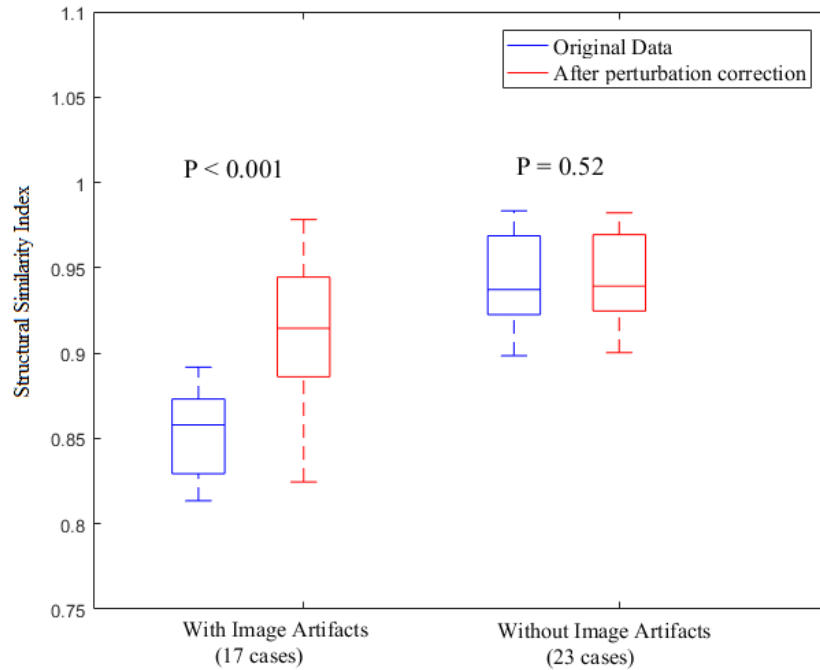
Figure 3.11: Comparison of SSIMs of reconstructed images before perturbation correction (blue box) and after perturbation correction (red box)

3.3.3 Perturbation correction vs Noise based down-weighting

An alternative method to complete removal of outlier data is to down weight the noisy data. The measurements are properly weighted in the inverse problem using variance of repeated measurements collected from each location of tissue in individual wavelength reconstruction solving a weighted least square problem [18]. Detailed procedures and findings are discussed below.

Given the measurement vector x, unknown optical property, θ and system matrix, H, linear model can be written as,

$$x = H\theta + w \qquad\qquad \text{Eq. (3.7)}$$

Where, θ has random prior PDF $N(\mu_\theta, C_\theta)$ and noise vector, w has a statistical characterization, $N(0, C_w)$ i.e. zero mean gaussian noise.

The posterior PDF of the optical properties, $p(\theta|x)$ has mean,

$$E(\theta|x) = \mu_\theta + \left(C_\theta^{-1} + H^T C_w^{-1} H\right)^{-1} H^T C_w^{-1}(x - H\mu_\theta) \qquad\qquad \text{Eq. (3.8)}$$

We take three repeated measurements for a benign patient from a particular tumor location. For each source-detector pair, variance of these three measurements are taken and then diagonalized to make noise covariance matrix, C_w. This method should appropriately down weight the measurement with higher measurement variance instead of completely removing them.

Results from the aforementioned algorithm are compared with the proposed algorithm in figure 3.12 for the benign case presented in figure 3.5. Maximum absorption coefficients for different algorithms are presented in Table 1.
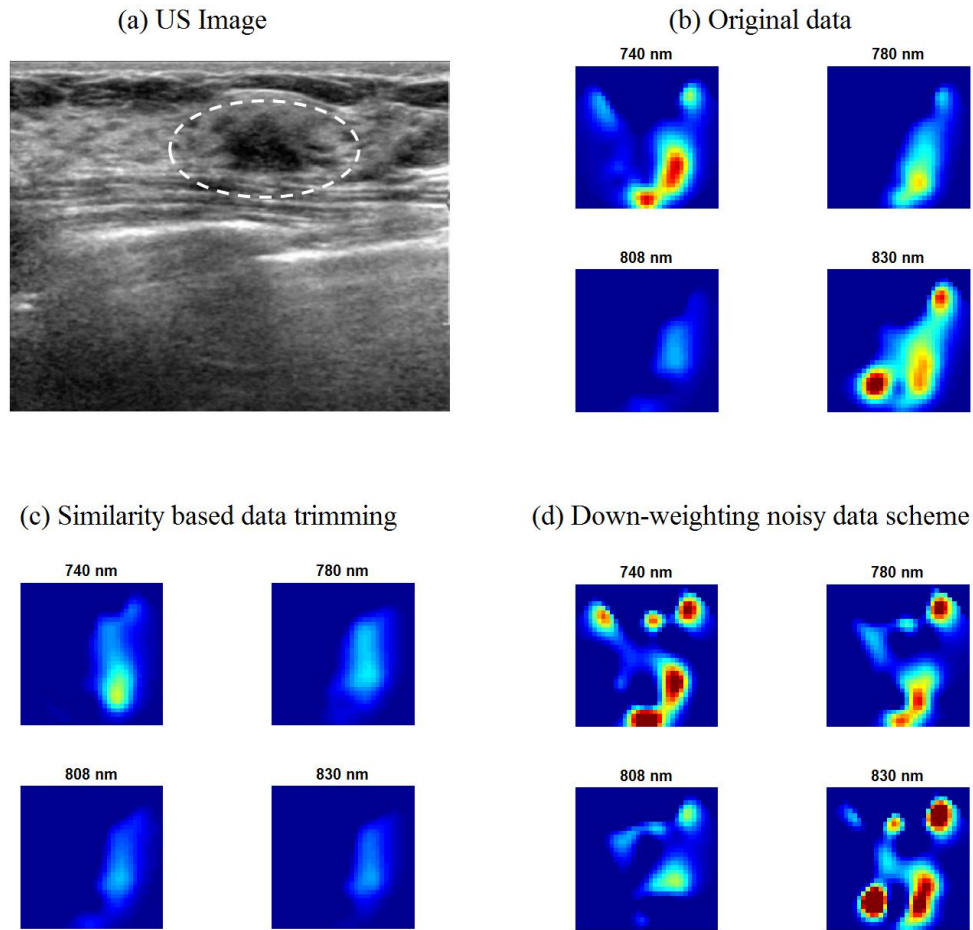
Figure 3.12: Comparison of Reconstructed absorption maps for different perturbation correction approaches (a) US image (b) Original Data (c) Image similarity-based data trimming approach (d) measurement variance based noisy data down-weighting approach

Table 3.2: Maximum absorption coefficient (cm^{-1}) for different perturbation correction approaches

	740 nm	780 nm	808 nm	830 nm
Original Data	0.24	0.21	0.13	0.33
Data trimming approach	0.16	0.15	0.13	0.15

Noise data down-weighting scheme	0.40	0.31	0.18	0.52

As we can see from the results, down weighting the noisy data didn't help in accurately reconstructing absorption maps for a benign case resulting in much higher artifacts. This may not be surprising. Our system noise comprises of both coherent and incoherent components and modeling it as a white additive noise may not be the best choice for our system. For our reconstruction, we avoid artifact from noisy data using regularization or early stopping in our iterative optimization problem [19]. Availability of a good prior is also crucial for our reconstruction. Thus, due to the lack of a good noise characterization and good prior PDF of optical properties, alternative method may not be useful in our case.

3.4 Summary and Discussion

In summary, an iterative perturbation correction algorithm based on image similarity is introduced and its performance in image artifact reduction is demonstrated using clinical data. This algorithm follows two simple assumptions. First, absorption map images for all four wavelengths are assumed to be structurally similar. Since we are imaging the same tissue region with closely spaced wavelengths, the image structure should be similar, even though the local absorption coefficients might differ due to wavelength-dependent absorption variations. Second, image artifacts in all four wavelengths are assumed to be dissimilar. Data acquisition is done sequentially, from one wavelength after another, in a few seconds. Motion or experimental errors can affect one or more wavelengths, but these effects are random and are unlikely to generate structurally similar artifacts at all four wavelengths. Additionally, certain tissue heterogeneity caused artifacts may

73

not be present at all wavelengths, for example 740 nm is very sensitive to dark skin pigment than other wavelengths. The total hemoglobin distribution, which is calculated by linear weighting of multi-wavelength absorption maps based on extinction coefficients, is significantly improved due to artifacts reduction. However, the average maximum total hemoglobin levels which we have used to classify malignant vs. benign lesions remain statistically the same as compared with no perturbation correction. This is because one or two absorption distributions are often significantly improved on artifacts, but the maximum total hemoglobin level may not change much.

Other approaches, such as weighted least-square (WLS) approach [18, Chapter 4], can compensate measurement differences between different wavelengths (or source/detector channels). Such method depends on the accurate modeling of the system noise. However, the noise in the DOT measurements includes coherent and incoherent components as well as random motion produced noise. We have evaluated the WLS approach to compensate measurement differences among source-detector pairs and found that it may not be suitable for the measurement noise we experienced in patient data.

The proposed iterative artifact reduction algorithm significantly reduces the effect of wavelength-dependent measurement errors in DOT perturbation, which helps to achieve more accurate reconstruction of the optical properties of breast lesions. This automated method also helps to minimize both the user interface and the time for data preprocessing. The average time for an experienced user to manually perform data preprocessing for one patient's data is from 15 minutes to 30 minutes. The automated method could reduce this time to less than a minute and facilitate the clinical translation of US-guided DOT technology. Although the method is demonstrated using ultrasound-guided DOT data, it is applicable to any DOT data preprocessing obtained with multiple wavelengths.

References

1. Boas, David A., Thomas Gaudette, and Simon R. Arridge. "Simultaneous imaging and optode calibration with diffuse optical tomography." Optics express 8, no. 5 (2001): 263-270.

2. Stott, Jonathan J., Joseph P. Culver, Simon R. Arridge, and David A. Boas. "Optode positional calibration in diffuse optical tomography." Applied optics 42, no. 16 (2003): 3154-3162.

3. Chen, Nan Guang, Puyun Guo, Shikui Yan, Daqing Piao, and Quing Zhu. "Simultaneous near-infrared diffusive light and ultrasound imaging." Applied optics 40, no. 34 (2001): 6367-6380.

4. Culver, Joseph P., Andrew M. Siegel, Jonathan J. Stott, and David A. Boas. "Volumetric diffuse optical tomography of brain activity." Optics letters 28, no. 21 (2003): 2061-2063.

5. Stott JJ, Culver JP, Arridge SR, Boas DA. Optode positional calibration in diffuse optical tomography. Appl Opt [Internet]. OSA; 2003 Jun;42(16):3154–62. Available from: http://ao.osa.org/abstract.cfm?URI=ao-42-16-3154

6. Schweiger M, Nissilä I, Boas DA, Arridge SR. Image reconstruction in optical tomography in the presence of coupling errors. Applied optics. Optical Society of America; 2007;46(14):2743–56.

7. Mozumder M, Tarvainen T, Arridge SR, Kaipio J, Kolehmainen V. Compensation of optode sensitivity and position errors in diffuse optical tomography using the

approximation error approach. Biomedical optics express. Optical Society of America; 2013;4(10):2015–31.

8. Fukuzawa R, Hoshi Y, Fukuzawa R, Okawa S, Matsuhashi S, Kusaka T, et al. Reduction of image artifacts induced by change in the optode coupling in time-resolved diffuse optical tomography in the optode coupling in time-resolved diffuse. 2017;

9. Scholkmann, Felix, Sonja Spichtig, Thomas Muehlemann, and Martin Wolf. "How to detect and reduce movement artifacts in near-infrared imaging using moving standard deviation and spline interpolation." Physiological measurement 31, no. 5 (2010): 649.

10. Izzetoglu, Meltem, Prabhakar Chitrapu, Scott Bunce, and Banu Onaral. "Motion artifact cancellation in NIR spectroscopy using discrete Kalman filtering." Biomedical engineering online 9, no. 1 (2010): 16.

11. Molavi, Behnam, and Guy A. Dumont. "Wavelet-based motion artifact removal for functional near-infrared spectroscopy." Physiological measurement 33, no. 2 (2012): 259.

12. Niu, Haijing, Ping Guo, Lijun Ji, Qing Zhao, and Tianzi Jiang. "Improving image quality of diffuse optical tomography with a projection-error-based adaptive regularization method." Optics express 16, no. 17 (2008): 12423-12434.

13. Vavadi, Hamed, and Quing Zhu. "Automated data selection method to improve robustness of diffuse optical tomography for breast cancer imaging." Biomedical optics express 7, no. 10 (2016): 4007-4020.

14. Althobaiti, Murad, Hamed Vavadi, and Quing Zhu. "An Automated Preprocessing Method for Diffuse Optical Tomography to Improve Breast Cancer Diagnosis." Technology in Cancer Research & Treatment 17 (2018): 1533033818802791.

15. Uddin, KM Shihab, and Quing Zhu. "Reducing image artifact in diffuse optical tomography by iterative perturbation correction based on multiwavelength measurements." Journal of biomedical optics 24, no. 5 (2019): 056005.

16. Wang, Zhou, Alan C. Bovik, Hamid R. Sheikh, and Eero P. Simoncelli. "Image quality assessment: from error visibility to structural similarity." IEEE transactions on image processing 13, no. 4 (2004): 600-612.

17. Renieblas, Gabriel Prieto, Agustín Turrero Nogués, Alberto Muñoz González, Nieves Gómez León, and Eduardo Guibelalde del Castillo. "Structural similarity index family for image quality assessment in radiological images." Journal of Medical Imaging 4, no. 3 (2017): 035501.

18. Steven M. Kay. 1993. Fundamentals of Statistical Signal Processing: Estimation Theory. Prentice-Hall, Inc., Upper Saddle River, NJ, USA.

19. Uddin, KM Shihab, Atahar Mostafa, Mark Anastasio, and Quing Zhu. "Two step imaging reconstruction using truncated pseudoinverse as a preliminary estimate in ultrasound guided diffuse optical tomography." Biomedical optics express 8, no. 12 (2017): 5437-5449.

Chapter 4: Optimal Breast Cancer Diagnostic Strategy

4.1 Introduction

Multiple imaging modalities are currently used for breast cancer screening and diagnosis. X-ray mammography is the predominant imaging modality for both screening and diagnostic imaging. Breast Ultrasound (US) is the second most common diagnostic imaging modality and is also used for screening average to moderate risk women with dense breast composition [1-3]. Due to its high cost and limited access, MRI is reserved for screening high risk women and has application to a very narrow group of diagnostic indications. While the characteristics of malignant and benign breast lesions are well established by conventional imaging techniques [4-6], their overlapping appearances result in approximately one million image-guided breast biopsies each year in the United States, most yielding benign results [7]. An optical tomography system that reveals functional differences in breast abnormalities could greatly improve diagnostic accuracy and reduce the number of benign biopsies. In the last 20 years, optical breast imaging using diffused light has been widely explored to develop non-invasive imaging tools to detect and diagnose breast cancer, and to predict and monitor its treatment response [8-26]. Initially these systems were investigated as primary or 'stand-alone' modalities [8-15]. However, it became clear that the accuracy of DOT could be enhanced on lesion localization and quantification by use of a priori information from other conventional breast imaging modalities like mammography/ tomosynthesis [24-25], ultrasound (US) [16-17,20,26] and MRI [21-23]. The dual-modality characterization, incorporating structure from conventional imaging and function from enhanced optical imaging,

provides complementary information to improve diagnosis. Ultrasound-guided DOT has demonstrated its translational potential for distinguishing breast cancers from benign lesions [16-17, 26], and for predicting and monitoring the neoadjuvant chemotherapy (NAC) response of breast cancers [18,27]. One major challenge for dual-modality breast cancer diagnosis is DOT's relatively slow data processing and image reconstruction speed as compared to the real-time imaging capabilities of US. Near real-time diagnosis is critical for the clinical translation of a US-guided DOT dual-modality technique. The random forest classifier is an ensemble learning method that has been employed widely in medical imaging applications [28]. It makes a decision based on majority vote of many individual decision trees which are trained on predictive features [29]. Random forest classifiers have demonstrated promising results for computer aided breast cancer diagnosis utilizing US [30], mammogram [31] and biopsy data [32-33].

In this chapter, we investigate a two-stage diagnostic strategy for breast cancer clinical management. The first stage seeks to identify benign lesions in near real-time based on radiologists' US scores and DOT measurements in the form of perturbation data that have not undergone image reconstruction. This is accomplished by use of a random forest classifier. Intermediate lesions that cannot be identified as benign with high confidence are flagged and functional images are subsequently reconstructed off-line from the DOT measurements. In the second stage of the diagnostic strategy, features are extracted from the reconstructed DOT images and a supper Vector Machine (SVM) classifier is employed for diagnosis. This proposed diagnostic strategy has showed significant improvement over DOT functional feature and US based diagnosis only by increasing AUC (area under ROC curve) from 0.892 to 0.937. To the best of our knowledge, this is the first time a two-step automated diagnostic strategy is proposed with near real-time assessment capability of majority of benign lesions.

4.2 Materials and methods

4.2.1 DOT perturbation features

The DOT perturbation, U_{sc}, is defined as normalized difference between lesion and reference measurements, which is related to differential absorption of lesion and reference normal tissue. For the ith source-detector pair,

$$U_{sc}(i) = \frac{A_l(i)e^{j\varphi_l(i)} - A_r(i)e^{j\varphi_r(i)}}{A_r(i)e^{j\varphi_r(i)}} = \frac{A_l(i)e^{j\varphi_l(i)}}{A_r(i)e^{j\varphi_r(i)}} - 1 \qquad i = 1,2,\dots\dots\dots m \qquad \text{Eq. (4.1)}$$

where m is the number of measurements, $U_l(i) = A_r(i)e^{j\varphi_r(i)}$ and $U_r(i) = A_l(i)e^{j\varphi_l(i)}$ are lesion and reference measurements, respectively. A two-dimensional representation of DOT perturbation measurements is shown in Fig. 4.1(a) for benign and Fig. 4.1(b) for malignant lesion. The unit circle represents the expected boundary for perturbation data. A convex hull or envelope of the data distribution is marked by a black polygon. For benign lesions, perturbation is skewed towards positive real axis or evenly distributed around both positive and negative real axis while perturbation for malignant lesion is skewed toward negative real axis due to high absorption of cancer which leads to lower ratio of $\frac{A_l(i)}{A_r(i)}$ (eq. (4.1), [34]). This difference in data distribution are quantified by data features extracted from the perturbation that are useful in differentiation of benign and malignant lesions.

(a) Benign perturbation data   (b) Malignant perturbation data
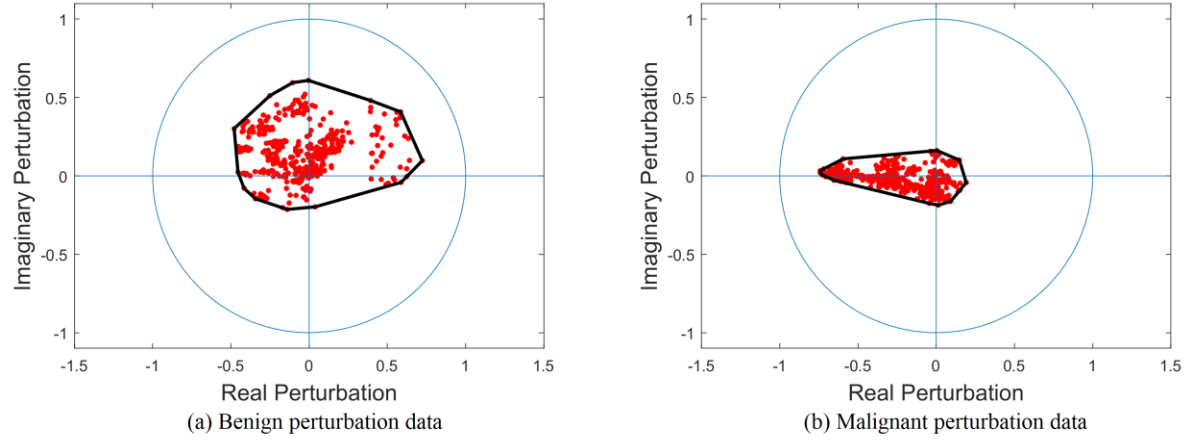
Figure 4.1: Two-dimensional representation of perturbation measurements for (a) Benign lesion, (b) Malignant lesion. The convex hull is marked by black polygon.

Two sets of DOT data features were extracted from perturbation measurements: morphological features from convex hull of data distribution and histogram features. Four features extracted from the convex hull are: area, perimeter, moment of inertia and centroidal polar moments. The moment of inertia, I_m is the quantitative measurement of resistance of an object against angular acceleration. The centroidal polar moment, I_p, denotes resistance of the object against torsion or twisting. The definition of moment of inertia and centroidal polar moment are as follows [35],

$$I_m = \int r^2 dm, \qquad I_p = \int r^2 dA, \qquad\qquad \text{Eq. (4.2)}$$

Where, dm and dA are differential mass and area elements respectively and r is the distance from axis of rotation to these elements.

For each lesion, all measurements were compiled to generate two separate univariate histograms of the real and imaginary perturbations. A representative example of univariate histogram for a benign lesion is shown in Fig. 4.2(a) for real perturbation and Fig. 4.2(b) for imaginary

perturbation. A histogram of a malignant lesion is shown in Fig. 4.2(d) for real perturbation and 4.2(e) for imaginary perturbation. From each histogram, six features - mean, standard deviation, skewness, kurtosis, energy and entropy - were extracted. In total we obtained 12 features from these two univariate histograms. Real and imaginary perturbations were used together to obtain a bivariate histogram as shown in Fig. 4.2(c) for benign and 4.2(f) for malignant case. Four features of mean distance from the centroid, standard deviation of distance from the centroid, multivariate skewness and multivariate kurtosis are calculated from each bivariate histogram. Two tailed t-test was performed for each feature to calculate p-value, which is an estimate of the predictive capability of the respective feature. All features were ranked in the ascending order of p-values and features with p-value less than 0.05 are used in the classification. A total of 12 features were found significant and used in the random forest classifier described below.
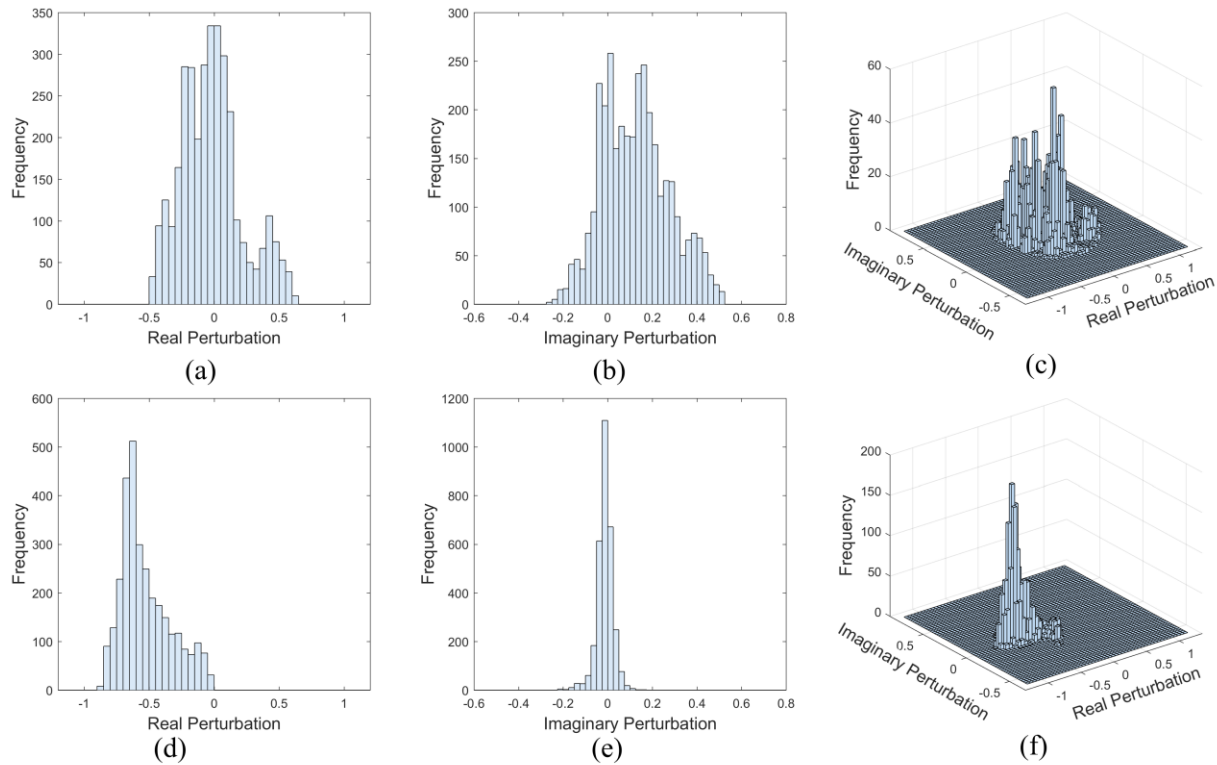
Figure 4.2: Example histogram from a benign lesion perturbation. (a) univariate histogram for real perturbation, (b) univariate histogram for imaginary perturbation, and (c) bivariate histogram. Example histogram from a malignant lesion perturbation. (d) univariate histogram for real perturbation, (e) univariate histogram for imaginary perturbation, and (f) bivariate histogram.

4.2.2 Patients and Ultrasound BIRADS grading

A total of 188 patients were studied for evaluating the proposed diagnostic scheme with 47 patients having malignant lesions and 141 with benign lesions based on biopsy results. The clinical study was approved by the local Institutional Review Board and was compliant with the Health Insurance

Portability and Accountability Act. Informed consent was signed by each patient. Data used in this study were obtained from an earlier study and patients were de-identified [26].

For each lesion, a sequence of US images was obtained and retrospectively reviewed by two radiologists who were blind to optical results. The lesions were graded using Breast Imaging Reporting and Data System (BI-RADS) based on US. For each lesion, one of the four grades were given, 4A, 4B, 4C and 5 based on the suspicion level of malignancy. BI-RADS 4A refers to ≤10% likelihood of malignancy while 4B, 4C and 5 denotes 10% to 50%, 50% to 95% and ≥95% likelihood of malignancy [4]. In the classification process, all BI-RADS grades (4A to 5) were encoded into numeric number from 0 (4A), 1(4B), 2(4C) and 3 (5) inclusive in step of 1 based on increasing suspicion level. These numerical scores from two radiologists were used as 2 additional features along with 12 perturbation features in random forest classifier.

4.2.3 Random Forest Classifier

A random forest is an ensemble of decision tree classifiers where each decision tree independently casts vote for a certain class based on randomly chosen subset of all features. The final outcome of the forest is based on majority voting of all the trees. In this study, total 14 features including 12 perturbation features and 2 sets of US BIRADS scores from two radiologists were used for classification. The random forest classifier employed in this study consisted of 50 decision trees (CART). Each tree works on 6 randomly selected features out of 14 features. Information gain is used to calculate the best split at each decision tree node. Decision trees can safely handle correlated features too, since once a feature is used to split the samples, information gain on the split samples in the child node would be lower for correlated features [36-37]. Another feature of

random forest classifiers is that they can possess attractive bias-variance trade-offs if suitably defined. To realize this, in this study, we limited each individual decision tree depth to five and number of minimum required samples to split a node is set to four.

4.2.4 DOT Functional features

In DOT image reconstruction, the entire 3-dimensional breast volume to be reconstructed is segmented into voxels with finer voxels within a lesion area identified by the co-registered US image and coarse voxels in the background region [38]. Fitted optical properties from the contralateral reference breast measurements are used to calculate weight matrix W (chapter 1, section 2) for the voxels. The total absorption of each voxel is reconstructed and then divided by the voxel volume to obtain differential optical absorption coefficient, $\delta\mu_a$. The inverse problem is linearized by use of the Born approximation to obtain a linear equation relating changes of optical absorption coefficients to perturbation measurement, U_{sc},

$$[U_{sc}]_{m\times 1} = [W_L, W_B]_{m\times n} \begin{bmatrix} \delta\mu_{aL} \\ \delta\mu_{aB} \end{bmatrix}_{n\times 1} \qquad \text{Eq. (4.3)}$$

$$U_{sc} = WX, \quad W = [W_L, W_B], \quad X = \begin{bmatrix} \delta\mu_{aL} \\ \delta\mu_{aB} \end{bmatrix}$$

where, W_L and W_B are voxel weights in lesion and background respectively; $\delta\mu_{aL}$ and $\delta\mu_{aB}$ are unknown optical properties of voxels in lesion and background respectively; n is the total number of voxels to be reconstructed. The optical absorption coefficients were reconstructed by solving a L2 regularized unconstrained optimization problem using conjugate gradient method [39].

$$\hat{X} = \arg\min_X(\|U_{sc} - WX\|^2 + \frac{\lambda}{2}\|X\|^2). \qquad \text{Eq. (4.4)}$$

Oxy and deoxy hemoglobin concentrations, (C_{HbO_2}, C_{Hb}), were calculated from 4 wavelength absorption maps using extinction coefficient, ε, for different wavelengths,

$$\begin{bmatrix} \mu_a^{740} \\ \mu_a^{780} \\ \mu_a^{808} \\ \mu_a^{830} \end{bmatrix} = \begin{bmatrix} \varepsilon_{Hb}^{740} & \varepsilon_{HbO_2}^{740} \\ \varepsilon_{Hb}^{780} & \varepsilon_{HbO_2}^{780} \\ \varepsilon_{Hb}^{808} & \varepsilon_{HbO_2}^{808} \\ \varepsilon_{Hb}^{830} & \varepsilon_{HbO_2}^{830} \end{bmatrix} \begin{bmatrix} C_{Hb} \\ C_{HbO_2} \end{bmatrix} . \qquad \text{Eq. (4.5)}$$

The total hemoglobin concentration, C_{tHb}, is defined as the summation of C_{HbO_2} and C_{Hb}.

Functional features were extracted from the reconstructed total hemoglobin map. Three features are calculated from all lesion images, C_{HbO_2}, C_{Hb}, C_{tHb}. Two features, C_{HbO_2} and C_{tHb}, are used in classification. The light shadowing effect was also used as a functional imaging feature [40]. Because malignant lesions are highly absorbing, photons are absorbed more by a top target layer in depth that creates shadow in deeper target layers. To quantify the light shadow effect, the shadow parameter was calculated as the average ratio of C_{tHb} calculated from the topmost layer in depth and the average of the subsequent layers in depth. An example of quantifying light shadow effect is given in Fig. 4.3. These three functional features, oxy hemoglobin, deoxy hemoglobin and light shadow parameters are the functional features used in second step of diagnosis by SVM classifier.

(a) US Image   (b) Reconstructed Hemoglobin Map
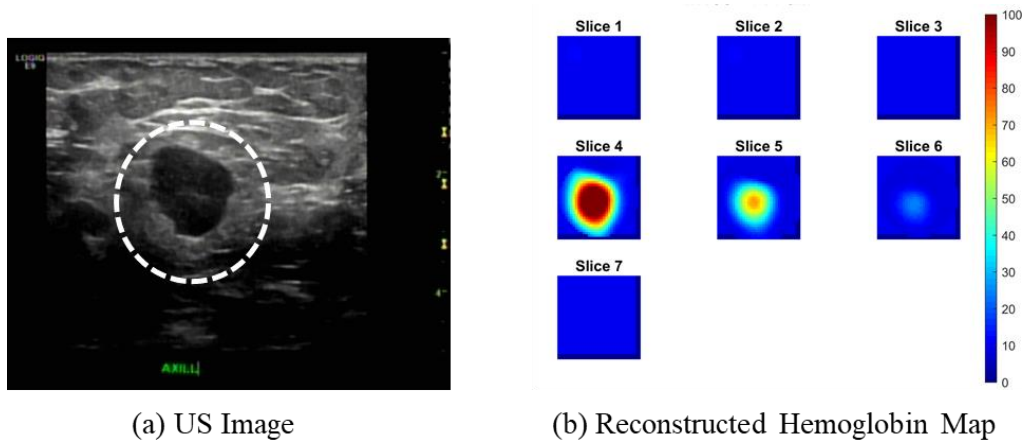
Figure 4.3: Light shadowing effect observed in large tumors. (a) US image, (b) total Hemoglobin concentration map for a large malignant lesion. Each 2D slice has dimension 4.5 cm × 4.5 cm and Slice 1 to 7 are at 0.5 cm to 3.5 cm depth with 0.5 cm increment. Mean ratio of the topmost layer in depth and the average of subsequent layers in depth is 4.52.

4.2.5 Support Vector Machine Classifier

Support vector machine (SVM) is a binary classifier that uses a linearly separating hyperplane which have maximum distance from both of the classes [41]. SVM can be extended to multiclass classification too [42]. SVM is considered non-parametric since the model parameters are not predefined and needs to be learned from training data. Hinge loss function with linear kernel and L2 regularization is used in our application. While bias of the SVM model can be decreased by the use of a nonlinear kernel e.g. gaussian kernel, more training data would be required to reduce the variance of the model. Hence, linear kernel is used for our application. Regularization parameter is selected by cross-validation on the training data. SVM is well known and widely used classifier and its detailed description can be found in ref 41.

4.2.6 Two-step Classification

Diagnosis of breast lesions was performed in two steps. Immediately after data acquisition, perturbation features were extracted, and US BIRADS scores were be obtained from radiologists. These perturbation features and BIRADS scores were used in a random forest classifier to identify lesions having high probability of benign. The total number of decision tree votes required to decide benign lesion is set to be very high so that false negative rate can be very small or nonexistent in near real-time assessment. Two-thirds of the malignant samples and same number of benign samples are used for training and rest of testing. The training set comprises of 32 malignant and 32 benign cases. The test set was comprised of the remaining 15 malignant and 109 benign cases. In this first step, all 32 benign and 32 malignant cases were used for training. Hyperparameter tuning was performed by 5-fold cross-validation on the training set.

Image reconstruction and functional feature extraction were done for lesions with intermediate diagnosis. These samples were classified using a SVM classifier based on functional features. Here, all 32 malignant cases were again used in training; however, for benign cases, lesions with higher malignancy probability were used in training. Again, hyperparameters were selected by 5-fold cross-validation performance. The test set of 15 malignant and 109 benign were not employed for training or validation. Thus, the test data were unseen to both the random forest and SVM classifiers. This entire two-step process was repeated 20 times for different random train-test split as illustrated in Fig. 4.4. At the first step in training, perturbation features and US BIRADS scores of all training samples were used to train a random forest classifier. Each decision tree outputs a binary decision of either benign or malignant for each training sample. In general, if more than half of the decision trees in the forest provide a benign decision, that sample was assumed to be benign. However, in this classification scheme, the threshold for the total number of decision tree

votes to determine benign was set as high as possible to avoid false negatives in the first step. A greedy search was applied to find the threshold. Initially the threshold i.e. number of votes required to determine benign, was set to the maximum number of decision trees, which is 50. Then the threshold was decreased in steps of 1 as long as there is no false negatives. Using this approach, the minimum threshold that provides 100% training sensitivity was achieved in the first step. While in testing, a sample was classified as 'confirmed benign' in first step only when the total number of trees voting benign is greater or equal than the threshold. In the second step of diagnosis, image reconstruction was done to obtain a hemoglobin map for the remaining samples. The maximum total hemoglobin, maximum oxy hemoglobin and light shadow quantitation parameters were extracted from the maps. These functional features were used to classify rest of the samples using SVM classifier.
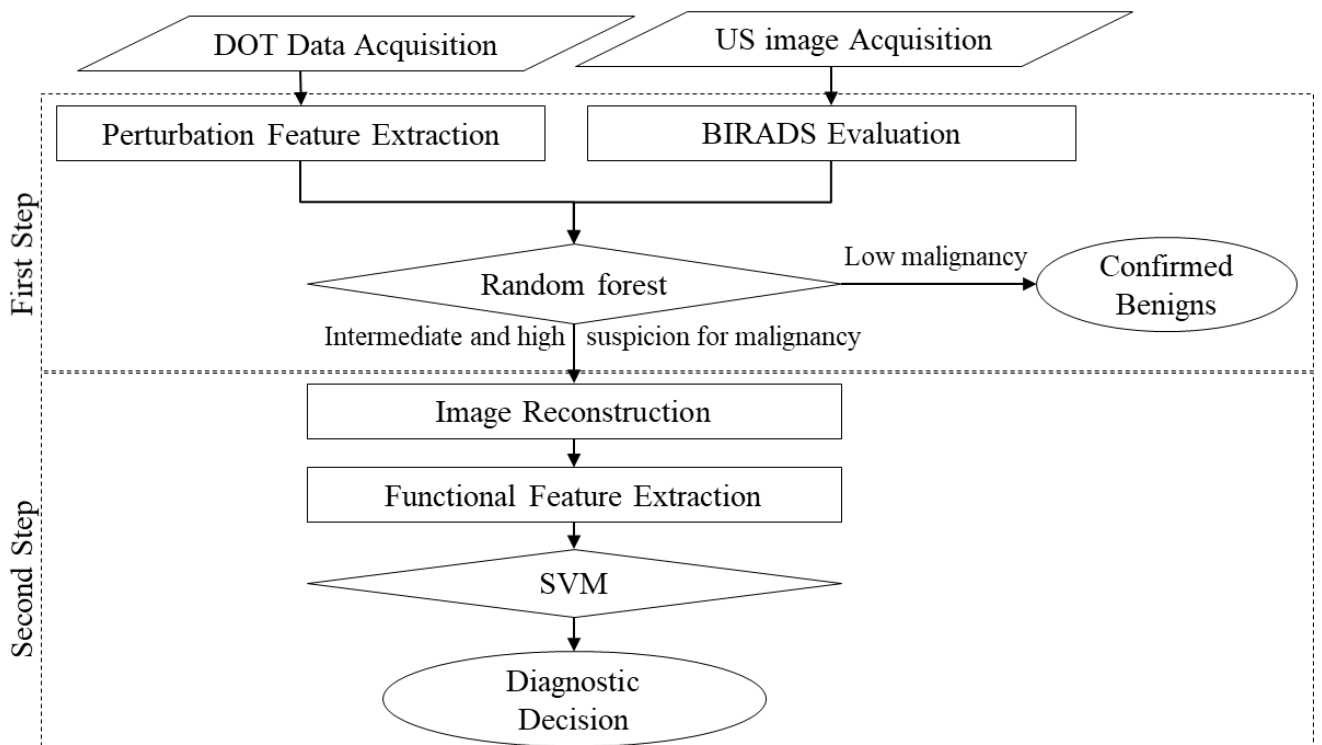
Figure 4.4: Two-step diagnosis scheme; Two different steps are denoted by dashed rectangles.

4.2.7 Performance Evaluation

To evaluate the performance of the classification algorithms, for each sample in the test set, we computed the probability of malignancy from the respective classifier. The receiver operating characteristic (ROC) curve and the area under the curve (AUC) was used as performance measure to evaluate the classifiers. 20 runs with different random train-test splits were performed for each classifier where the mean AUC denotes how well the classifier can separate benign and malignant classes and standard deviation indicates the robustness the classifier for varying training and testing data sets. Sensitivity and specificity were calculated at the threshold of 0.5 from the mean ROC curve. To evaluate the radiologists' performance, sensitivity and specificity were calculated based on BIRADS scores; 4A and 4B are grouped as benign, and 4C and 5 as malignant.

4.3 Results

4.3.1 Perturbation Feature Selection

A total of 20 features were extracted from perturbation data and listed in table 1. Box plots and p-values of all significant features are shown in Fig. 4.5.

Table 4.1: List of extracted perturbation features; Corresponding p-value for each feature is shown in brackets next to it.

Histogram features			Morphological features
Univariate (Real)	Univariate (Imaginary)	Bivariate	Convex hull
• Mean (P<0.001)	• Mean (P=0.034)	• Mean (P=0.261)	• Area (P=0.001)
• Standard deviation (P=0.006)	• Standard deviation (P=0.064)	• Standard deviation (P=0.015)	• Perimeter (P<0.001)
• Skewness (P=0.097)	• Skewness (P=0.039)	• Skewness (P=0.136)	• Moment of inertia (P=0.102)
• Kurtosis (P<0.001)	• Kurtosis (P=0.329)	• Kurtosis (P=0.033)	• Centroidal polar moment (P=0.018)
• Energy (P=0.432)	• Energy (P=0.026)		
• Entropy (P=0.153)	• Entropy (P=0.019)		
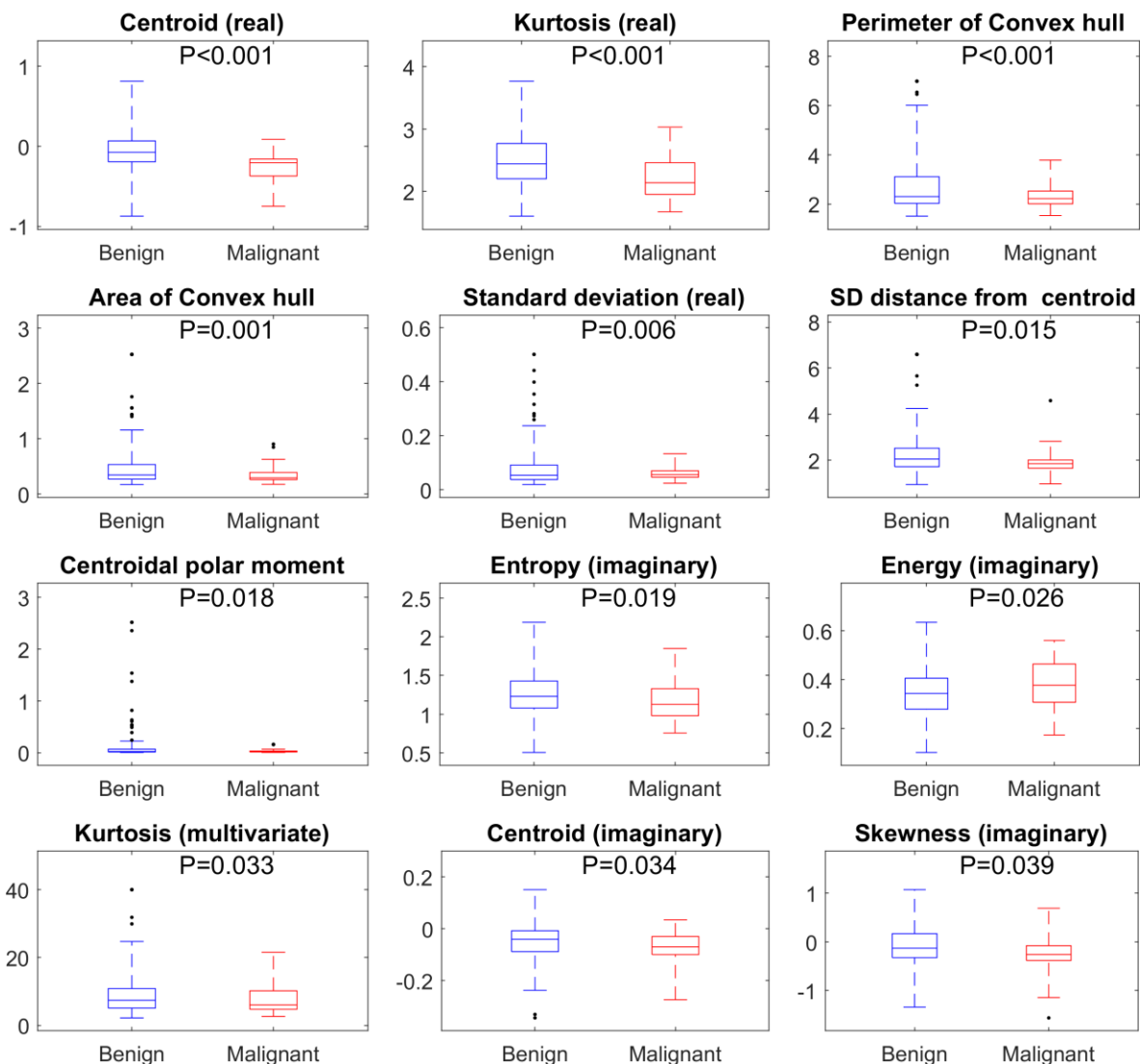
Figure 4.5: Boxplot with p-values for selected statistically significant perturbation features.

4.3.2 Clinical Study Results

To evaluate Using BI-RADS scores only and grouping 4A and 4B as benign, and 4C and 5 as malignant, the sensitivities for radiologist I and II were 70.9% ($\pm$0.3%) and 85.6% ($\pm$0.2%), and the specificities were 90.8% ($\pm$2.2%) and 63.5% ($\pm$2.4%), respectively. The ROC curves for

radiologist I and II are shown in Fig. 4.6(a) and 4.6(b), with AUC value 0.848±0.003 and 0.783±0.031 respectively. The blue curve and the light blue shade denote the mean and standard deviation of 20 ROC curves obtained from 20 runs. Using functional features only in the SVM classifier, the AUC was 0.781±0.048, as shown in Fig. 4.6(c) with a sensitivity of 82.5% (±4.2%) and specificity of 72.9% (±1.0%). Using BIARDS scores along with functional features in the SVM classifier improved the AUC to 0.892 ± 0.027 (Fig. 4.6(d)), with a sensitivity of 90.2% (±1.9%) and specificity of 74.5% (±1.3%). The proposed two-step diagnosis significantly improved the AUC to 0.937 ± 0.009 (Fig. 4.6(e)), with a sensitivity of 91.4% (±0.6%) and specificity of 85.7% (±0.8%). In the first step of the two-step method, 64.8% (±4.7%) benign samples were classified as benign by the random forest classifier. Even though a zero false negative rate was enforced in training, 1.9% (±0.6%) of malignant samples were misclassified as benign in testing in the first step. AUC for all different diagnostic schemes are summarized in Table 4.2.

(a) US BI-RADS Radiologist I

(b) US BI-RADS Radiologist II

(c) Functional features only

(d) Functional features with US

(e) Two-step diagnostic scheme
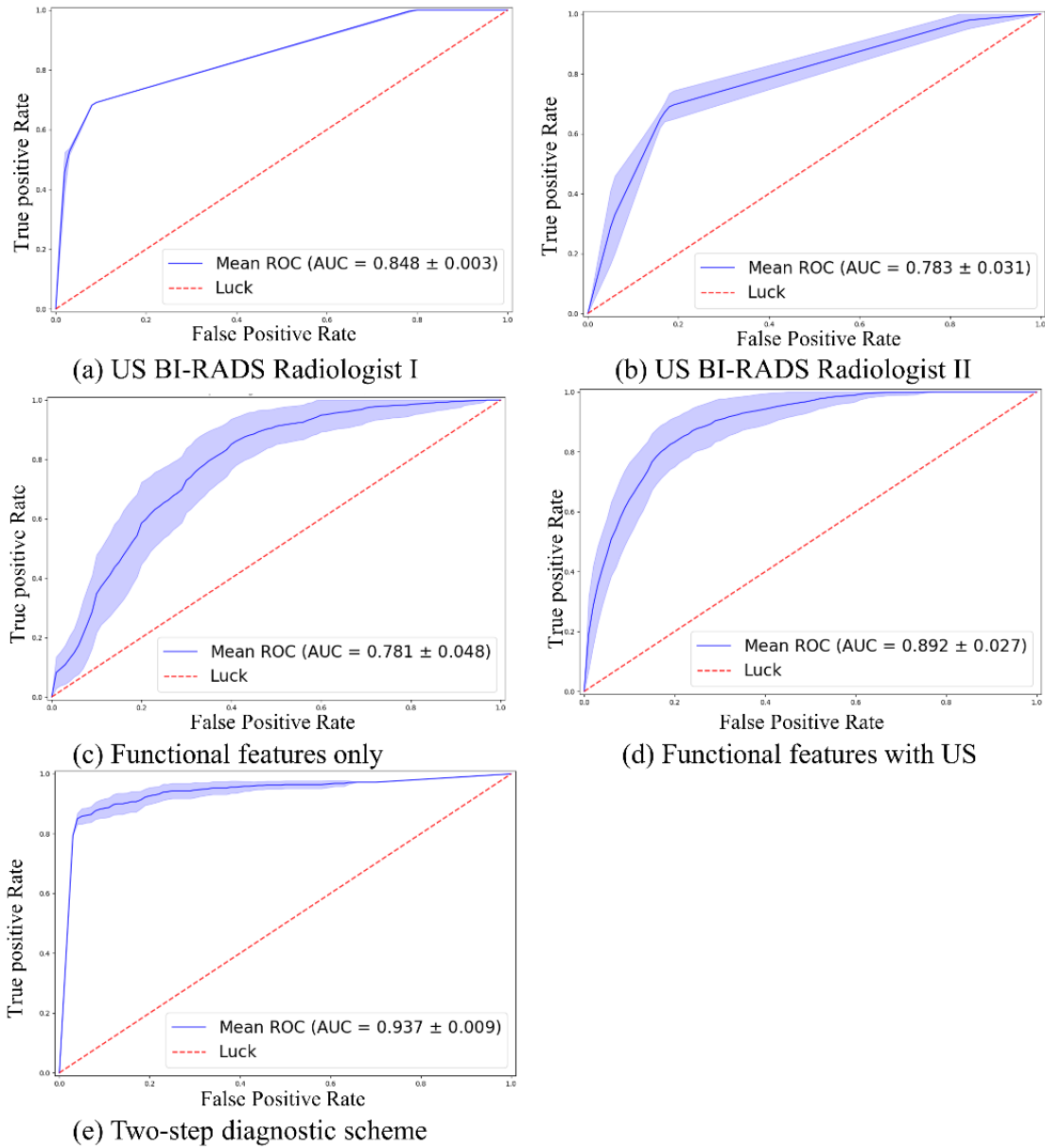
Figure 4.6: ROC curves of different classification methods. (a) BI-RADS score for radiologist I, (b)BI-RADS score for radiologist II, (c) functional feature only, using SVM. (d) BI-RADS score with functional features using SVM. (e) Proposed two-step diagnostic scheme.

Table 4.2: AUC, sensitivity and specificity of different diagnostic methods

Diagnostic Methods	US BI-RADS Radiologist I	US BI-RADS Radiologist II	Functional Feature only	Functional Feature with US BI-RADS	Two-Step Diagnostic Scheme
AUC (mean±std)	0.848±0.003	0.783±0.031	0.781±0.048	0.892±0.027	0.937±0.009
Sensitivity (mean±std)	70.9±0.3%	90.8±2.2%	82.5±4.2%	90.2±1.9%	91.4±0.6%
Specificity (mean±std)	85.6±0.2%	63.5±2.4%	72.9±1.0%	74.5±1.3%	85.7±0.8%

4.4 Summary and Discussion

Deep In summary, a novel breast cancer diagnostic strategy based on a two-step classification strategy was proposed and validated with a large pool of patient data. This strategy involves near real-time automated assessment using a random forest classifier to filter out highly probable benign lesions based on perturbation data and US BI-RADS scores. Lesions that cannot be identified as benign with high confidence are flagged, and their functional images are subsequently reconstructed off-line from the corresponding DOT measurements. In the second stage of the diagnostic strategy, features are extracted from the reconstructed DOT images, and a Support Vector Machine (SVM) classifier is employed for diagnosis. Functional feature extraction can take up to two hours including manual US image segmentation and optical image reconstruction with artifact evaluation. However, these steps are critical to provide high diagnostic accuracy.

The random forest classifier reliably predicted more than half of benign lesions in near real time, shortly after perturbation features were extracted and radiologist's BI-RADS scores were

available. In practice, BI-RADS are typically available within a few minutes after the patient exam. Such rapid diagnosis helps advance clinical management by identifying highly probable benign lesions and allowing the physicians to comfortably recommend follow-up instead of biopsy or surgical removal of the lesions. Additionally, US BI-RADS evaluation is highly dependent on the radiologist's experience; while the random forest classifier combines sensitive perturbation data with the BI-RADS to provide an improved diagnosis over that of a radiologist alone.

The two-step diagnosis scheme improves the specificity of a breast cancer diagnosis over a diagnosis based on the BI-RADS score and DOT-derived functional parameters only. This improvement is due to the diagnosis of highly probable benign lesions by the random forest classifier. A lower standard deviation across multiple cross-validations indicated this approach is very robust to different training and testing datasets and hence more reliable. Introducing perturbation features in the first step improved the overall diagnostic performance and facilitated better clinical management of the benign lesions to reduce unnecessary biopsies. Although a hemoglobin map is reconstructed from perturbation data, the tumor size and location provided by co-registered US and the breast tissue optical background properties are also used in the reconstruction process. The tumor size and location define the fine mesh area and location, and the background optical properties are used to calculate the weight matrix. Thus, for similar perturbation data, the reconstructed functional features can be different for different background properties, and lesion dimensions and locations. Our results suggest that this additional information employed when reconstructing functional features is valuable to further differentiate benign and malignant lesions.

For large benign lesions, even if the absorption coefficient is high, the hemoglobin concentration map shows less light shadowing and a more uniform distribution in depth, which is critical in

differentiating large benign lesions and malignant tumors. For low grade carcinomas (14.63% in this study), the detection sensitivity of DOT can be lower due to the low level of tumor angiogenesis, however, the distorted tumor morphology evaluated by US BI-RADS is very helpful in improving diagnosis. Additionally, certain types of fibroadenomas are vascularized and present as false positives to DOT, however, the fibroadenomas' well circumscribed morphology in US image can help rule out malignance. This study has the limitation that radiologists' evaluations were done on stationary ultrasound images. Real time assessment of ultrasound images while examining the patient may improve the overall diagnostic performance. Additionally, with other diagnostic information, such as mammograms and patient family history, the overall diagnostic performance can be further improved. This is a direction that we are pursuing in on-going clinical studies.

The proposed novel two-step diagnostic strategy employing a random forest classifier as a first step to filter out low suspicious benign lesions during patients' US exam has great potential to streamline breast diagnostic workflows by suggesting short-term follow-ups rather than biopsy. Based on a large patient pool, 64.8% of the benign lesions were identified by the first step random forest classifier with 1.9% false negative rate. The next step using an SVM classifier combining DOT total hemoglobin functional maps with other diagnostic image features, provides high overall performance, AUC of 0.937, in breast cancer diagnosis. The reported two-step diagnostic strategy can be generalized to other modality guided diffused optical tomography for the optimal management of breast cancer diagnosis.

References

1. There Regina J. Hooley, RJ, Scoutt, L M., Philpotts, L E. "Breast Ultrasonography: State of the Art," Radiology, September 2013, Volume 268, Issue 3

2. Jimmy O, Kisembo H, Bugeza S, Galukande M. "Breast cancer detection using sonography in women with mammographically dense breasts." BMC Med Imaging. 2014 Dec 30;14(1):241.

3. Corsetti V1, Houssami N, Ghirardi M, Ferrari A, Speziani M, Bellarosa S, Remida G, Gasparotti C, Galligioni E, Ciatto S. "Evidence of the effect of adjunct ultrasound screening in women with mammography-negative dense breasts: interval breast cancers at 1 year follow-up." Eur J Cancer. 2011 May;47(7):1021-6. doi: 10.1016/j.ejca.2010.12.002.

4. American College of Radiology. ACR BIRADS® Atlas Fifth Edition Quick Reference: "Ultrasound, Mammography, Magnetic Resonance Imaging, BI-RADS® Assessment Categories."

   http://www.acr.org/~/media/ACR/Documents/PDF/QualitySafety/Resources/BIRADS/Posters/BIRADS%20Reference%20Card_web_F.pdf

5. Dr Ayush Goel and Dr Frank Gaillard et al. "Benign and malignant characteristics of breast lesions at ultrasound", Mayo Clin Proc. Mar 2010; 85(3): 274–279.

6. The ASPE Technical Expert Panel on Improving Cancer Policy Research through Information Technology. "The Importance of Radiology and Pathology Communication in the Diagnosis and Staging of Cancer: Mammography as a Case Study." November 2010.

7. Flowers CI1, O'Donoghue C, Moore D, Goss A, Kim D, Kim JH, Elias SG, Fridland J, Esserman LJ "Reducing false-positive biopsies: a pilot study to reduce benign biopsy rates for BI-RADS 4A/B assessments through testing risk stratification and new thresholds for

intervention." Breast Cancer Res Treat. 2013 Jun;139(3):769-77. doi: 10.1007/s10549-013-2576-0.

8. Tromberg BJ, Cerussi A, Shah N, Compton M, Durkin A, Hsiang D, Butler J, Mehta R. "Imaging in breast cancer: diffuse optics in breast cancer: detecting tumors in pre-menopausal women and monitoring neoadjuvant chemotherapy." Breast Cancer Res. 2005; 7(6):279-85.

9. Choe R, Konecky SD, Corlu A, Lee K, Durduran T, Busch DR, Pathak S, Czerniecki BJ, Tchou J, Fraker DL, Demichele A, Chance B, Arridge SR, Schweiger M, Culver JP, Schnall MD, Putt ME, Rosen MA, Yodh AG. Differentiation of benign and malignant breast tumors by in-vivo three-dimensional parallel-plate diffuse optical tomography. J Biomed Opt. 2009 Mar-Apr;14(2):024020. doi: 10.1117/1.3103325.

10. Poplack SP, Tosteson TD, Wells WA, Pogue BW, Meaney PM, Hartov A, Kogel CA, Soho SK, Gibson JJ, and Paulsen KD. Electromagnetic Breast Imaging: Results of a Pilot Study in Women with Abnormal Mammograms. Radiology 2007; 243: 350-359;

11. Intes X. Time-domain optical mammography SoftScan: initial results. Acad Radiol. 2005 12(8):934-47.

12. Spinelli L, Torricelli A, Pifferi A, Taroni P, Danesini G, Cubeddu R. Characterization of female breast lesions from multi-wavelength time-resolved optical mammography. Phys Med Biol. 2005;50(11):2489-502.

13. Collettini F, Martin JC, Diekmann F, Fallenberg E, Engelken F, Ponder S, Kroencke TJ, Hamm B, Poellinger A. Diagnostic performance of a Near-Infrared Breast Imaging system as adjunct to mammography versus X-ray mammography alone. Eur Radiol. 2012 Feb;22(2):350-7. doi: 10.1007/s00330-011-2276-2.

14. Athanasiou A, Vanel D, Balleyguier C, Fournier L, Mathieu MC, Delaloge S, Dromain C . Dynamic optical breast imaging: a new technique to visualise breast vessels: comparison with breast MRI and preliminary results. Eur J Radiol. 2005;54(1):72-9.

15. van de Ven S, Elias S, Wiethoff A, van der Voort M, Leproux A, Nielsen T, Brendel B, Bakker L, van der Mark M, Mali W, Luijten P. Diffuse optical tomography of the breast: initial validation in benign cysts. Mol Imaging Biol. 2009 Mar-Apr;11(2):64-70.

16. Zhu Q, Cronin EB, Currier AA, Vine HS, Huang MM, Chen, NG, and Xu C. Benign versus Malignant Breast Masses: Optical Differentiation with US-guided Optical Imaging Reconstruction. Radiology 2005; 237:57-66

17. Zhu Q, Hegde PU, Ricci A Jr, Kane M, Cronin EB, Ardeshirpour Y, Xu C, Aguirre A, Kurtzman SH, Deckers PJ, Tannenbaum SH. Early-stage invasive breast cancers: potential role of optical tomography with US localization in assisting diagnosis. Radiology. 2010 Aug;256(2):367-78.

18. Zhu Q, DeFusco PA, Ricci A Jr, Cronin EB, Hegde PU, Kane M, Tavakoli B, Xu Y, Hart J, Tannenbaum SH. Breast cancer: assessing response to neoadjuvant chemotherapy by using US-guided near-infrared tomography. Radiology. 2013 Feb;266(2):433-42.

19. Ueda S, Nakamiya N, Matsuura K, Shigekawa T, Sano H, Hirokawa E, Shimada H, Suzuki H, Oda M, Yamashita Y, Kishino O, Kuji I, Osaki A, Saeki T. Optical imaging of tumor vascularity associated with proliferation and glucose metabolism in early breast cancer: clinical application of total hemoglobin measurements in the breast.

20. Choi JS, Kim MJ, Youk JH, Moon HJ, Suh HJ, Kim EK. US-guided optical tomography: correlation with clinicopathologic variables in breast cancer. Ultrasound Med Biol. 2013 Feb;39(2):233-40.

21. Brooksby B, Pogue BW, Jiang S, Dehghani H, Srinivasan S, Kogel C, Tosteson TD, Weaver J, Poplack SP, Paulsen KD. Imaging breast adipose and fibroglandular tissue molecular signatures by using hybrid MRI-guided near-infrared spectral tomography. Proc Natl Acad Sci U S A. 2006;103(23):8828-33.

22. Ntziachristos V, Yodh AG, Schnall MD, Chance B. MRI-guided diffuse optical spectroscopy of malignant and benign breast lesions. Neoplasia. 2002; 4(4):347-54.

23. Mastanduno MA, Xu J, El-Ghussein F, Jiang S, Yin H, Zhao Y, Michaelsen KE, Wang K, Ren F, Pogue BW, Paulsen KD. Sensitivity of MRI-guided near-infrared spectroscopy clinical breast exam data and its impact on diagnostic performance. Biomed Opt Express. 2014 Aug 22;5(9):3103-15.

24. Fang Q, Selb J, Carp SA, Boverman G, Miller EL, Brooks DH, Moore RH, Kopans DB, Boas DA. Combined optical and X-ray tomosynthesis breast imaging.

25. Krishnaswamy V, Michaelsen KE, Pogue BW, Poplack SP, Shaw I, Defrietas K, Brooks K, Paulsen KD. A digital x-ray tomosynthesis coupled near infrared spectral tomography system for dual-modality breast imaging. Opt Express. 2012 Aug 13;20(17):19125-36.

26. Zhu Q, Ricci A Jr, Hegde P, Kane M, Cronin E, Merkulov A, Xu Y, Tavakoli B, Tannenbaum S. Assessment of Functional Differences in Malignant and Benign Breast Lesions and Improvement of Diagnostic Accuracy by Using US-guided Diffuse Optical Tomography in Conjunction with Conventional US. Radiology. 2016 Aug;280(2):387-97.

27. Zhu Q, Tannenbaum S, Kurtzman SH, DeFusco P, Ricci A Jr, Vavadi H, Zhou F, Xu C, Merkulov A, Hegde P, Kane M, Wang L, Sabbath K. Identifying an early treatment window for predicting breast cancer response to neoadjuvant chemotherapy using

immunohistopathology and hemoglobin parameters. Breast Cancer Res. 2018 Jun 14;20(1):56.

28. Hosni, Mohamed, Ibtissam Abnane, Ali Idri, Juan M. Carrillo de Gea, and José Luis Fernández Alemán. "Reviewing ensemble classification methods in breast cancer." Computer methods and programs in biomedicine (2019).

29. Breiman, Leo. "Random forests." Machine learning 45, no. 1 (2001): 5-32.

30. Shan, Juan, S. Kaisar Alam, Brian Garra, Yingtao Zhang, and Tahira Ahmed. "Computer-aided diagnosis for breast ultrasound using computerized BI-RADS features and machine learning methods." Ultrasound in medicine & biology 42, no. 4 (2016): 980-988.

31. Liu, Jun, Jianxun Chen, Xiaoming Liu, and J. Tang. "An investigate of mass diagnosis in mammogram with random forest." In The Fourth International Workshop on Advanced Computational Intelligence, pp. 638-641. IEEE, 2011.

32. Nguyen, Cuong, Yong Wang, and Ha Nam Nguyen. "Random forest classifier combined with feature selection for breast cancer diagnosis and prognostic." Journal of Biomedical Science and Engineering 6, no. 05 (2013): 551.

33. Ahmad, Farzana Kabir, and Nooraini Yusoff. "Classifying breast cancer types based on fine needle aspiration biopsy data using random forest classifier." In 2013 13th International Conference on Intellient Systems Design and Applications, pp. 121-125. IEEE, 2013.

34. Uddin, KM Shihab, and Quing Zhu. "Reducing image artifact in diffuse optical tomography by iterative perturbation correction based on multiwavelength measurements." Journal of biomedical optics 24, no. 5 (2019): 056005.

35. Nelson, Eric, Charles Best, Willian McLean, and Merle Potter. "Schaum's Outline of Engineering Mechanics: Statics". McGraw-Hill Education, 2010, Chapter 12, page 235-277.

36. Liaw, Andy, and Matthew Wiener. "Classification and regression by randomForest." R news 2, no. 3 (2002): 18-22.

37. Dormann, Carsten F., Jane Elith, Sven Bacher, Carsten Buchmann, Gudrun Carl, Gabriel Carré, Jaime R. García Marquéz et al. "Collinearity: a review of methods to deal with it and a simulation study evaluating their performance." Ecography 36, no. 1 (2013): 27-46.

38. Huang, Minming, and Quing Zhu. "Dual-mesh optical tomography reconstruction method with a depth correction that uses a prioriultrasound information." Applied optics 43, no. 8 (2004): 1654-1662.

39. Uddin, KM Shihab, Atahar Mostafa, Mark Anastasio, and Quing Zhu. "Two step imaging reconstruction using truncated pseudoinverse as a preliminary estimate in ultrasound guided diffuse optical tomography." Biomedical optics express 8, no. 12 (2017): 5437-5449.

40. Xu, Chen, and Quing Zhu. "Light shadowing effect of large breast lesions imaged by optical tomography in reflection geometry." Journal of biomedical optics 15, no. 3 (2010): 036003.

41. Wang, Lipo, ed. Support vector machines: theory and applications. Vol. 177. Springer Science & Business Media, 2005.

42. Petrova, Marina, Petri Mähönen, and Alfredo Osuna. "Multi-class classification of analog and digital signals in cognitive radios using support vector machines." In 2010 7th International Symposium on Wireless Communication Systems, pp. 986-990

Chapter 5: Summary and Future Work

5.1 Summary

This dissertation has focused on algorithm development for robust data processing, image reconstruction, and classification of benign and malignant breast tumors using ultrasound guided DOT. First project, described in Chapter 2, was related to robust reconstruction for DOT. We proposed a two-step imaging reconstruction method. Initial estimate was obtained by taking a truncated Moore Penrose pseudoinverse of the weight matrix. That initial solution was refined by solving a L2 regularized optimization problem. We validated the proposed reconstruction method by both phantom experiment and clinical study. Calibrated phantoms submerged in intralipid solution were imaged by our US guided DOT system, and the proposed method was shown to have higher reconstruction accuracy than conventional reconstruction techniques. We performed clinical study on 20 human patients, 10 of them having malignant lesions and 10 having benign lesions. While we did not know the actual total hemoglobin concentration in the patient's breast, so it was not possible to calculate the reconstruction accuracy for clinical study, two step imaging reconstruction showed higher separation between the benign and malignant lesion groups. Thus, introducing pseudoinverse solution as preliminary estimate significantly increased diagnostic power of DOT. Choice of regularization was the most difficult part of this first project. Since DOT is a functional imaging modality, we could not arbitrarily try different regularization parameters to see which one worked best. Regularization was set to be proportional with largest singular value of weight matrix and the size of the tumor. This choice was heuristic but was consistently followed for all types of lesions.

We discussed an imaging artifact reduction technique in Chapter 3. Due to the tenfold noise reduction achieved in the system development and system calibration processes, our system had good signal to noise ratio, and most of the detector measurements could be used to reconstruct artifact-free images. But their use in clinical study is still unpredictable: there can be outliers in measurements because of patient motion, operator hand motion, patient breathing, tissue heterogeneity in the normal breast, and bad coupling between the optical fibers and tissue surface. These outliers produce image artifacts in the reconstructed absorption maps. We proposed an iterative perturbation correction approach based on structural similarity of images reconstructed from multiple wavelengths. The inherent assumption of this idea was that outliers were random and would produce different types of artifacts in different wavelength images, since these wavelengths were switched sequentially. Image quality index of anyone wavelength image was average of its structural similarity indices with other wavelength images. Measurement outliers were detected and removed until all the wavelength images had image quality index higher than 90%. Probability of a measurement being outlier was calculated by the distance between the original measurement and the projected measurement, which We obtained by projecting the reconstructed image onto the range of our imaging operator. This iterative perturbation measurement correction approach significantly improved the image quality for patients with inconsistent reconstructed absorption maps. Since, only one or two wavelengths images were changed, the total hemoglobin concentration might not change much, due to the perturbation correction.

While DOT provides valuable functional information to increase sensitivity of breast cancer diagnosis, the imaging pipeline is not fully automated, and can it take hours to get the reconstructed image. In Chapter 4, we proposed two-stage imaging scheme in which a near real time

recommendation of confirmed benignity was made for majority of the benign lesions. This recommendation was based on the DOT measurement data and radiologists' evaluations of US images, which were provided immediately. Morphological and histogram features were extracted from the measurement perturbation data. Those perturbation features were combined with ultrasound BIRADS scores and used in a random forest classifier to identify confirmed benign cases. Semi-automated ultrasound segmentation and image reconstruction were done for the rest of the lesions, which had intermediate suspicion level. Functional features were extracted, and suspicious lesions were classified as benign or malignant in the second stage of the imaging scheme. A support vector machine classifier was used in this stage. A random forest classifier correctly identified majority (65%) of the benign cases in near real time, with a very small false negative rate of 2%. This detection capability facilitates better clinical management of low risk breast cancer patients. Clinicians can adopt a less aggressive management for the confirmed benign patients, e.g., recommending a follow up instead of a surgical biopsy or removal of the breast. Introduction of perturbation features in the first stage improves specificity by more than 10% and thus can reduce unnecessary biopsies. Detailed methods, results and findings of the projects summarized in this section were published in different conference proceedings and journals [1-9].

5.2 Future Work

As our research group on DOT is getting bigger, more research is focused on automated data processing, image segmentation and application of artificial intelligence in DOT cancer diagnosis. In this section, I present several research ideas, some from literature study and others from my own preliminary formulations. These research directions might be valuable for future students.

5.2.1 Fully Automated Ultrasound Segmentation

DOT reconstruction is guided by ultrasound measurements. Lesion dimension and position extracted from the ultrasound images is used to identify the region of interested in dual mesh scheme DOT reconstruction [1]. Thus, fully automated ultrasound image segmentation is a critical step for clinical translation of DOT. Earlier research from our lab focused on semi-automated segmentation of US images [3], where user provides a seed for the lesion and draw a bounding polygon. Depth markers and chest walls were detected using edge detection techniques like sobel and canny edge detection. Instead of relying on a human to identify a region of interest, a region based convolutional neural network (r-cnn) can be used [10]. Convolutional neural network can be trained with labeled US images with regions marked as lesions. For test images, it first identifies the small candidate regions. Then those small regions are combined greedily based on how similar they are and how close they are. Based on predetermined features, final region will be selected from the shortlisted candidate regions. Another neural network-based segmentation model which is widely used now is mask r-cnn [11]. It extends the r-cnn by adding another branch for predicting object mask in addition to the bounding box prediction. Since DOT accuracy is not very sensitive to accuracy of the segmentation, a bounding box might be enough to perform the segmentation. The hardest part of this project would be labeling thousands of US images, since some images are unclear, and an undergraduate or graduate student researcher might need help from an experienced radiologist.

5.2.2 Joint Reconstruction of Reference and Target Breasts

An inherent assumption of DOT reconstruction is that the normal breast is homogeneous. This assumption is not true for many cases, and normal breast heterogeneity can result in imaging

artifacts which are difficult to get rid of. A possible solution to this problem would be to jointly reconstruct both the reference and target breasts. Objective function be written as follows:

$$\left\|P_{r,i} - W_i\Delta\mu_{a,r}\right\|^2 + \lambda_1\left\|\Delta\mu_{a,r}\right\|_2^2 + \left\|P_{l,r} - W_r\Delta\mu_{a,l}\right\|^2 + \lambda_2\left\|\Delta\mu_{a,l}\right\|_2^2$$

$$+ \begin{bmatrix} \lambda_{fine} & 0 \\ 0 & \lambda_{corase} \end{bmatrix} \left\| \begin{matrix} \Delta\mu_{a,l,fine} \\ \Delta\mu_{a,l,coarse} \end{matrix} - \begin{matrix} \Delta\mu_{a,r,fine} \\ \Delta\mu_{a,r,coarse} \end{matrix} \right\|_2^2 \quad , \quad (eq\ 5.1)$$

where $P_{r,i}$ is the perturbation from the fitted reference to the original reference, W_i is the weight from the fitted reference, $P_{l,r}$ is the perturbation from the reference to the lesion, and W_r is the weight from three reconstructed reference. An example of perturbation from the fitted reference to the original reference is shown in Figure 5.1.

(a) Reference Fitting
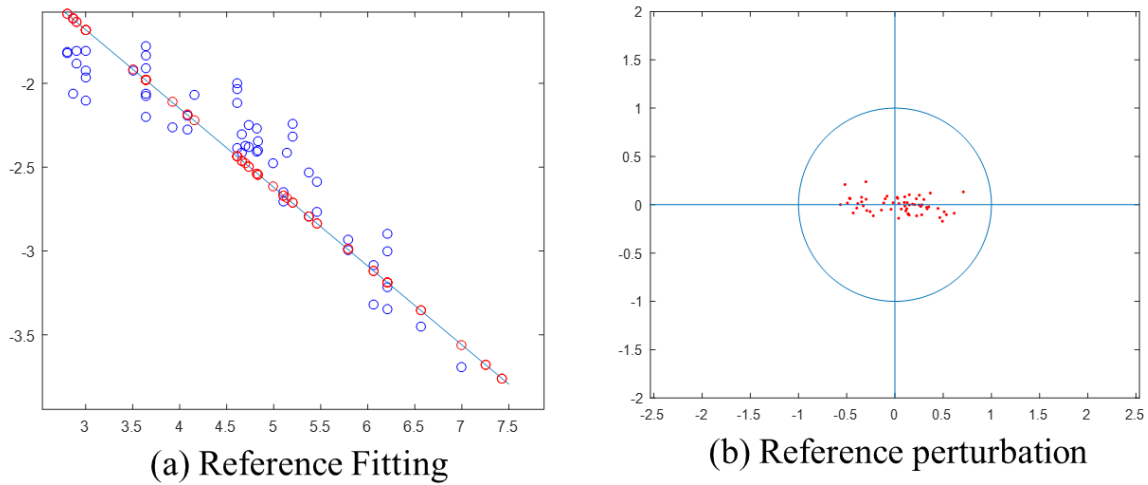
(b) Reference perturbation

Figure 5.1: Example of (a) reference fitting, where red circles correspond to fitted data and blue circles corresponds to actual measurements (b) perturbation from fitted data to actual reference measurements

A tentative algorithm for joint reconstruction of reference and target is presented in table 5.1.

Table 5.1: Joint reconstruction of reference and target

Initialize perturbation for reference, P_ref and perturbation for lesion, P_tar

Initialize absorption for reference, Mua_ref and absorption for lesion, Mua_tar

Weight for reference, W_ref (calculate from fitted background) and set W_tar=W_ref

REPEAT

    1. Update Mua_ref

    2. Update W_tar using using Mua_ref

    3. Update Mua_tar

UNTIL converge (max_iteration)

First, perturbation can be calculated for both reference and target sides. Refer to fig. 5.1 to see how to fit reference data and get the perturbation between the fitted reference and the original measurement data. In each iteration, first update reference absorption map. Based on the reference absorption map, update the weight matrix for target side. Since no analytical solution exists for a heterogeneous medium, we can use monte Carlo simulation [12] or finite element method [13] to generate the weight matrix. Finally, use this updated weight matrix to update lesion absorption map.

5.2.3 Simultaneous Reconstruction of Optical Absorption and Scattering

In this dissertation, we always assumed that scattering coefficient was constant and same for both reference and target sides, and that perturbation was due to absorption only. But human breast consists of different types of tissues with different scattering coefficients. Diffusion coefficient, which is inversely proportional to reduced scattering coefficient, is much smaller than absorption, so it is difficult to simultaneously reconstruct both absorption and scattering [1,14]. One possible solution would be to use weighted least squares by appropriately weighting the perturbation norms for absorption and scattering. We could introduce a regularization matrix, too, with varying regularization parameter for absorption and scattering.

5.2.4 No Gold Standard Evaluation for DOT Reconstrued Images

Absence of a gold standard is a big problem in clinical study. For phantoms and numerical simulations, we can calculate accuracies and compare multiple algorithms for a task like image reconstruction or segmentation. But since, we have no gold standard for clinical data, it is often difficult to compare performance of multiple algorithms. A no gold standard (NGS) evaluation of reconstructed images or segmented ultrasound lesions can be adopted where performance of multiple algorithms can be compared without a gold standard [15-17]. This no NCS evaluation assumes a linear relation between the true and estimated parameter values for different algorithms under evaluation [15]. Two evaluation metrics, the mean square error (MSE) and the noise: slope ratio, are used to evaluate performance of each method or algorithm. Since our new research group is more focused on developing algorithms for DOT and we have a large patient pool for validating our algorithms, a no gold standard evaluation would be a valuable tool for future DOT researchers.

References

1. Uddin, KM Shihab, Atahar Mostafa, Mark Anastasio, and Quing Zhu. "Two step imaging reconstruction using truncated pseudoinverse as a preliminary estimate in ultrasound guided diffuse optical tomography." Biomedical optics express 8, no. 12 (2017): 5437-5449.

2. Vavadi, Hamed, Atahar Mostafa, Feifei Zhou, KM Shihab Uddin, Murad Althobaiti, Chen Xu, Rajeev Bansal, Foluso Ademuyiwa, Steven Poplack, and Quing Zhu. "Compact ultrasound-guided diffuse optical tomography system for breast cancer imaging." Journal of biomedical optics 24, no. 2 (2018): 021203.

3. Mostafa, Atahar, Hamed Vavadi, KM Shihab Uddin, and Quing Zhu. "Diffuse optical tomography using semiautomated coregistered ultrasound measurements." Journal of biomedical optics 22, no. 12 (2017): 121610.

4. Vavadi, Hamed, Atahar Mostafa, Jinglong Li, Feifei Zhou, Shihab Uddin, Chen Xu, and Quing Zhu. "Preliminary results of miniaturized and robust ultrasound guided diffuse optical tomography system for breast cancer detection." In Optical Tomography and Spectroscopy of Tissue XII, vol. 10059, p. 100590F. International Society for Optics and Photonics, 2017.

5. Amidi, Eghbal, Guang Yang, KM Shihab Uddin, Ryan Wahidi, and Quing Zhu. "Low-cost ultrasound and optical gelatin-based phantoms." In Photons Plus Ultrasound: Imaging and Sensing 2019, vol. 10878, p. 108784A. International Society for Optics and Photonics, 2019.

6. Uddin, KM Shihab, and Quing Zhu. "Reducing image artifact in diffuse optical tomography by iterative perturbation correction based on multiwavelength measurements." Journal of biomedical optics 24, no. 5 (2019): 056005.

7. Xu, Shiqi, KM Shihab Uddin, and Quing Zhu. "Improving DOT reconstruction with a Born iterative method and US-guided sparse regularization." Biomedical optics express 10, no. 5 (2019): 2528-2541.

8. Uddin, KM Shihab, and Quing Zhu. "Local outlier factor based iterative outlier removal to reduce image artifacts in ultrasound guided diffuse optical tomography (Conference Presentation)." In Optical Tomography and Spectroscopy of Tissue XIII, vol. 10874, p. 108740D. International Society for Optics and Photonics, 2019.

9. Uddin, KM Shihab, Atahar Mostofa, Mark Anastasio, and Quing Zhu. "Improved two step reconstruction method in Ultrasound guided Diffuse Optical Tomography." In Optical Tomography and Spectroscopy, pp. OF1D-5. Optical Society of America, 2018.

10. Ren, Shaoqing, Kaiming He, Ross Girshick, and Jian Sun. "Faster r-cnn: Towards real-time object detection with region proposal networks." In Advances in neural information processing systems, pp. 91-99. 2015.

11. He, Kaiming, Georgia Gkioxari, Piotr Dollár, and Ross Girshick. "Mask r-cnn." In Proceedings of the IEEE international conference on computer vision, pp. 2961-2969. 2017.

12. Boas, David A., J. P. Culver, J. J. Stott, and Andrew K. Dunn. "Three dimensional Monte Carlo code for photon migration through complex heterogeneous media including the adult human head." Optics express 10, no. 3 (2002): 159-170.

13. Dehghani, Hamid, Subhadra Srinivasan, Brian W. Pogue, and Adam Gibson. "Numerical modelling and image reconstruction in diffuse optical tomography." Philosophical Transactions of the Royal Society A: Mathematical, Physical and Engineering Sciences 367, no. 1900 (2009): 3073-3093.

14. Tavakoli, Behnoosh, and Quing Zhu. "Two-step reconstruction method using global optimization and conjugate gradient for ultrasound-guided diffuse optical tomography." Journal of biomedical optics 18, no. 1 (2013): 016006.

15. Jha, Abhinav K., Brian Caffo, and Eric C. Frey. "A no-gold-standard technique for objective assessment of quantitative nuclear-medicine imaging methods." Physics in Medicine & Biology 61, no. 7 (2016): 2780.

16. Jha, Abhinav K., Esther Mena, Brian S. Caffo, Saeed Ashrafinia, Arman Rahmim, Eric C. Frey, and Rathan M. Subramaniam. "Practical no-gold-standard evaluation framework for quantitative imaging methods: application to lesion segmentation in positron emission tomography." Journal of Medical Imaging 4, no. 1 (2017): 011011.

17. Jha, Abhinav K., Matthew A. Kupinski, Jeffrey J. Rodriguez, Renu M. Stephen, and Alison T. Stopeck. "Task-based evaluation of segmentation algorithms for diffusion-weighted MRI without using a gold standard." Physics in Medicine & Biology 57, no. 13 (2012): 4425.